Stony Brook University

OFFICIAL COPY

The official electronic file of this thesis or dissertation is maintained by the University Libraries on behalf of The Graduate School at Stony Brook University.

© All Rights Reserved by Author.

EXPERIMENTAL CONSTRAINTS ON THE FRICTIONAL PROPERTIES OF FAULT ZONES THROUGH THE SAN ANDREAS FAULT OBSERVATORY AT DEPTH SCIENTIFIC DRILLING PROJECT

A Dissertation Presented

by

Sheryl Tembe

To

The Graduate School

in Partial Fulfillment of the

Requirements

for the Degree of

Doctor of Philosophy

In

Geosciences

Stony Brook University

December 2007

Copyright by
Sheryl Tembe
2007

The Graduate School

Sheryl Tembe

We, the dissertation committee for the above candidate for the Doctor of Philosophy degree, herby recommend acceptance of this dissertation.

Teng-fong Wong, Dissertation Advisor
Professor, Department of Geosciences, Stony Brook University

Daniel M. Davis, Chairperson of Defense
Professor, Department of Geosciences, Stony Brook University

William E. Holt
Professor, Department of Geosciences, Stony Brook University

Christiane Stidham
Lecturer, Department of Geosciences, Stony Brook University

David A. Lockner
Project Chief, Physics of Earthquakes and Faulting Project
US Geological Survey

This dissertation is accepted by the Graduate School.

Lawrence Martin
Dean of the Graduate School

Abstract of the Dissertation

EXPERIMENTAL CONSTRAINTS ON THE FRICTIONAL PROPERTIES OF FAULT ZONES THROUGH THE SAN ANDREAS FAULT OBSERVATORY AT DEPTH SCIENTIFIC DRILLING PROJECT

by

Sheryl Tembe

Doctor of Philosophy

in

Geosciences

Stony Brook University

2007

The mechanical behavior of a fault depends on the complex interaction between numerous parameters including composition, hydraulic properties, state of stress and the partitioning of strain between the country rock and gouge layer. One of the most important properties of the gouge is the coefficient of friction μ, defined as the ratio of shear stress to normal stress acting on the fault. In recent years a number of drilling projects have been conducted to retrieve core samples from seismogenic systems and systematic mineralogical characterization of core samples have underscored the pervasive occurrence of weak minerals in shear zones. I constrain the level of stress supported by a fault system based on laboratory measurements of the intrinsic strength of the fault materials and through modeling of fault zone pore fluid pressures. Friction experiments were conducted on materials derived at depth in the San Andreas Fault Observatory at Depth (SAFOD) borehole. A technique was developed to obtain meaningful mechanical data from drill cuttings and the data were used to construct a rheological profile of the country rock and faults penetrated by the SAFOD hole. It was observed that material strength was sensitive to mineralogical composition and the majority of the shear zones in the SAF system contained clay and hydrated phases. A systematic investigation into

the frictional sliding behavior of quartz-montmorillonite-illite gouge mixtures was undertaken to elucidate the role of mineralogy on strength. As clay content was increased, the strength of the gouge decreased nonlinearly in two stages, which were manifested as the development of Riedel shear fractures and clay foliation. To constrain the pore pressures involved, I modified Rice's (1992) theoretical model for fault zone overpressure to allow for variable μ in the gouge and incorporate recent findings at SAFOD. Experimental data obtained at hydrothermal conditions on illitic fault gouge from a minor strand of the SAF, chrysotile and talc were used to set the μ of the gouge. On this basis, the pore pressure required to weaken the SAF is highly sensitive to the relative deviatoric stress and the orientation of the maximum horizontal stress. If the findings at SAFOD of high relative deviatoric stress and near fault normal compression are taken at face value, then the fault zone pore pressures would have to be hydrostatic to 3 times the lithostatic stress.

Table of Contents

List of Figures

fault with shear stress of 100 MPa and r~0.8-1, the fault angle would be 16-21°. c) Effective normal stress in the fault zone for the end-member presented in Figure 1b (where $p_f = p_o$) assuming the overburden stress is equivalent to the normal stress (conventional model) or assuming the normal stress is as given by the modified model. The effective normal stress in the modified model is insensitive to the shear stress and r. d) With the shear stress and normal stress defined in (a) and (c), the coefficient of friction for the fault zone can be calculated for the conventional and modified models. The modified friction coefficients are insensitive to r and are significantly lower than the conventional model. To satisfy the heat flow constraint, the fault zone friction coefficients must be 0.1-0.2 and <0.05 in the conventional and modified, respectively.

List of Tables

Acknowledgements

I owe my deepest gratitude to my advisor Teng-fong Wong for challenging me with a variety of projects, putting my career in the forefront, and setting a fine example of scientific excellence and professionalism. By the same token, I am especially grateful David Lockner, for sharing his laboratory and extensive knowledge. I thank you both for wonderful experiences and for opening up a world of opportunities.

Committee members Dan Davis, Bill Holt, and Christiane Stidham provided stimulating discussion and comments. Patrick Baud, Steve Hickman, Carolyn Morrow, Diane Moore and John Rudnicki have kindly guided me through this and other research, for which I am so appreciative.

My time in Stony Brook was made enjoyable by many people over the years, including Natalie Chen, Laurent Louis, Wei Zhu, and in particular my friend and former lab mate, Veronika Vajdova. Your generous mentoring when I first joined the rock mechanics lab and now in all areas is invaluable.

Lastly, my biggest thanks goes to my parents and my husband for keeping me focused on the things that give life substance. I owe a great deal to my husband and sister for keeping me balanced, giving me strength, and always looking forward. I will never know how you guys managed to tolerate me in this last year of study, but I thank you for kindness and many home cooked meals.

Publications

Tembe, S., V. Vajdova, T.-f. Wong, W. Zhu, (2006), Initiation and propagation of strain localization in circumferentially notched samples of two porous sandstones, *Journal of Geophysical Research*, 111, B02409, doi:10.1029/2005JB003611.

Louis, L., T.-f. Wong, P. Baud, **S. Tembe**, (2006)], Imaging strain localization by X-ray computed tomography: Discrete compaction bands in Diemelstadt sandstone, *Journal of Structural Geology*, 29 (1), 129-140, doi:10.1016/j.jsg.2006.02.006.

Tembe, S., V. Vajdova, P. Baud, W. Zhu, T.-f. Wong, (2006), A new methodology to delineate the compactive yield behavior of two porous sandstones under undrained condition, *Mechanics of Materials*, 39, 513-523, doi:10.1016/j.mechmat.2006.08.005.

Tembe, S., D.A. Lockner, J.G. Solum, C.A. Morrow, T.-f. Wong, D.E. Moore, (2006), Frictional strength of cuttings and core from SAFOD drillhole phases 1 and 2, *Geophysical Research Letters*, 33, L23307, doi:10.1029/2006GL027626.

Morrow, C., J.G. Solum, **S. Tembe**, D.A. Lockner, T.-f. Wong, (2007), Using drill cutting separates to estimate the strength of narrow shear zones at SAFOD, *Geophysical Research Letters*, 34, L11301, doi:101029/2007GL029665.

Tembe, S., D. A. Lockner, T.-f. Wong, (2007), Effect of clay content and mineralogy on frictional sliding behavior of simulated gouges: Binary and ternary mixtures of quartz, illite and montmorillonite, *Journal of Geophysical Research*, submitted, MS#2007JB005290.

Tembe, S., P. Baud, T.-f. Wong, (2007), Stress conditions for the propagation of discrete compaction bands in porous sandstone, *Journal of Geophysical Research*, submitted, MS#2007JB005439.

Chapter 1

Introduction

Strain in the upper lithosphere is accommodated by brittle failure localized along faults. The level of stress supported by the lithosphere and the manifestation of fault slip as either creep or seismic depends on the mechanical response of the embedded faults and constituent materials to ambient conditions, which include gravitational and tectonic stresses, loading rate, pore fluid pressure and a thermal gradient. With both locked and creeping sections, and notable characteristic repeating earthquakes [e.g. *Bakun and McEvilly*, 1984, *Nadeau and McEvilly*, 1997], the San Andreas fault (SAF) system demonstrates a range of behaviors that have attracted considerable scientific attention. The fault broadly delineates a structural boundary between crystalline rock on the west side and Franciscan mélange and Great Valley sedimentary rock on the east side. Long-term displacement along the San Andreas has entrained material from both sides and resulted in the juxtaposition of mechanically dissimilar rock types. For example, the abutment of competent Coast Range ophiolites against weak Franciscan mélange and serpentinites in the Hayward fault, has led some to argue that seismicity (or creep) on the fault is largely controlled by the lithology [*Ponce et al*., 2003, *Graymer et al.,* 2005]. In

fact because substantial geophysical evidence exists for large serpentinite bodies at depth [e.g., *Ponce et al*., 2003, *McPhee* et al., 2004] and outcrops of serpentinized rock are pervasive in the region adjacent to the San Andreas [e.g.. *Hanna et al*., 1972, *Rymer et al*., 2006] it is hypothesized that the creeping segment in Central California may be the result of serpentine-bearing gouge [e.g. *Irwin and Barnes*, 1975].

Despite the correlation between slip behavior and regional geology presented above, the San Andreas fault is at the heart of a great disagreement between geophysical observations and laboratory measurements. Borehole breakout data and earthquake focal plane mechanisms indicate the maximum horizontal stress is at a high angle to the SAF [*Mount and Suppe*, 1987; *Zoback et al.,* 1987; *Townend and Zoback*, 2001, 2004], an unfavorable orientation for a strike-slip fault in which the shear stresses resolved on the fault would be minimized. Based on heat flow measurements throughout California it was observed that friction-induced heat flow across the fault zone (assuming a conductive-dominant thermal regime) was conspicuously low, similar to the background levels [*Brune et al*., 1969, *Lachenbruch and Sass*, 1980, *Lachenbruch and Sass*, 1992, *Williams et al*., 2004]. It was surmised the San Andreas would have to be extremely weak to slip and estimated average shear stress magnitudes of 10-20 MPa for the upper 14 km crust [*Brune et al*., 1969, *Lachenbruch and McGarr*, 1990]. In experimental rock mechanics studies, the shear stress levels required for sliding on an existing fractured surface scales with the effective normal stress by a factor referred to as the coefficient of friction. *Byerlee* [1978] showed that for many minerals and rocks the coefficient of friction is typically between 0.6-0.85. From the laboratory standpoint, in the brittle crust, this would correspond to average shear stress of 50-100 MPa [e.g., *Hanks*, 1977, *Brace and Kohlstedt*, 1980], considerably greater than implied by the heat flow studies.

Numerous fault-weakening scenarios have been posited over the decades to reconcile field and experimental observations and it is likely that several mechanisms are involved. These explanations broadly fall into three classes. First, intrinsically weak materials that are exceptions to *Byerlee's* [1978] empirical data, such as clays and certain serpentine minerals, which have friction coefficients as low as 0.1, could be present along principal slip surfaces and enable sliding under low shear stress. However, experimental

studies conducted at elevated temperatures on these minerals have raised questions regarding the stability of these materials at depth under elevated pressures and temperature [e.g. *Morrow et al*., 1992, *Lockner and Beeler*, 2002, *Moore et al.*, 2004, *Moore and Lockner*, 2007]. The second class of hypotheses hinge on the generation and maintenance of elevated fluid pressure confined to the fault zone [e.g. *Byerlee*, 1990, *Rice*, 1992, *Bredehoeft and Ingrebritsen*, 1990], which would reduce the effective stress and therefore shear stress level required for slip. It is uncertain how much fluid pressure is required to weaken the fault by almost an order of magnitude and if such pressures could be generated and maintained. Finally, the class dynamic weakening mechanisms range from means of reducing effective stress (thermal pressurization of pore fluid, normal stress changes due to elastic mismatch) [e.g., *Lachenbruch*, 1980, *Mase and Smith*, 1987, *Brodsky and Kanamori*, 2001, *Rudnicki and Rice*, 2006], or reducing viscosity of the gouge (frictional melting, gel formation, fluidization of gouge) [e.g. *McKenzie and Brune*, 1972, *Melosh*, 1996, *DiToro et al*., 2004]. The family of dynamic mechanisms includes probably the broadest and most creative solutions for fault weakening. In general, since they can only become relevant when rupture has commenced, they may explain why an initially moderate sized quake may develop into a large one. Given all the possible explanations, very little is known about the hydromechanical properties of the fault rock at in-situ conditions, leaving many of these explanations poorly constrained.

With a number of major inferences involved and a several hypotheses put forth in the field, the scientific community recognized the need for serious ground-truthing [*Hickman et al*., 2004]. As one component of the National Science Foundation's EarthScope initiative and in partnership with the US Geological Survey, the San Andreas Fault Observatory at Depth (SAFOD) was designed to directly monitor an active fault zone at seismogenic depth, to sample fault rocks and fluids, and to measure a broad spectrum of geophysical and geochemical properties by drilling into the hypocentral zone of M2 earthquakes. Parkfield, California was chosen as the site of the operation since it was well characterized following the *Parkfield Experiment* [*Bakun and Lindh*, 1985], which investigated the reoccurrence of M6 earthquakes in regard to earthquake prediction.

The drill site is located 1.8 km west of surface trace of the SAF and is situated between the locked and creeping sections. SAFOD drilling project is scheduled to be completed in 4 stages with high quality geophysical logging (e.g. FMI, spectral, resistivity, sonic). The project commenced in 2002 with the drilling of a 2.2 km vertical pilot hole into 0.8 km of sedimentary cover before terminating in fractured granodiorite [*Boness and Zoback*, 2004] and provided some of the earliest estimates of the stress state [*Hickman and Zoback*, 2004, *Townend and Zoback*, 2004] and heat flow [*Williams et al.*, 2004] adjacent to the fault. Phase 1 was conducted in 2005 with the drilling of the main hole to a vertical depth of 1.5 km at which point the borehole was inclined towards the microseismic patches of the SAF and stopped ~200 m short of the fault zone. Interestingly, just as in the pilot hole, the main hole crossed granodiorite but then encountered tertiary sedimentary rock at 1.9 km vertical depth. Phase 2 penetrated the SAF and terminated in the Great Valley siltstones on the NE side. A broad low-velocity zone ~30 m wide was discovered near the lithologic boundary separating the sides of the fault and subsequent logging of borehole elongation showed shearing of the hole [*Zoback et al*, 2006]. Phase 3 was completed in 2007 with multiple sidetracks and 3 spot cores retrieved from SAF fault strands. Instrumentation of the borehole with accelerometers, tiltmeters and fluid pressure transducers for long term monitoring at SAFOD is currently underway.

This research presented in this dissertation utilizes laboratory data on the frictional properties of samples obtained from the SAFOD drilling project to address three outstanding issues:

- What is the rheology of materials from and adjacent to the San Andreas? Which faults are weak and which are prone to unstable behavior?
- Pure clay minerals are known to be very weak and are ubiquitous in faults. How much clay does it take to weaken the fault? What role do clay minerals play in sliding – are they involved in active shear and do they *lubricate* faults? Does the presence of clay determine whether a fault will be seismic or creep?
- From the standpoint of the SAF heat-flow paradox, what weakening mechanisms may dominate in the creeping section of the SAF? How are gouge strength and fluid pressure coupled in weak fault zones?

In Chapter 2, I present experimental results on the frictional properties of SAFOD Phases 1 and 2 materials. The chapter titled *Frictional strength of cuttings and core from SAFOD drillhole phases 1 and 2* by Tembe, Lockner, Solum, Morrow, Wong and Moore has been published in *Geophysical Research Letters*. Since drill core retrieval was minimal in the initial phases, a technique was developed for obtaining good quality frictional data from drill cutting. I have tabulated the experimental data for the version included in the dissertation. The data set covers the entire deviated section of the main hole and identifies areas of interest for future investigation. Although not included in the dissertation, an extension of the technique was that published in *Geophysical Research Letters* by Morrow, Solum, Tembe, Lockner, and Wong details handling of bulk cuttings from narrow faults.

Chapter 3 presents findings from friction experiments on mixtures of smectite, illite, and quartz gouges. The experimental data when compared with natural shear zone materials demonstrate that the friction coefficient can be estimated from mineral composition. Microstructural analysis of gouge texture elucidates the role of clays in active shear zones. The chapter, *Effect of clay content and mineralogy on frictional sliding behavior of simulated gouges: Binary and ternary mixtures of quartz, illite and montmorillonite* by Tembe, Lockner, and Wong has been submitted to *Journal of Geophysical Research.*

Chapter 4 reviews popular stress analyses and Mohr circle constructions for a weak San Andreas. High-temperature friction data on clay fault gouge by acquired by SAFOD is incorporated into a modified Rice-style stress model to constrain pore pressure levels and stress state in the upper 15 km of the SAF. The chapter is in preparation for submission to *Journal of Geophysical Research*.

References

Bakun, W. H. and T. V. McEvilly, (1984), Recurrence models and Parkfield, California, earthquakes, *J. Geophys. Res*., 89, p. 3051-3058.

Bakun, W.H. and A.G. Lindh, (1985) The Parkfield, California, Earthquake Prediction Experiment, *Science*, 229, 4714, pp. 619 – 624.

Boness, N.L., and M.D. Zoback, (2004), Stress induced seismic velocity anisotropy and physical properties in the SAFOD pilot hole in Parkfield, CA, *Geophys. Res. Lett*., 31, doi:10.1029/2003GL019020.

Brace, W.F., and D.L. Kohlstedt, (1980) Limits on lithospheric stress imposed by laboratory experiments, *J.Geophys. Res*., 85, B11, 6248-6252.

Bredehoeft, J. D., and S. E. Ingebritsen (1990), Degassing of carbon dioxide as a possible source of high pore pressure in the crust, in *The Role of Fluids in Crustal Processes*, edited, pp. 158-164, National Academy Press, Washington, D.C.

Brodsky, E.E., and H. Kanamori, (2001), Elastohydrodynamic lubrication of faults, *J. Geophys. Res.*, *106*, 16357-16374.

Brune, J.N., T. Henyey, and R. Roy, (1969) Heat flow, stress, and rate of slip along San Andreas fault, California, *J. Geophys. Res*., 74, 3821-4009.

Byerlee, J.D., (1978) Friction of rocks, *Pure and Applied Geophysics*, 116, 615-26.

Byerlee, J.D., (1990), Friction, overpressure, and fault normal compression, *Geophys. Res.Lett.*, 17, 2109-2112.

DiToro, G., D.L. Goldsby, and T.E. Tullis, (2004) Friction falls toward zero in quartz rock as slip velocity approaches seismic rates, *Nature, 427*, 436-439.

Graymer, R.W., D.A. Ponce, R.C. Jachens, R.W. Simpson, G.A. Phelps, C.M. Wentworth, (2005), Three-dimensional geologic map of the Hayward fault, northern California: Correlation of rock units with variations in seismicity, creep rate, and fault dip, *Geology,* 33, 6, 521–524, doi: 10.1130/G21435.1

Hanna, W. F., R. D. Brown, Jr, D. C. Ross, and A. Griscom, (1972), Aeromagnetic reconnaissance and generalized geologic map of the San Andreas fault between San Francisco and San Bernardino, California. *US Geol. Surv. Geophys. Investig. Map GP-815*.

Hickman, S., and M.D. Zoback, (2004), Stress orientations and magnitudes in the SAFOD pilot hole, *Geophys. Res. Lett*., 31, doi:10.1029/2004GL020043.

Irwin, W. P. and I. Barnes, (1975). Effect of geologic structure and metamorphic fluids on seismic behavior of the San Andreas fault system in central and northern California. *Geology*, 3, 713–716.

Lachenbruch, A.H., (1980), Frictional heating, fluid pressure, and the resistance to fault motion, *J. Geophys. Res., 85*, 6097-6112.

Lachenbruch, A., and J. Sass, (1980), Heat flow and energetics of the San Andreas fault zone, *J. Geophys. Res*., 85, 6185–222.

Lachenbruch, A., and J. Sass, (1992), Heat flow from Cajon Pass, fault strength, and tectonic implications, *J. Geophys. Res*., 97, 4995-5015.

Lockner, D.A., and N.M., Beeler (2002), Rock failure and earthquakes-Chapter 32, in *International Handbook of Earthquake and Engineering Seismology*, edited by W.H.K. Lee, H. Kanamori, P.C. Jennings, and C. Kisslinger, 505-537, Academic Press, Amsterdam.

Mase, C.W., and L. Smith, (1987), Effects of frictional heating on the thermal, hydrologic, and mechanical response of a fault, *J. Geophys. Res., 92*, 6249-6272.

McKenzie, D. P., and J. N. Brune, (1972), Melting on fault planes during large earthquakes, *Geophys. J. R. Astron. Soc.*, *29*, 65–78.

McPhee, DK., R.C. Jachens, and C.M. Wnetworth, (2004) Crustal structure across the San Andreas Fault at the SAFOD site from potential field and geologic studies, *Geophys. Res. Lett*., 31, L12S03, doi:10.1029/2003GL019363.

Melosh, H. J.**,** (1996) Dynamical weakening of faults by acoustic fluidization, *Nature*, *379*, 601–606.

Moore, D. E., R. Summers, J.D. Byerlee (1989), Sliding behavior and deformation textures of heated illite gouge, *J. Struct. Geol., 11,* (3) 329-342.

Moore, D.E., D.A. Lockner, H. Tanaka, and K. Iwata, (2004), The coefficient of friction of chrysotile gouge at seismogenic depths, in *Serpentine and Serpentinites: Minerology,* Petrology, Geochemistry, Geology, Geophysics, and Tectonics, ed. W.G. Ernst, and B.J. Skinner, GSA Int. Geol. Rev., 46, 385-398.

Moore, D. E., D. A. Lockner, (2007), Comparative deformation behavior of minerals in serpentinized unltramafic rock: Application to the slab-mantle interface in subduction zones, *Int. Geol. Rev.,* 49, 401-415.

Moore, D.E. and D.A. Lockner (2007), Friction of the smectite clay montmorillonite: A review and interpretation of data, in Dixon, T. H., and Moore, J. C., eds., The Seismogenic Zone of Subduction Thrust Faults, MARGINS Theoretical and Experimental Earth Science Series, 2, in press.

Morrow, C. A., L. Q. Shi and J. D. Byerlee, (1982), Strain hardening and strength of clay-rich fault gouges, *J. Geophys. Res*., 87, 6771-6780.

Morrow, C.A., B. Radney, and J.D. Byerlee, (1992), Frictional strength and the effective pressure law of montmorillonite and illite clays, in *Fault Mechanics and Transport Properties of Rocks*, ed. B. Evans, and T.-f. Wong, 69-88, Academic Press, San Diego.

Morrow, C., J.G. Solum, S. Tembe, D.A. Lockner, T.-f. Wong, (2007), Using drill cutting separates to estimate the strength of narrow shear zones at SAFOD, *Geophysical Research Letters*, 34, L11301, doi:101029/2007GL029665.

Mount, V.S. and J. Suppe, (1987), State of stress near San Andreas fault: Implications for wrench tectonics, *Geology*, 15, 1143-1146.

Nadeau, R. M. and T. V. McEvilly, (1997) Seismological Studies at Parkfield V: Characteristic microearthquake sequences as fault-zone drilling targets, *Bull. Seis m. Soc. Am., 87*, 1463-1472.

Ponce, D.A., Hildenbrand, T.G., and Jachens, R.C., (2003), Gravity and magnetic expression of the San Leandro gabbro with implications for the geometry and evolution of the Hayward Fault zone, northern California: Bulletin of the Seismological Society of America, v. 93, no. 1, p. 1-13.

Rice, J.R., (1992), Fault stress states, pore pressure distributions, and the weakness of the San Andreas fault, in Fault mechanics and Transport Properties of Rocks, ed. B. Evans, and T.-f. Wong, 475-504, Academic Press, San Diego.

Rudnicki, J.W., J.R. Rice, (2006), Effective normal stress alteration due to pore pressure changes induced by dynamic slip propagation on a plane between dissimilar materials, *J. Geophys. Res*., 111, B10308, doi:10.1029/2006JB004396.

Rymer, M. J. et al. (2006) Surface fault slip associated with the 2004 Parkfield, California, earthquake. *Bull. Seismol. Soc. Am*. 96 (4B), S11–S27.

Sibson, R.H. and G. Xie, (1998), Dip range for intracontinental reverse fault ruptures: truth not stranger than friction. *Bull. Seismol. Soc. Am.,* 88, 1014–1022.

Sibson, R.H., (1973), Interaction between temperature and fluid pressure during earthquake faulting-A mechanism for partial or total stress relief, *Nature, 243*, 66-68.

Townend, J., and M. D. Zoback (2001), Implications of earthquake focal mechanisms for the frictional strength of the San Andreas Fault system, in The Nature and Tectonic Significance of Fault Zone Weakening, edited by R. E. Holdsworth et al., Geol. Soc. Spec. Publ., 186, 13– 21.

Townend, J., and M. D. Zoback (2004), Regional tectonic stress near the San Andreas Fault in central and southern California, Geophys. Res. Lett., 31, L15S11, doi:10.1029/2003GL018918.

Williams, C., F.V. Grubb, and S.P. Galanis, (2004), Heat flow in the SAFOD pilot hole and implications for the strength of the San Andreas Fault, *Geophys. Res. Lett*., 31, doi:10.1029/2003GL019352.

Chapter 2

Frictional Strength of Cuttings and Core from SAFOD Drillhole Phases 1 and 2

Abstract

We investigated the frictional properties of drill cuttings and core obtained from 1.85-3.1 km true vertical depth in the SAFOD scientific borehole in central California. Triaxial frictional sliding experiments were conducted on samples from primary lithologic units and significant shear zones, including the inferred active trace of the San Andreas fault. The samples were deformed at room temperature under constant effective normal stresses of 10, 40, and 80 MPa with axial shortening rates of 0.01-1.0 μm s^{-1}. The weakest samples were from shale, claystone, and siltstone units with friction coefficient μ= 0.4-0.55. Stronger samples were from quartzo-feldspathic rocks with μ ≥0.6. Materials tested from two shear zones at 2560 and 3067 m measured depth had μ=0.4-0.55 and velocity strengthening behavior that is consistent with fault creep at depths <4 km. The coefficient of friction for bulk samples from the inferred trace of the San Andreas fault was ~0.6.

1. Introduction

The San Andreas Fault Observatory at Depth (SAFOD) scientific borehole provides a unique opportunity to study samples from seismogenic depths of an active major plate-bounding fault. Understanding the state of stress and mechanical behavior of the San Andreas fault (SAF) is critical to resolving the long-standing stress-heat flow paradox [*Lachenbruch and Sass*, 1980; *Zoback et al*., 1987; *Lachenbruch and Sass*, 1992] and hinges on intrinsic rock properties adjacent to and inside the fault zone. In order to investigate the frictional properties of fault-derived rocks we have conducted laboratory experiments on samples acquired at depth during drilling of phases 1 and 2 of SAFOD.

The SAFOD main hole, located in central California near the town of Parkfield was drilled vertically into Salinian granitic rocks before being deviated at 1490 m toward the SAF. SAFOD subsequently penetrated over a kilometer of arkosic sandstones and conglomerates, and numerous faults before terminating in sedimentary rocks of the Great Valley sequence (Figure 1a). By the end of phase 2, drilling had yielded 20 m of spot core (from ~1463, 3056, and 3990 m measured depth) and drill cuttings for the entire 4.0 km long borehole (maximum vertical depth of 3.1 km). The SAFOD drilling strategy intentionally limited the amount of core that was retrieved during the initial phases to <1%, with continuous coring planned for phase 3 drilling in 2007. To augment data obtained from the limited core available at this time and to aid in planning the phase 3 drilling strategy, we conducted extensive frictional sliding tests on drill cuttings.

At least three important limitations exist for inferring in situ fault strength from cuttings. (1) The cuttings are mixed as they travel up the borehole so that narrow zones of potentially weak phases are under-represented or diluted in the samples collected at the surface. (2) Fine particles, including clays and weak minerals, are preferentially lost during drilling as the cuttings pass over the shale shakers and therefore may be under-sampled. (3) Cuttings may be contaminated by drill fluids. We report here our findings and assess the reliability of inferring mechanical properties from cuttings by comparing results to tests on spot cores.

2. Methodology

The SAFOD sampling protocol acquired cuttings at 3 m intervals for drilled sections and at 0.3 m intervals for cored sections of the borehole, and yielded *unwashed* and *washed* cuttings for scientific study. The *unwashed cuttings* (denoted by CUU in Figure 1) were collected from the shale shakers and air dried in their unwashed state. *Washed cuttings* (CU) were gently washed through a 106 μm sieve in tap water on-site to remove the bentonite drilling mud. The material that was left in the sieve was then air dried.

Guided by the local stratigraphy, X-ray diffraction (XRD) clay mineral analyses [*Solum et al*.,2006] and dipole sonic velocity logs, we selected 36 washed cuttings samples, 4 unwashed cuttings samples, and 6 core samples from depths spanning the length of the deviated main hole from 1890 to 4000 m measured depth (MD) (corresponding to 1.85 to 3.1 km true vertical depth). Cuttings were chosen to represent primary lithologic units as well as significant shear zones, including the inferred active trace of the SAF.

Further preparation of the samples was conducted in the laboratory. Washed cuttings samples were cleaned in an ultrasonic bath in deionized water for 30 minutes to remove any residual drilling fluid. The remaining bathwater was poured off (reserved for later analysis) and the cuttings left to air dry. The majority of our friction tests were carried out on these twice-washed samples, which we will denote as CU-W. Subsets of unwashed cuttings were cleaned once and twice in an ultrasonic bath following the procedure described above in order to evaluate the effect of washing (referred to as CUU-W and CUU-WW, respectively).

Cursory inspection of the samples at this stage showed the presence of two contaminants remaining from the drilling process. The first were loss circulation materials (coarsely ground nut shells referred to as *nut plugs*) that were added to the drilling fluid to reduce mud loss in case a fissure should open while drilling. The nut plugs were easily separated from the bulk material owing to their density contrast. The second contaminant was metal filings from the drill bit, estimated to be <5 wt. % in most

samples. As standard practice adopted for phase 2, a bar-magnet was passed through the samples to remove this small fraction of metal. All samples were then crushed and passed through a 100 mesh sieve to obtain particles sizes of <149 μm.

Triaxial sliding experiments were conducted at room temperature on cylindrical (2.54 cm diameter) granite/sandstone forcing blocks containing saw-cuts inclined at 30° and filled with 1 mm-thick sample gouge layers following the procedure detailed by *Morrow et al*. [1992]. To approximately duplicate the in situ effective stress, tests were run at constant normal stresses of 11.0 and 41.0 MPa, and at constant pore pressure of 1.0 MPa. Deionized water was used as the pore fluid, and to assure good pore pressure communication between the gouge layer and the external pore pressure system, the upper driving block was a porous (20%) Berea sandstone with high permeability. The lower granite driving block had low porosity (< 1%) to minimize the generation of pore pressure transients that might result during rapid stress changes.

The samples were sheared up to 9 mm of axial displacement (10.4 mm slip resolved on the saw-cut) at axial displacement rates of 0.01, 0.1 and 1.0 μm/s. Since the samples typically strain hardened to a steady stress level within 1 to 2 millimeters it was possible to incorporate two pressure steps into a single run doubling the number of analyses. A total of 46 washed and unwashed cuttings samples were tested.

Strength tests were conducted on 5 intact rectangular prisms (1.8 x 1.8 x 4.6 cm) of granodiorite drill core from 1498 m MD in the conventional triaxial configuration at confining pressures of 10 to 160 MPa. The samples were deformed at a constant shortening rate, corresponding to a nominal strain rate of 10^{-5} s^{-1}. With the exception of the granodiorite, the SAFOD core was generally too damaged to obtain intact samples suitable for mechanical testing. As an alternative, frictional sliding tests were carried out on drill core fragments that were crushed to a particle size of <149 μm and deformed in the same manner as the cuttings samples at constant effective normal stresses of 10, 40, and 80 MPa. In all, 12 experiments were conducted on core samples from 3058, 3065, 3066, 3067, and 3991 m MD. A complete list of samples tested in this study is compiled in Tables 1 and 2.

3. Results

3.1 Frictional Strength Profile

In Figure 1 we summarize laboratory and logging data as functions of depth for the lower half of the main hole from 1400 to 4000 m MD. For reference, a simplified lithology modified from commercial mud logs (available online: www.icdp-online.de/sites/sanandreas/public/public.html) is shown in Figure 1a. Figure 1b plots coefficient of friction, μ (defined as the ratio of shear stress to effective normal stress resolved on the saw-cut) for experiments on cuttings (at 4.8 mm and 8.6 mm of axial displacement), and on core (at 8.6 mm of axial displacement). Zones where smectite, illite and chlorite were identified in relatively high concentrations by XRD [*Solum et al*., 2006] are indicated in Figure 1c. Seismic velocity data from dipole sonic logs for this section of the borehole are also shown in Figure 1d [*Boness and Zoback*, 2006].

The coefficients of friction for washed cuttings and core spanned the range of 0.4 to 0.8 and typically showed a slight increase with effective normal stress. Relatively higher values of μ ($\geq$0.6) corresponded to quartzo-feldspathic rocks derived from granodiorite, arkose, sandstone, and conglomerate facies encountered in the drill hole, and are comparable to the sliding frictional strength measured in the intact granodiorite core samples from 1498 m MD. Lower values of μ (0.40 – 0.55) were observed at depth intervals corresponding to siltstone, shale and claystone units. Two distinct regions at ~2600 and 3067 m MD are interpreted to be shear zones based on low strength (μ=0.4-0.5), enriched clay content, and reduced seismic velocities. The active trace of the San Andreas Fault inferred from borehole casing deformation [*Zoback et al*., 2006] at 3310-3353 m MD is within a lithological transition zone [*Solum et al*., 2006] and is manifested in the laboratory data as a modest decrease in frictional strength.

A comparison of unwashed cuttings samples (which should have retained much of their fine grained material) and samples washed following different preparation routines was used to evaluate the loss of fine particles. The various washing procedures for cuttings appear to have little effect on the frictional strength (Figure 1b). In contrast

experiments on unwashed cuttings (orange squares) varied greatly in a somewhat unsystematic manner, ranging from values of μ observed for relatively pure bentonite (a major constituent of the drilling mud) to granitic rocks.

3.2 Comparison With Core Samples

To assess the extent to which the cuttings data provide a realistic proxy for actual in situ strength, we compared the results of mechanical deformation experiments on drill core with cuttings for three common facies: granodiorite, conglomerate, and siltstone.

Intact granodiorite core samples (1498 m MD) failed by brittle fracture in strength tests. The coefficient of friction measured during sliding on fracture surfaces formed during these tests is 0.68 ± 0.03, comparable to the friction coefficients obtained for saw-cut experiments of granodiorite drill cuttings at 1890 m MD which typically have μ = 0.7-0.8. As in all of the saw-cut experiments, stable sliding behavior and overall strain hardening were observed, and most samples showed an increase in strength with increasing sliding rate.

A comparison of conglomerate samples from the equivalent depth at 3058 m MD in Figure 2a shows a high friction coefficient (0.75-0.85), as expected. However, the slight difference between cuttings and core suggests biased sampling of the coarse grained rock, or the involvement of contamination from metal filings and perhaps the loss of formation clays in the washed cuttings.

Figure 2b shows μ plotted as a function of axial displacement for core samples obtained from near the bottom of the Phase 2 borehole at 3991 m MD (3070 m TVD). This section of core is from a Great Valley siltstone unit on the NE side of the SAF. Experiments on core samples show steady sliding behavior, strain hardening, and strengthening in response to increasing velocity steps. The cuttings from this depth demonstrate similar behavior.

The agreement between strength data obtained from drill cuttings and core supports the feasibility of the method under appropriate conditions which are sensitive to the fraction of weak phases present in the cuttings.

3.3 Dilution of Weak Phases

At the termination of Phase 1 at 3067 m MD the SAFOD borehole had intersected a fracture zone considered to be the southwest strand of the San Andreas [*Hickman et al*., 2005] This shear zone is approximately 30 cm thick and is composed of 48-51% illite, 14-18% illite-smectite, 19-22% feldspar, 11-17% quartz, 1% chlorite, and trace amounts of calcite [*Solum et al*., 2006]. The coefficient of friction of drill core samples shown in Figure 3a was measured to be 0.40-0.45, notably weaker than cuttings (~0.6) tested at this same depth, but similar to the values obtained for other shear zones. We can also surmise based on the sampling interval that for a shear zone to be reliably detected in the cuttings the section would have be at least 2 to 3 meters thick. Since this layer is narrow and bounded by a conglomerate unit the differences in strength are likely due to mixing of material in the cuttings samples, resulting in the averaging of mechanical properties over an interval of 0.3 m or more. Application of appropriate mixing rules for a polymineralic system would help to define these narrow zones.

While resolving a narrow shear zone in the cuttings may not be straightforward, broad shear zones are readily detected in the cuttings. As an example Figure 3b presents friction data for a thick clay bearing unit at 2560 m MD, interpreted to be a shear zone based on its enrichment in illite and illite-smectite clays, reduced seismic velocities and associated anomalies in downhole geophysical log data (e.g., natural gamma ray, resistivity). This moderately weak layer is bounded by stronger sandstone units at 2377 and 2713 m MD, and the difference in frictional strength is easily discerned.

The quality of the cuttings data may be enhanced further since material from slip surfaces can be recognized in the cuttings by slickensides on grain fragments. Although a tedious process, these grains can be separated from the bulk material and subjected to laboratory testing. We developed a meticulous approach based on hand selection of

drillhole cuttings separates for more detailed measurements on narrow shear zones [*Morrow et al*., 2007]. Cuttings from two shear zones (one an active trace of the San Andreas fault) that exhibit deformation-induced slickensides were hand picked to prepare gouge samples for frictional experiments. In these tests the coefficients of friction for clay-rich and serpentine grains were 0.3-0.35 and 0.4-0.45, respectively and are included in Figure 1 as black triangles. These values are around 0.12 lower than the friction coefficient of the corresponding bulk cuttings, providing an improved estimate of the frictional strength of the San Andreas fault.

3.4 Preferential Loss of Clay Phases

While frictional strength data from cuttings are inherently limited by the sampling interval, cuttings from a large shear zone may be affected by the loss of fine particles. For example, despite recent indications of a broad actively deforming region from 3310 m to 3353 m MD [*Zoback et al*., 2006], the strength data for samples in the vicinity of the San Andreas Fault do not reflect the presence of an exceptionally weak shear zone (Figure 1b). Mineralogical characterization by *Solum et al.* [2006] of washed cuttings from the inferred active trace of the SAF determined the clay content to be between 5-35 % illite, 8-23 % chlorite, 6 % calcite, with trace amounts of serpentine (2 %) and laumontite (<2 %). If the preferential removal of low strength mineral phases from drill cuttings is occurring, then one way of constraining the effect of the lost clay fraction would be from experiments on unwashed cuttings samples. However given the unsystematic variation in mechanical data due to contamination, the results are inconclusive. Another method we are pursuing is to quantify the lost fraction from XRD analyses of unwashed cuttings and drilling fluid separated by the shale shakers to in order to reconstruct a sample for laboratory testing that would be better representative of the formation or shear zone.

4. Discussion and Conclusions

Arguments for a weak SAF arise from the absence of a friction-induced surface heat flow anomaly [*Lachenbruch and Sass*, 1980; *Lachenbruch and Sass* 1992; *Williams et al*., 2004] and stress orientation data [*Zoback et al.,* 1987; *Hickman and Zoback*, 2004], suggest a relatively low resolved shear stress (on the order of 10-20 MPa for the upper 15 km of the SAF) and coseismic frictional strength of $\mu = 0.1$ to 0.2, well below the friction coefficient observed for most crustal rocks [e.g., *Byerlee*, 1978]. Low strength minerals are a common constituent of fault gouge and have often been invoked to reconcile field and laboratory observations [*Wu et al*., 1975]. Accordingly previous studies have focused on clays and phyllosilicates derived from surface and shallow borehole samples [e.g., *Morrow et al*., 1982], and pure mineral analogs [e.g., *Morrow et al.,* 1992; *Moore et al.*, 1996] to infer mechanical properties of the San Andreas Fault. Our study of deep, fault-derived materials provides the best SAF fault zone strength data to date by measuring 63 samples that span a depth range of 2 km. We have established an experimental methodology and demonstrated that meaningful mechanical information can be derived from cuttings despite potential difficulties caused by drilling and sample collection, as evidenced by good agreement between strength of core and cutting samples, XRD analyses and downhole log data.

Two weak shear zones (~2560 and 3067) with friction coefficients ranging from 0.4 to 0.55 were measured in our study and their mechanical data are consistent with fault creep behavior observed in central California down to 4 km depth. The inferred active trace of the SAF at 3310-3353 m MD was found to have a friction coefficient ~0.60 in bulk cuttings samples. If the SAF is indeed unusually weak, then our data demonstrate that the presence of weak alteration minerals would account for only a portion of this reduced strength. Other mechanisms such as elevated pore fluid pressure or dynamic weakening processes may be involved in controlling fault strength, although fault-related elevated fluid pressure has yet to be detected in the SAFOD hole [*Zoback et al*., 2006]. Moreover, to extrapolate to seismogenic conditions we must also consider the role of temperature and the presence of chemically reactive fluids. Studies conducted on heated

chrysotile show overall strengthening with increasing effective pressure and temperature [*Moore et al*., 2004]. Similarly, montmorillonite and illite gouges deformed at high effective pressures [*Morrow et al.,* 1992] strengthen to values well above the heat flow constraint. Nevertheless, many uncertainties remain and more definitive conclusions cannot be drawn partly due to the paucity of core samples retrieved from the initial phases of SAFOD. Fully exploring the constitutive properties and fine structure of the SAF from continuous core available in phase 3 drilling will be critical to resolving the stress-heat flow paradox.

Acknowledgments

We are grateful to the SAFOD volunteers for their tremendous effort in collecting, preserving, and documenting the samples. We also thank Nick Beeler, Steve Hickman, and Brian Kilgore of the USGS for comments and discussion during the course of this work. Fred Chester and Dan Faulkner provided thoughtful reviews that have improved the manuscript. ST is supported by a Department of Education GAANN Fellowship. The research at Stony Brook was partially supported by US National Science Foundation under grant EAR-0346022.

References

Boness, N.L., and M.D. Zoback, (2006), A multiscale study of the mechanisms controlling shear velocity anisotropy in the San Andreas Fault Observatory at Depth, *Geophysics*, doi:10.1190/1.2231107.

Byerlee, J.D., (1978) Friction of rocks, *Pure and Applied Geophysics*, 116, 615-26.

Hickman, S., M.D. Zoback, (2004), Stress orientations and magnitudes in the SAFOD pilot hole, *Geophys. Res. Lett*., 31, doi:10.1029/2004GL020043

Hickman, S.H, M.D. Zoback, W.L. Ellsworth, (2005), Structure and Composition of the San Andreas Fault Zone at Parkfield: Initial Results from SAFOD Phases 1 and 2, *EOS Trans. AGU,* 86(52), Fall Meet. Suppl., Abstract T23E-05.

Lachenbruch, A., and J. Sass, (1980), Heat flow and energetics of the San Andreas fault zone, *J. Geophys. Res*., 85, 6185–222.

Lachenbruch, A., and J. Sass, (1992), Heat flow from Cajon Pass, fault strength, and tectonic implications, *J. Geophys. Res*., 97, 4995-5015.

Moore, D.E., D.A. Lockner, R. Summers, S. Ma, and J.D. Byrelee, (1996), "Strength of chrysotile-serpentinite gouge under hydrothermal conditions: Can it explain a weak San Andreas fault?" *Geology* 24(11): 1041-1045.

Moore, D.E., D.A. Lockner, H. Tanaka, and K. Iwata, (2004), The coefficient of friction of chrysotile gouge at seismogenic depths, in *Serpentine and Serpentinites: Minerology, Petrology, Geochemistry, Geology, Geophysics, and Tectonics*, ed. W.G. Ernst, and B.J. Skinner, GSA Int. Geol. Rev., 46, 385-398.

Morrow, C. A., L. Q. Shi and J. D. Byerlee, (1982), Strain hardening and strength of clay-rich fault gouges, *J. Geophys. Res*., 87, 6771-6780.

Morrow, C.A., B. Radney, and J.D. Byerlee, (1992), Frictional strength and the effective pressure law of montmorillonite and illite clays, in *Fault Mechanics and Transport Properties of Rocks*, ed. B. Evans, and T.-f. Wong, 69-88, Academic Press, San Diego.

Morrow, C., J.G. Solum, S. Tembe, D.A. Lockner, T.-f. Wong,(2007), Using drill cutting separates to estimate the strength of narrow shear zones at SAFOD, *Geophys.Res.Lett.*, 34, L11301, doi:101029/2007GL029665.

Solum, J.G., S.H. Hickman, D.A. Lockner, D.E. Moore, B.A. van der Pluijm, and J.P. Evans, (2006), Mineralogical characterization of protolith and fault rocks from the SAFOD main hole, *Geophys. Res. Lett. ,in press.*

Williams, C., F.V. Grubb, and S.P. Galanis, (2004), Heat flow in the SAFOD pilot hole and implications for the strength of the San Andreas Fault, *Geophys. Res. Lett.,* 31, doi:10.1029/2003GL019352.

Wu, F.T, L. Blatter, H. Roberson, (1975), Clay gouges in the San Andreas Fault System and their possible implications, Pure and Applied Geophysics, 113, 87-95, doi 10.1007/BF01592901.

Zoback, M.D., et al. (1987), New evidence for the state of stress on the San Andreas fault system, *Science*, 238, 1105-1111.

Zoback, M.D, S.H. Hickman, and W.L. Ellsworth, (2006) Structure and properties of the San Andreas fault in central California: Preliminary results from the SAFOD experiment, *Geophysical Research Abstracts*, Vol. 8, 02474, SRef-ID: 1607-7962/gra/EGU06-A-02474.

Table 2.1. Summary of experimental runs on bulk cuttings samples. Sample type and procedure use the following coding: CU: Cuttings washed on-site, CUU: unwashed cuttings, CU-W: Cuttings washed on-site and once in the lab, CUU-W: unwashed cuttings washed once in the lab, CUU-WW: unwashed cuttings washed twice in the lab.

Measured Depth (m)	Lithology	Sample # and Preparation Procedure	Coefficient of Friction	
			10 MPa at 4.8 mm	40 MPa at 8.6 mm
1890	granitic	CUW 6200	0.815	0.798
1951	granitic gouge	CUW 6400	0.810	0.801
2073	sandstone	CUW 6800	0.800	0.773
2195	sandstone	CUW 7200	0.771	0.737
2195	sandstone	CUU 7200	0.142	0.152
2377	granitic,	CUW 7800	0.781	0.803
2551	shale	CUW 8370	0.533	-
2560	shale	CUW 8400	0.495	0.494
2560	shale	CUL 8400	0.451	0.441
2612	shale, sandstone,	CUW 8570	0.597	0.483
2658	shale	CUW 8720	0.659	0.589
2682	shale	CUW 8800	0.582	0.472
2713	sandstone, shale,	CUW 8900	0.764	0.735
2896	sandstone, shale, siltstone	CUW 9500	0.740	0.736
2896	sandstone, shale, siltstone	CU 9500	0.690	0.725
2896	sandstone, shale, siltstone	CUU 9500	0.712	0.666
2896	sandstone, shale, siltstone	CUL 9500	0.719	0.707
2896	sandstone, shale, siltstone	CULL 9500	0.744	0.725
2987	sandstone, siltstone	CUW 9800	0.683	0.684
2987	sandstone, siltstone	CUU 9800	0.547	0.554
2987	sandstone, siltstone	CUL 9800	0.612	0.600
3018	sandstone	CUW 9900	0.781	0.792
3058	conglomerate	CU 10032	0.806	0.819
3058	conglomerate	CUW 10032	0.804	0.833
3065	siltstone	CUW 10057	0.618	0.622
3067	siltstone	CUW 10062	0.709	0.678
3155	sandstone, siltstone	CUW 10350	0.577	0.567
3216	sandstone, shale, siltstone	CUW 10550	0.717	0.670
3277	sandstone, shale, siltstone, clay	CUW 10750	0.614	0.648
3307	siltstone, sandstone, shale	CUW 10850	0.609	0.619
3313	sandstone, siltstone, claystone	CUW 10870	0.804	0.833
3338	shale, sandstone, siltstone	CU 10950	0.524	0.578
3399	shale, siltstone	CUW 11150	0.517	0.530
3459	shale, siltstone, sandstone	CUW 11350	0.564	0.548
3490	shale, siltstone	CUW 11450	0.521	0.556

Measured Depth (m)	Lithology	Sample # and Preparation Procedure	Coefficient of Friction	
			10 MPa at 4.8 mm	40 MPa at 4.8 mm
continued…				
3520	shale, siltstone, sandstone	CUW 11550	0.497	0.535
3581	shale, sandstone, siltstone	CUW 11750	0.480	0.540
3642	shale, siltstone, sandstone	CUW 11950	0.538	0.569
3703	shale, siltstone, sandstone, clay	CUW 12150	0.533	0.550
3770	siltstone ,shale, sandstone	CUW 12350	0.524	0.536
3801	siltstone, shale, sandstone	CUW 12470	0.488	0.540
3831	siltstone ,shale, sandstone	CUW 12570	0.527	0.549
3892	shale, sandstone, siltstone	CUW 12770	0.620	0.591
3987	shale, siltstone, sandstone	CUW 13080	0.606	0.573
3990	siltstone, shale	CUW 13092	0.513	0.571

Table 2. Summary of experimental runs on crushed drill core samples.

Measured Depth (m)	Lithology	Coefficient of Friction		
		10 MPa	40 MPa	80 MPa
3057.8	conglomerate	0.736	0.744	-
3065.4	siltstone	0.599	0.554	-
3066.6	clay gouge	0.446	0.401	0.423
3066.9	clay gouge	0.444	0.422	0.420
3990.7	siltstone	0.551	0.541	0.534

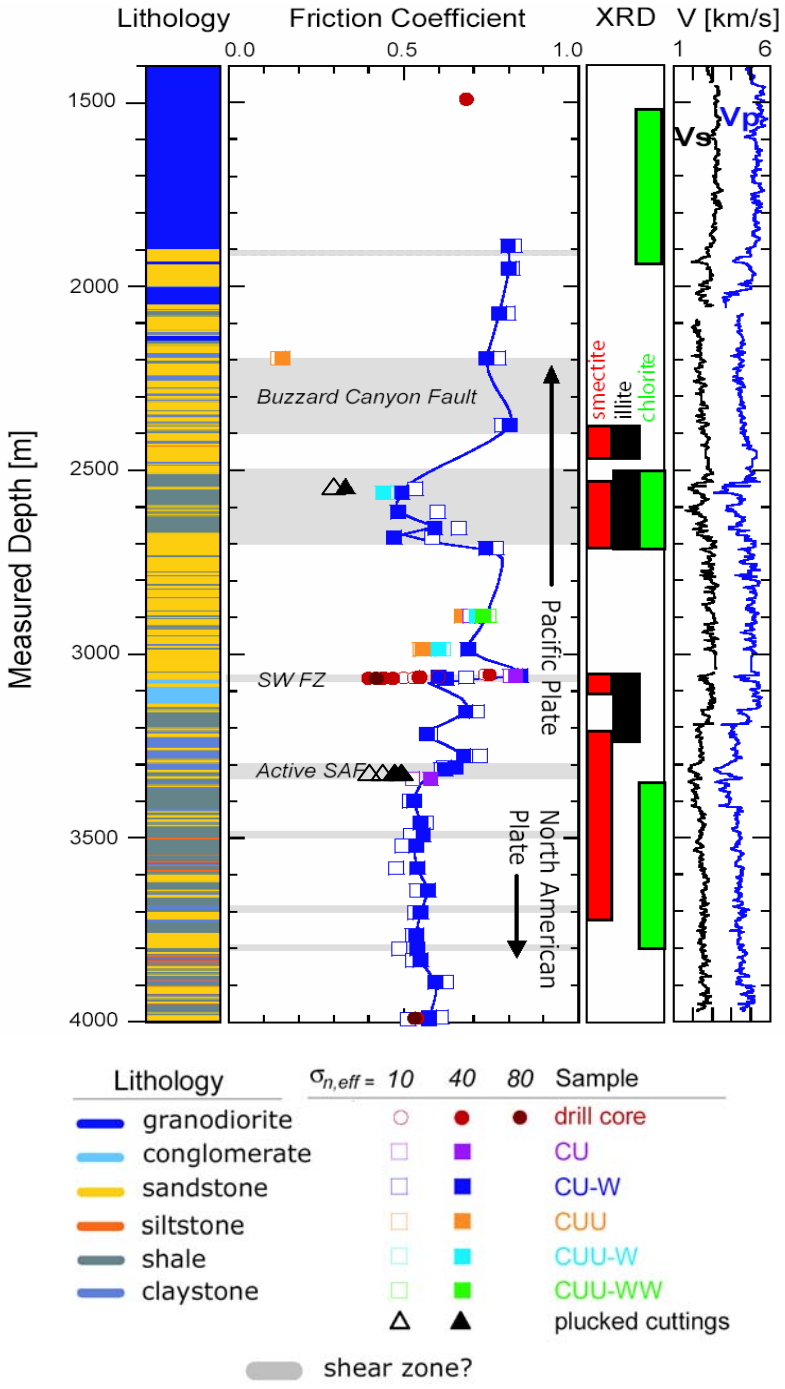

Figure 2.1. Depth profile of the SAFOD main hole showing (a) simplified lithology (b) friction coefficient of cuttings (indicated by square symbols) and drill core (circles). The points are color coded according to preparation procedure. The black triangle is from a preliminary test on cuttings separates. (c) Sections where typical fault gouge minerals were found in significant abundance are indicated. (d) Seismic velocity log data.

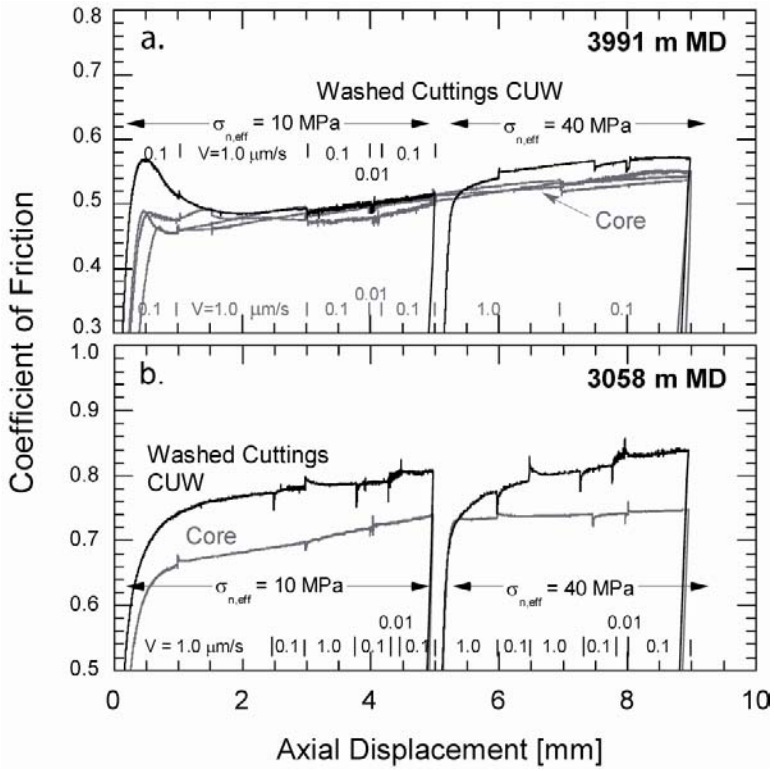

Figure 2.2 Comparison of friction coefficient versus axial displacement for cuttings and core samples from (a) conglomerate unit at 3058 m MD and (b) siltstone unit at 3991 m MD. Data for drill core samples are plotted in gray and cuttings data are in black.

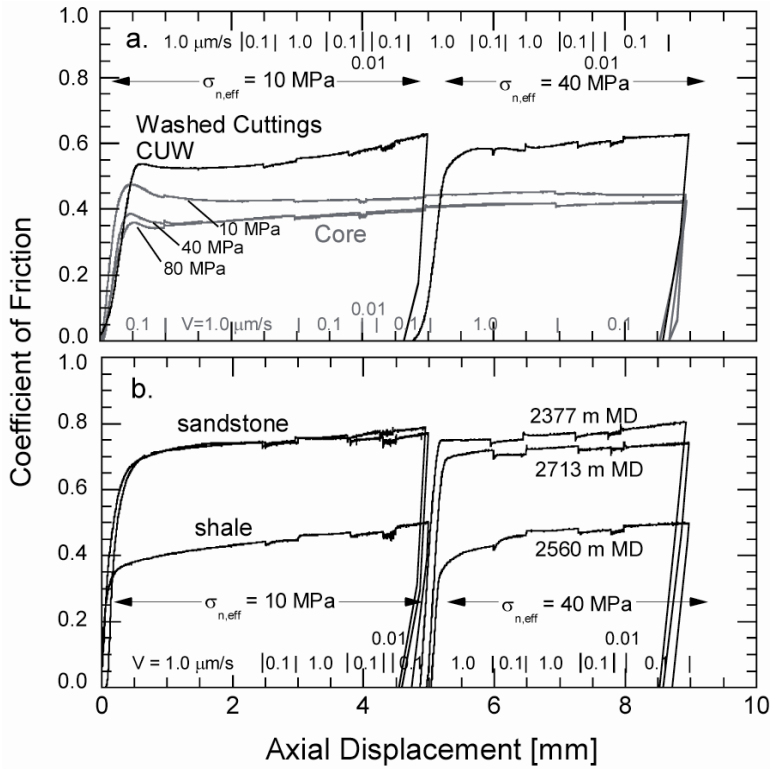

Figure 2.3 Coefficient of friction versus axial displacement for two shear zones. (a) Narrow shear zone at 3067 m MD. The signal of weaker material is diluted in the cuttings, while in (b) a broad illite clay shear zone at 2560 m MD is easily detected in the cuttings. The stronger samples at 2377 and 2713 m MD are from sandstone units on either side of the fault.

Chapter 3

Effect of Clay Content and Mineralogy on Frictional Sliding Behavior of Simulated Gouges: Binary and Ternary Mixtures of Quartz, Illite and Montmorillonite

Abstract

We investigated the frictional sliding behavior of simulated quartz-clay gouges under stress conditions relevant to seismogenic depths. Conventional triaxial compression tests were conducted on saturated saw-cut samples containing binary and ternary mixtures made up of quartz, montmorillonite and illite at 40 MPa effective normal stress. Microstructural observations were performed on the deformed samples to characterize the geometric attributes of shear localization within the gouge layers. Two micromechanical models were adopted to analyze the critical clay fractions for the two regime transitions based on clay porosity and packing of the quartz grains. The transition from regime 1 to 2 is associated with the shift from a stress supporting framework of quartz grains to a clay matrix embedded with disperse quartz grains, manifested by the development of P-foliation and reduction in Riedel shear angle. The transition from regime 2 to 3 is attributed to the development of shear localization in the clay matrix,

occurring only when the neighboring layers of quartz grains are separated by a critical clay thickness. We compare our mixture data on the degradation of strength with clay content against results for natural shear zone materials obtained from scientific deep drilling projects and find good correlation.

1. Introduction

The mechanical strength and stability behavior of a fault system depend on the complex interaction between numerous physical and chemical parameters including chemical composition, hydraulic properties (e.g., saturation, pore fluid composition, permeability), state of stress, and partitioning of strain in the country rock and gouge layer. One of the most important hydromechanical properties of the gouge is the coefficient of friction, defined as the ratio of shear stress to normal stress acting on the fault. Laboratory studies for a variety of rocks and minerals show the frictional strength has an approximately linear dependence on normal stress and that the friction coefficient typically ranges from 0.6 to 0.85 [*Byerlee*, 1978]. Exceptions to this trend are platy alteration and hydrated minerals, some of which can be significantly weaker than quartzo-feldspathic materials [*Lockner and Beeler,* 2002].

In recent years a number of drilling projects have been conducted to retrieve core samples from seismogenic systems in a variety of tectonic settings. Systematic mineralogical characterization of such core samples from the San Andreas Fault Observatory at Depth (SAFOD) [*Solum et al*., 2006], Taiwan Chelungpu-fault Drilling Project (TCDP) [*Kuo et al*., 2005] as well as Ocean Drilling Program (ODP) sites in the Nankai trough [*Underwood et al*., 1993, *Steurer and Underwood*, 2003, *Wilson et al*. 2003] and Cascadia basin [*Underwood*, 2002] have underscored the pervasive occurrence of clay minerals in the vicinity of fault zones and décollement. In a shear zone located at 2551 m (measured depth) penetrated during SAFOD phase 2, the retrieved cuttings have weight percentage of clay (made up of illite, chlorite, and mixed montmorillonite/illite) up to 57% and friction coefficient values down to 0.30 [*Tembe et al*., 2006; *Solum et al*.,

2006; *Morrow et al*., 2007]. In the Nankai trough the décollement sediments at ODP Sites 808 [*Underwood et al*., 1993] and 1174 [*Steurer and Underwood,* 2003] have clay contents up to 80% and friction coefficients ranging from 0.16 to 0.24 [*Kopf and Brown*, 2003].

In light of these findings it is therefore of fundamental importance in earthquake mechanics to have a more comprehensive understanding of how clay mineralogy and content influence the frictional strength and stability behavior of fault gouge, which is typically a mixture of siliciclastic and clay minerals. To be applicable to the tectonic settings, laboratory studies should be conducted preferably at stress conditions compatible to those at to seismogenic depths. However, most systematic studies of this important question have been conducted in soil mechanics at relatively low stresses on the order of 1 MPa, which would be pertinent to geotechnical problems related to slope stability and hazard assessment [*Skempton*, 1964; *Lupini et al*., 1981], but the extent to which these results can be extrapolated to higher stresses is somewhat unclear. To our knowledge the only systematic study conducted under relatively high normal stress (on the order of 10-100 MPa) was by *Logan and Rauenzahn* [1987] in a mixed assemblage of quartz and montmorillonite, a smectite clay. *Kopf and Brown* [2003] also reported data on two selected mixtures made up of quartz and 20% and 30% smectite. The primary objective of this study is to systematically investigate the frictional sliding behavior of such simulated gouges under stress conditions pertinent to seismogenic depths.

In the fourth Rankine Lecture *Skempton* [1964] critically reviewed the soil mechanics data and postulated a general correlation between the saturated residual friction and clay fraction, that is manifested by a relatively smooth transition with increasing clay content from a high friction coefficient (corresponding to that of a granular soil) to a minimum coefficient (related to sliding between low-friction clay particles). This transition was elaborated by *Lupini et al*. [1981], who observed that the overall degradation of frictional strength can be separated into three sequential regimes: (1) as the clay content increases up to 25% or so, a very moderate reduction of frictional strength would occur; (2) as the clay content further increases up to 70% or so, the

frictional strength would decrease significantly in this interval; and (3) as the soil evolves to become 100% clay, the frictional strength would again decrease rather moderately to approach a minimum value. They referred to these three regimes as "turbulent shear", "transitional" and "sliding shear", respectively. *Brown et al*. [2003] concluded that similar regimes can be identified in their low-stress data for ODP samples from Nankai as well as high-stress data of *Logan and Rauenzahn* [1987] on a binary mixture of quartz and montmorillonite.

Motivated by these observations this study was undertaken with several questions in mind. Do these three regimes of frictional strength degradation also occur in a simulated gouge made up of quartz and various clay minerals sheared at higher stresses? Are these regimes associated with distinct microstructural signatures? What is the micromechanical basis for the transitions from regime 1 to 2 and from regime 2 to 3? What are the key microstructural parameters that control the critical clay contents at these two transitions? Conventional triaxial compression tests were conducted on saturated saw-cut samples sandwiched with binary and ternary mixtures made up of quartz, montmorillonite and illite. Microstructural observations were also performed on the deformed samples to characterize the geometric attributes of shear localization within the gouge layers.

2. Methodology

2.1 Sample description and preparation

Simulated gouge mixtures used in this study were prepared from quartz, montmorillonite, and illite minerals. The quartz powder was commercially acquired Ottawa sand (>99% purity) that was crushed and sieved. Laser particle size analysis showed the size distribution to be skewed with 90% of the particles finer than 175 μm and modal grain size of 140 μm (Figure 1a). A backscattered scanning electron

microscope (SEM) image (Figure 1a inset) of the starting material showed the grains to be angular.

The montmorillonite clay was a commercially obtained sodium bentonite powder (Volclay MPS-1), the same used by *Moore and Lockner* [2007]. It has the chemical composition $Na_{0.3}(Fe^{+2},Mg)_{0.3}(Al,Fe^{+3})_{1.7}Si_4O_{10}(OH)_2 \cdot nH_2O$, with 94% of the grains being finer than 3 μm (Figure 1b). To remove adsorbed water the smectite material was dried in a vacuum oven at 100°C for 18 hours before being weighed and incorporated into a mixture.

High purity illite is difficult to obtain commercially so often a clay-bearing shale is employed [*Moore et al*., 1989; *Morrow et al*., 1992; *Brown et al*. 2003; *Saffer and Marone*, 2003]. Likewise, our illite was derived from Cambrian shale from Silver Hill, Montana supplied by Clay Minerals Society as Imt-1. The shale was predominantly made up of the disordered monoclinic illite polytype and contained 10-15 wt.% of quartz impurities. Two procedures were employed for preparation of the illite gouge. The first method was to crush and pass the shale through a 325-mesh sieve to obtain particle sizes of <43 μm for use in the mixtures (Figure 1c). In mixtures using illite obtained by this method, it was assumed that the material had a starting quartz content of 12.5±2.5 wt.% and the amount of quartz added was adjusted accordingly. The second procedure was to attain pure illite separate from the disaggregated shale by extracting the clay particle size fraction (< 5 μm) through gravity settling in a water column. Since this second method can be time consuming and yields limited quantities, only enough material was prepared for the illite end-member experiment. X-ray diffraction (XRD) analysis of the end product showed that the majority of the impurities had been eliminated leaving a relatively pure illite phase (>95%).

While it is more convenient to analyze the packing of a sand/clay mixture in terms of the volumetric clay fraction, accurately determining this value in a small sample can be problematic. A more convenient and widely used property would be the gravimetric clay fraction, which can then be converted to the volumetric component if the constituent grain densities are known. Our sample gouges were prepared from

gravimetric mixtures of the dry mineral powders. Altogether five binary mixtures of montmorillonite-quartz, four of illite-quartz, and six ternary mixtures were investigated. The ternary system used equal parts of montmorillonite and illite clays by dry weight to make up the bulk clay mineral fraction of the mixture before incorporating the quartz. Table 1 compiles the compositions of the sample gouges.

2.2 Mechanical deformation

Frictional sliding experiments were conducted at room temperature in the conventional triaxial configuration on cylindrical forcing blocks (2.54 cm diameter) containing saw-cuts inclined at 30° and filled with 1 mm-thick simulated gouge layers (Figure 2) and deformed at 40 MPa effective normal stress. The dry mixture was first prepared as a thick paste with deionized water, which was spread onto the saw-cut face of the upper forcing block, and then sandwiched by the lower block. To assure good pore pressure communication between the gouge layer and the external pore pressure system, the upper driving block was either a porous Berea sandstone (20% porosity and high permeability ~ 10^{-13} m^2) or for strong, high quartz-content gouges, a Westerly granite block that contained a small hole drilled along the sample axis. The lower driving block was granite with very low porosity (< 1%) to minimize the storage and pore pressure transients that might be generated during rapid stress changes. The assembled saw-cut sample was first jacketed with a heat shrinkable polyolefine tubing (0.9 mm wall thickness) to hold the blocks and gouge together and then dried in a vacuum oven at 80°C for a minimum of 4 hours. The dried sample was then inserted into a soft polyurethane jacket before being placed in the pressure vessel and hydrostatically loaded to a confining pressure of 41 MPa. Since the initial gouge layer applied to the saw-cut contained 50 to 60 percent water, application of confining pressure without pre-drying the sample could result in mobilization of the gouge with undesired consequences. Pre-dried gouge, however, would remain in place during application of confining pressure but would maintain significant porosity (i.e., subsequent shearing would result in gouge compaction).

The sample assembly and pore pressure lines were evacuated for 25 minutes, after which deionized water was introduced as the pore fluid and the saturated sample allowed to equilibrate for at least 1 hour at pore pressure $p_p = 1$ MPa and confining pressure of 41 MPa. Triaxial loading was then applied to the saw-cut sample, such that the saturated gouge layer would be sheared under drained conditions at a fixed normal stress of $\sigma_n = 41$ MPa and pore pressure $p_p = 1$ MPa, up to 8 mm of axial displacement (corresponding to 9.2 mm resolved on the inclined saw-cut). In each experiment, a servo-controlled axial displacement rate of 1.0 μm/s was initially applied until an axial displacement of 5.0 mm had been attained. The displacement rate was then decreased to 0.1 μm/s until a displacement of 6.0 mm at which point it was increased back to 1.0 μm/s. The confining and pore pressures were computer controlled to within ±0.05 MPa. The mechanical data were corrected for the elastic deformation of the loading system, jacket strength, and reduction in contact area between the sliding blocks during deformation, producing an uncertainty of < 0.1 MPa in shear and normal tractions.

2.3 Petrographic observations

Eleven sheared samples were impregnated with epoxy and then sawed along a plane parallel to the axial direction and perpendicular to the saw-cut plane to prepare thin-sections for standard petrographic analysis. Two of these thin sections were of relatively poor quality (Table 1). Detailed optical microscopy was performed on the other nine thin-sections using a Nikon petrographic microscope under polarized light. For each thin section, up to 37 images acquired at a magnification of 100X would be incorporated into a single mosaic (75 mm^2 in area) to map out shear localization features within the gouge layer.

3. Frictional strength and sliding behavior of gouge mixtures

3.1 Frictional sliding behavior

Our data for binary mixtures of montmorillonite/quartz and illite/quartz are presented in Figures 3a and 3b, respectively. For reference our data for the pure end-members of quartz, montmorillonite and illite are also included in these figures. The ternary mixture data are presented in Figure 3c. The frictional strength data are normalized and presented in terms of the coefficient of friction $\mu = \tau/(\sigma_n - p_p)$, where τ is the shear stress resolved on the saw-cut surface. For each sample the frictional coefficient values attained at axial displacements of 4.00 mm and 7.98 mm (corresponding to shear displacements of 4.61 mm and 9.21 mm resolved on the saw-cut) are compiled in Table 1.

Several common features were observed in the frictional sliding data. First, only stable sliding behavior was observed. Second, the friction coefficient of a sample typically attained a relatively stable value at an axial displacement of about 2 mm, beyond which strain hardening behavior manifested by a slight increase of the friction coefficient with slip was commonly observed. Third, in all three types of mixture the frictional strengths fall between the end-members of pure quartz and clay having the maximum and minimum, and there is an overall trend for the frictional strength to decrease with increasing clay content. Fourth, velocity strengthening was observed in all samples. In response to the step change in displacement rate, a relatively small change in friction coefficient was observed in all the samples, except MI35 (Figure 3c, 5 mm displacement) which showed an anomalously large irreversible strength drop when the displacement rate was lowered by an order of magnitude.

3.2 Coefficient of friction as a function of clay content

Our data on the friction coefficient values at the two displacements of 4.00 and 7.98 mm (Table 1) show that notwithstanding the hardening behavior, the increase of frictional coefficient with displacement was very small. To analyze the influence of clay

content on frictional strength, we compare the friction coefficient values measured at the same axial displacement of 7.98 mm near the end of each experiment. If we were to select data at another fixed displacement, the overall trend would be almost identical to what we present here in Figure 4. In general, uncertainty in the coefficient of friction due to machine error and reproducibility is typically ±0.005 (less than the symbol size). We use error bars on our illite samples to indicate the uncertainty in composition due to the quartz impurities.

Most previous studies have focused on the frictional sliding behavior of a binary mixture of montmorillonite/quartz. For comparison we compile in Figure 4a published data acquired under both high-stress (closed symbols) and low-stress (open symbols) conditions. Our data are qualitatively similar to the published data in that the frictional strength degradation with increasing clay content can be characterized by the three regimes postulated by *Lupini et al*. [1981]. In regime 1 (Q100, M5, M15) the strength reduction in friction coefficient as the clay content increased to 15% was so small that the strengths of the three samples were comparable to that predicted by Byerlee's law. In regime 2 (M15, M25, M50, M 75) a precipitous drop in friction coefficient from 0.679 to 0.193 was observed in four samples with clay content ranging from 15% to 75%. In regime 3 (M75, M100) the strength reduction was stabilized with a quite moderate decrease of friction coefficient to attain the minimum value of 0.126 for the 100% montmorillonite gouge.

When comparing the data, one should keep in mind a number of intrinsic and extrinsic factors that may influence the frictional strength. In regime 1 our measurements are higher than the other data. We deformed the pure quartz gouge using pairs of granite, basalt and Tennessee sandstone (as used by *Logan and Rauenzahn*, 1987) forcing blocks to test the possibility that the quartz gouge might abrade the sandstone and lead to a lower frictional strength. However, in all three cases, we observed $\mu = 0.75$ to 0.78. It is not clear why previous studies of the pure quartz end member friction, as shown in Figure 3a, range from 0.54 to 0.6. We simply note that commonly reported residual friction for quartz (i.e., *Byerlee*, 1978) is significantly higher than this. In regime 3 the

frictional behavior of the clay-rich mixture is dominated by the montmorillonite, the strength of which (in a water-saturated state) is expected to increase with increasing normal stress [*Kopf and Brown*, 2003; *Moore and Lockner*, 2007]. The frictional strength is also sensitive to fluid chemistry. *Brown et al*. [2003] and *Kopf and Brown* [2003] used sea water (roughly equivalent to a 0.5M NaCl solution) whereas *Logan and Rauenzahn* [1987], *Moore and Lockner* [2007] and our study used deionized water. We should also note that *Saffer and Maron*e [2003] and *Ikari et al.* [2007] presented frictional data on binary sand-clay mixtures, but given the partially saturated state of their simulated gouge samples it is very difficult to quantitatively compare data of water-saturated gouges with theirs [*Moore and Lockner*, 2007], and accordingly their data were not considered here.

We present in Figure 4b the data for the illite/quartz mixture. As expected the friction coefficient of the illite end-member is higher than montmorillonite. However, our value of 0.303 is appreciably lower that the friction coefficient of ~0.4 determined by *Morrow et al*. [1992] on illite gouge extracted from disaggregated shale using the "crush and sieve" method. It is likely that by extracting the very fine size fraction through gravity settling in a water column we had managed to extract an illite separate that was more pure. For comparison we also include in Figure 4b the ring-shear data of *Brown et al*. [2003] and direct-shear data of *Kopf and Brown* [2003] which consistently fall below our data, possibly due to the relatively low stress at which these measurements were conducted. Although the reduction in friction coefficient is not as pronounced as the montmorillonite/quartz mixture, three regimes can still be recognized. In the transitional regime 2 (I15, I25, I50, I88) a significant decrease of friction coefficient from 0.726 to 0.347 was observed as the clay content increased from 15% to 88%.

We present in Figure 4c the data for the ternary mixture. For the clay end-member of mixed illite/montmorillonite we measured a friction coefficient of 0.165, which fall between the montmorillonite and illite coefficients. This value is again somewhat lower than that determined by *Morrow et al*. [1992], possibly because our illite was purer and weaker. For comparison, we calculate the coefficient of friction for the ternary system from a weighted average of the binary mixture results. The calculation,

plotted as the dashed line in Figure 4c, underpredicts the friction coefficient in regime 1 and overpredicts it in regime 3. To our knowledge, there have not been any other such measurements on a ternary mixture under high stress. *Tiwari and Marui* [2005] recently reported ring-shear measurements on a ternary mixture of kaolinite, quartz and feldspar, and smectite. Since these low-stress data are not in a form that can be conveniently compared with ours, they are not included here. For the ternary mixture, three regimes of frictional strength degradation can also be recognized. In the transitional regime 2 (MI25, MI35, MI50, MI75) a significant decrease of friction coefficient from 0.756 to 0.215 was observed as the clay content increased from 25% to 75%.

3.3 Velocity dependence of frictional sliding

The velocity dependence of steady state frictional sliding can be characterized by the quantity $d\mu_{ss} / d\ln V$, were μ_{ss} denotes the steady state coefficient of friction at the slip velocity V. In the context of the rate and state dependent friction model [*Dieterich,* 1979], this quantity is given by the difference *a*-*b*, with *a* and *b* characterizing the "direct" and "evolution" effects in response to perturbations in slip velocity [*Paterson and Wong*, 2005]. Positive and negative values of $a - b = d\mu_{ss} / d\ln V$ thus correspond to velocity strengthening and weakening, respectively.

Since in each experiment we made two step changes in the loading velocity (Figure 3), the velocity dependence can be inferred from the corresponding changes in friction coefficient. We present in Figure 5 our data for the velocity dependence of the friction coefficient as a function of the clay content for the three types of mixture. The uncertainty in these estimates is typically around ±0.0004, but in certain mixtures (such as MI35 which showed an anomalously large strength drop in response to the velocity perturbation) larger error bars were involved and are so indicated. Our data for $a - b = d\mu_{ss} / d\ln V$ of all three types of gouge mixtures range from near-zero to slightly positive, in basic agreement with previous observations of *Logan and Rauenzahn's*

[1987], *Morrow et al*. [1992] and *Kopf and Brown* [2003] of velocity strengthening behavior in binary mixtures of montmorillonite/quartz and illite/quartz.

4. Microstructural observations

4.1 Description of gouge textures

We observed a number of textural features in the sheared gouge mixtures, including Riedel shear bands, boundary shears, and clay mineral fabric, which may become more or less pronounced as the gouge composition varies. To describe the texture and fabric of these gouges we will follow the notation shown in Figure 6 based on the classification scheme of *Logan et al*. [1979]. All micrographs in this paper are presented with left-lateral shear sense.

The gouge textures in our sheared montmorillonite/quartz mixtures are similar to those documented by *Logan and Rauenzahn* [1987], even though the gouge mixtures in this previous study involved somewhat more complicated loading paths. In regime 1 the montmorillonite grains are typically entrapped in the void space of the quartz particles and the gouges seem to have undergone significant shear compaction before shear localization would occur. Many of the quartz grains have been intensely comminuted with shear localization developed along R-, Y- and boundary shears. Although they share many common features, the Riedel shears in our samples are not as dense as those documented by *Gu and Wong* [1994] in an ultrafine quartz gouge. Two micrographs from the samples M5 and M15 are shown in Figure 7. The gouge layer in M5 shows an asymmetric distribution of large quartz grains with typical grain size of ~100 μm and aggregates in the upper part of the gouge and comminuted grains in the lower half. Short R-shears are present in each half but have been cross-cut by the Y-shear. In this sample strain concentrates along Y-shears, which separate coarser particles from a finer matrix. It may be that most of the sliding is initially accommodated at the interface of the country rock and gouge, thus developing a thick boundary shear of finer material. Textures from this first regime are diagrammatically represented as *texture A* in Figure 7.

In regime 2 the quartz grains in the gouge mixture have a tendency to congregate in the middle of the gouge layer, away from the boundaries and often surrounded by R-shears. In comparison to samples sheared in regime 1, the quartz grains show appreciably less comminution or microcracking. At higher magnification there is a noticeable particle size gradation near the R- and boundary shears with finer quartz and clay particles entrained in the shear and larger, less deformed grains further away. A clay foliation in the P-orientation is often observed to develop at 155-160° to the shear direction in these samples. In most samples several continuous R-shears could be observed, indicating that they might have been active towards the end of the experiment. Many of the samples contain Y- and P-shear bands that link discontinuous Riedel shears. We classify these microstructure as belonging to *texture B*. As indicated by the arrows in sample M50 (Figure 7) many of the quartz grains are relatively intact with little cracking and they are surrounded by the clay particles. The clay has also migrated to the country rock-gouge interface to form a thin boundary shear, with very few Y-shears present. We had very limited observations on montmorillonite samples from regime 3, but *Logan and Rauenzahn* [1987] reported "discontinuous alignment of grains" and "little fracturing of quartz" in a sample with 75% montmorillonite. They also observed "pervasive alignment of clay grains" in the R_1 and Y orientations.

Our observations on illite/quartz and the ternary mixture indicate that their gouge textures are qualitatively similar to those of montmorillonite/quartz in each of the three regimes. This is illustrated by a micrograph of MI25 from regime 1 and micrographs of MI35 and I50 in regime 2. It should also be noted that deformation features documented by *Moore et al*. [1989] in sheared heated illite gouges are quite similar to *Logan and Rauenzahn's* [1987] observations on 100% montmorillonite.

4.2 Orientation of Riedel shear localization

Although the densities of Riedel shear in our samples are relatively low, we were able to characterize the orientation of R-shears in selected samples with clay contents between 5% and 50%. We measured the angle α of the R_1 shear with respect to the

boundary between the gouge and country rock (Figure 6), and the data are plotted as a function of the clay content in Figure 8. While the samples with low clay content show greater scatter, there is an overall trend for the Riedel shear angle to decrease with increasing clay content in association with the transition from regime 1 to regime 2.

Such a decrease of Riedel shear angle can be attributed to reduction of the bulk strength of the gouge mixtures [*Gu and Wong*, 1994]. If the gouge can be approximated as a non-cohesive material with its pressure-dependent bulk strength characterized by an angle of internal friction μ_i, then stress equilibrium at the interface of the country rock and gouge layer would constrain the limiting state of stress and principal stress orientations within the gouge layer at the onset of Riedel shear localization, which in turn determine the orientations of the Riedel shears. In particular *Gu and Wong* [1994] derived the following expression for the orientation of the R_1-shear:

$$\alpha = \frac{\pi}{4} - \frac{1}{2}\tan^{-1}\left(\frac{\mu}{-\mu_i^2 + (1+\mu_i^2)\sqrt{1-(1+\mu^2)/(1+\mu_i^2)}}\right) + \frac{\tan^{-1}\mu_i}{2} \qquad (1)$$

We plot in Figure 9 this theoretical prediction of the Riedel shear angle as a function of the friction coefficient μ (corresponding to the ratio between the shear and normal stresses resolved at the rock-gouge interface) for fixed values of the internal friction coefficient μ_i. For comparison we plot our gouge mixture data on the mean value of the angle α as a function of friction coefficient μ. Data in regimes 1 and 2 are shown in open and dark symbols, respectively. We also include the data of *Gu and Wong* [1994] for a highly sheared coarse quartz gouge (sample WGQP17) and of *Moore et al.* [1989] for heated Fithian shale (made up of 80% illite). Comparison of the laboratory data and theoretical prediction suggest that the transition from regime 1 to 2 is associated with a decrease in the bulk strength of the gouge mixtures, corresponding to a reduction of the internal friction coefficient from >0.8 to <0.6.

A limitation of this mechanical interpretation should be noted. The equilibrium condition and therefore equation (1) should strictly apply only in the vicinity of the rock-gouge interface with the implicit assumption that shear localization develops along planar

features, whereas the Riedel shears are often curvilinear and the angle measurements typically made near the mid-section of the gouge layer.

5. Discussion

Our results on the frictional strength of binary and ternary mixtures of quartz, montmorillonite and illite show that the degradation of frictional strength as a function of increasing clay content in saturated gouge under high stresses is characterized by three regimes, that are phenomenologically similar to soil mechanics results obtained under relatively low stresses. In regime 1 a very moderate reduction of frictional strength occurs as the clay content increases up to 25% or so. In regime 2 a significant reduction in frictional strength occurs as the clay content increase up to 70% or so. In regime 3 the frictional strength would again decrease rather moderately to approach a minimum value corresponding to that of the 100% clay end-member. While these three regimes can be identified in the data, it can also be seen from our normalized friction coefficient data (Figure 10) that there are differences among the three simulated gouge mixtures. Although the transition from regime 1 to 2 seems to occur at a clay fraction between 15% and 25% in the two binary mixtures, the other set of data suggest a higher clay fraction of >25% for the ternary mixture. While the strength reduction in regime 3 was very moderate in the montmorillonite/quartz and ternary mixtures, it was appreciably higher in the illite/quartz mixture. A more refined characterization of the three regimes and the two transitions would warrant a significantly more comprehensive laboratory study that is beyond the scope of the present investigation.

Our microstructural observations have identified certain shear localization fabrics that are characteristic of these three regimes of frictional strength degradation. Since sand grains may be larger than clay particles by several order of magnitude, in a sandy mixture with low clay content (such as our gouge mixtures in regime 1) the clay minerals would tend to collect in the voids of the larger framework quartz grains and accordingly the applied stresses are primarily accommodated by force network chains that connect the

contacting quartz grains. Consequently the presence of small amount of clay in such a mixture has a minor influence on the frictional strength and gouge fabric in regime 1, which we observe to be quite similar to those in a granular gouge solely made up of siliciclastic minerals. As the clay content increases to beyond a critical fraction the voids are completely occupied by the clays, inducing the quartz grains to disperse within an interconnected clay matrix. This allows the possibility of development of clay foliation as a gouge failure mode, and as clay content increases this shear localization mechanism evolves to become dominant in regime 2. Due to the significant contrast in frictional strength between the clay and quartz, the overall friction coefficient would undergo significant reduction with this development. Since quartz particles are embedded in the clay matrix, they act as high-strength "barriers" for the development of through-going Riedel shears within the clay even though the matrix is interconnected. As the clay content further increases it becomes less likely for the development of shear localization within the clay matrix to be impeded by the quartz barriers, and ultimately in regime 3 the quartz barriers play such a minor role that the failure mode is predominately due to Riedel shear localization in the clay. As a result the friction coefficient in regime 3 is comparable to that in a pure clay gouge.

Lupini et al. [1981] recognized the three regimes of strength degradation, which they referred to as "turbulent shear", "transitional" and "sliding shear". In this study we have avoided the use of this somewhat misleading terminology. The term "turbulent shear" may imply the absence of any patterning of strain such as Riedel shear localization, which is actually an important mechanism of gouge failure involving the stress-supporting quartz framework in regime 1. To associate regime 3 with "sliding shear" would suggest that this is a mechanism that applies only to clay, thus ruling out localized shear slip along Riedel bands in the quartz matrix that occurs in regime 1.

5.1 Ideal packing model for the transition in frictional strength degradation from regime 1 to 2

On the basis of our friction and microstructural data, we present in Figure 11 a conceptual model of how the grain packing and modes of shear localization evolve from regime 1 to regime 3 with increasing clay content. Since the two transitions (from regime 1 to 2 and from regime 2 to 3) involve similar values of critical clay fractions in all three gouge mixtures investigated suggests that there are common microstructural attributes controlling these transitions.

The transition from regime 1 to 2 is associated with a qualitative change in the grain packing, from a mixture with an interconnected framework of quartz grains supporting the applied stresses to one with an interconnected clay matrix. Such a transition can be analyzed using results from powder technology on the packing of a binary mixture of fine and coarse particles [*McGeary*, 1961; *Cumberland and Crawford*, 1987], which have provided useful insights into the mechanical compaction, seismic velocity and permeability of a sand-clay mixture as functions of porosity and pressure [*Marion et al*., 1992; *Koltermann and Gorelick*, 1995; *Revil et al*., 2002].

According to this ideal packing model, the mixture in regime 1 can be considered to form in two steps. The quartz grains are first assembled to form an interconnected, stress-supported framework that has an interstitial void space with porosity ϕ_s. The clay particles are then randomly added into the void space without disturbing the pre-existing quartz framework. As the clay content increases, a point will be reached when all the interstitial space has been filled, and further addition of clay particles necessitate the breakage of existing quartz grain contacts, which would enhance the connectivity among the clay grains and development of an interconnected clay matrix at the inception of regime 2. If we define the volumetric clay fraction *c* as the ratio of the volume of dry clay (which includes the volumes of solid clay grains and pore space) to that of the dry gouge mixture, then one would conclude that the transition from regime 1 to 2 occurs when clay grains fill up all the interstitial volume corresponding to the porosity ϕ_s, that is when

$$c = \phi_s \tag{2}$$

In most laboratory studies the clay content is characterized by the weight or gravimetric fraction w_c, which is related to the volumetric clay fraction c by

$$w_c = \frac{c(1-\phi_{cl})}{c(1-\phi_{cl}) + (1-\phi_s)(\rho_s / \rho_{cl})} \quad \text{for} \quad c \le \phi_s \tag{3a}$$

$$w_c = \frac{c(1-\phi_{cl})}{c(1-\phi_{cl}) + (1-c)(\rho_s / \rho_{cl})} \quad \text{for} \quad c \ge \phi_s \tag{3b}$$

where ϕ_{cl} denotes the porosity of the dry clay grains, and ρ_s and ρ_{cl} denote the grain densities of quartz and clay, respectively [*Marion et al*., 1992]. We will follow *Revil et al.* [2002] to take $\rho_s \approx \rho_{cl} \approx$ 2650 kg m^{-3} and accordingly assume $\rho_s / \rho_{cl} = 1$. This assumption is applicable here since we determined the weight fraction on clay minerals that had been dried in vacuo under elevated temperature to get rid of their bound water. If the clay minerals had water adsorbed on the surface, the density ρ_{cl}, could be appreciably lower.

The gravimetric clay fraction at the transition from regime 1 to 2 corresponding to the critical condition (2) is given by

$$w_{cr} = \frac{(1-\phi_{cl})}{(1-\phi_{cl}\phi_s)}\phi_s \tag{3c}$$

According to this ideal packing model, the critical gravimetric clay fraction at the transition from regime 1 to 2 depends only on the initial quartz packing (characterized by ϕ_s) and clay porosity (characterized by ϕ_{cl}). Its value is always smaller than the critical volumetric fraction $c = \phi_s$. An increase in pressure or normal stress will decrease both ϕ_s and ϕ_{cl}, but since the decrease in clay porosity is typically more pronounced than the quartz porosity, one expects the critical gravimetric fraction w_{cr} to slightly increase with increasing pressure or normal stress.

While clay is highly porous at ambient conditions, its porosity may collapse resulting in significant porosity reduction under pressure. However, there is a paucity of

data on clay porosity at high pressure. Some of the best data are for saturated kaolinite obtained by *Marion et al*. [1992], who reported a drastic reduction of porosity from an initial value of 62% to 24% at an effective pressure of 40 MPa. Guided by their data, if we assume that in our gouge mixtures the clay porosity ϕ_{cl}=0.24, then our binary mixture data which indicate a critical weight fraction of ~20% (an intermediate value between 15% and 25%) would imply that the stress-bearing quartz framework had a porosity of $\phi_s \approx 25\%$. For comparison *Marion et al*. [1992] determined a porosity value of 33% and *Zoback and Byerlee* [1976] reported values of 22% and 23% for hydrostatically stressed Ottawa sand at an effective pressure of 40 MPa. Even though our quartz gouges were more angular than Ottawa sand and likely to be more porous than Ottawa sand under ambient conditions, our microstructural observations also indicate pervasive shear-enhanced compaction associated with comminution and microcracking in quartz that might significantly reduce the porosity of the quartz framework.

If we were to consider the mixed clay (of illite and montmorillonite) as one single component in a binary mixture, then according to (3c) our ternary mixture data which indicate a critical weight fraction of ~30% (an intermediate value between 25% and 35%) would imply a very low clay porosity of <10%. The ideal packing model of a binary mixture may be of limited applicability in this context, and indeed the analysis can be extended to a ternary system [*Cumberland and Crawford*, 1987], but given the paucity of constraints on the additional parameters, the use of a more involved analysis is unlikely to provide insights into our ternary mixtures data.

For a binary mixture at the critical condition (2), the ideal packing model predicts a minimum in porosity and a maximum in the P-velocity as functions of clay content at a fixed effective pressure [*Marion et al*., 1992; *Revil et al*., 2002], and this represents the only transition of importance for a sand-clay mixture under hydrostatic loading. Under shear loading, this transition is manifested by an accelerated decrease of frictional strength, corresponding to the transition between regime 1 to 2. However, under nonhydrostatic loading there is an additional transition from regime 2 to 3 related to

Riedel shear localization in the interconnected clay matrix that can develop when the quartz particles are sufficiently disperse at a relatively high clay fraction.

5.2 Critical clay layer thickness for the transition in frictional strength degradation from regime 2 to 3

To analyze this second transition we will expand on an idea postulated by *Lupini et al.* [1981] that the inception of regime 3 hinges on the attainment of a critical thickness for the clay layer that separates two neighboring layers of sand grains. First order estimates of the geometric attributes involved can be derived for the idealized model of monodisperse spheres randomly (Figure 12a) or regularly packed (Figure 12b). We will first derive the results for the random case using *Chandrasekhar's* [1943] elegant result that the mean of the nearest neighbor distance between a random distribution of particles

$$\lambda = \Gamma(4/3)/(4\pi n/3)^{1/3} = 0.554 n^{-1/3} \tag{4a}$$

where Γ is the factorial function and n denotes the number of particles per unit volume. If we assume that the particles are quartz with a mean diameter d, then the volumetric fraction of quartz is $\pi n d^3/6$ and the volumetric clay fraction is $c = 1 - \pi n d^3/6$ which implies that

$$n = \frac{6}{\pi}\frac{(1-c)}{d^3} \tag{4b}$$

Substituting (4b) into (4a) we obtain

$$\lambda = 0.554 d \left(\frac{\pi}{6(1-c)}\right)^{1/3} \tag{4c}$$

The minimum requirement for the existence of a continuous clay layer between nearest neighbors of quartz particles is $\lambda > d$, which from (4c) requires $c >$ 1- (π/6) 0.554^3 =0.911. While this is a rather general result, it provides an estimate that is overly conservative in that our observations indicate that the transition from regime 2 to 3 occurs at a critical clay fraction appreciably lower than 91%.

This suggests that we should consider a more close-packed configuration. As a first example we will consider monodisperse spheres (with diameter *d* and radius *r*=*d*/2) in a hexagonal close-packed (HCP) assemblage (Figure 12b). With the spherical quartz grains in contact (corresponding to the scenario at the transition from regime 1 to 2) the unit cell volume for HCP is $V = 4\sqrt{2}r^3$, and since the volume of the sphere is $4/3\pi r^3$ the clay volume is $V - 4/3\pi r^3$ and the volumetric clay fraction is $c = \phi_s = 1 - \pi/(3\sqrt{2}) = 0.26$ [*Cumberland and Crawford*, 1987; *Mavko et al*., 1998]. We note that this value is close to the estimate of $\phi_s \approx 25\%$ for our binary mixtures at the transition from regime 1 to 2. To analyze the progressive increase of clay content in regime 2 we will assume that the clay increments are distributed homogenously and model it as the superposition of two steps. In the first step we consider a uniform dilation of the system so that the linear dimension is increased by a factor of α >1. This dilation results in solid grains with radius $R = \alpha r$ embedded in unit cells of volume $V = 4\sqrt{2}R^3$. In the second step the solid grains are allowed to shrink back to the initial radius of *r,* and the void space created is filled with clay. At the end of these two steps, the volume of the sphere remains $4/3\pi r^3$, but the volumetric clay fraction has increased to

$$c = 1 - \frac{\pi}{(3\sqrt{2})}\left(\frac{r}{R}\right)^3 = 1 - 0.740/\alpha^3 \qquad (5a)$$

For a given α equations (5a) and (3b) can used to calculate the gravimetric clay fraction w_c. A clay layer of uniform thickness will now separate two adjacent layers of spherical grains in such a regular packing. At the end of the first step (with the dilated grains in contact with one another), the layer spacing in the HCP system of spherical grains is $2\sqrt{2/3}R$ [*Cumberland and Crawford*, 1987]. After the grains have contracted back to radius *r* in the second step, a clay layer of uniform thickness $\delta = 2\sqrt{2/3}R - 2r = 2(\sqrt{2/3}\alpha - 1)r$ is incorporated to fill in the gap. *Lupini et al*. [1981] proposed using the ratio $\delta/d = \delta/(2r)$ as the geometric parameter that controls the transition from regime 2 to 3. From soil mechanics data they suggested a critical ratio of

0.1-0.4 for this transition to occur. Specifically for the HCP system we analyze here, this ratio is given by

$$\delta / d = \sqrt{2/3}\alpha - 1 = 0.816\alpha - 1 \quad (5b)$$

As a second example we consider the simple cubic (SC) packing which is relatively loose. For this configuration with volume $V = 8r^3$ and layer spacing $2r$ the volumetric clay fraction and normalized clay layer thickness are given by

$$c = 1 - \pi/(6\alpha^3) = 1 - 0.524/\alpha^3 \quad (6a)$$

$$\delta / d = \alpha - 1 \quad (6b)$$

We plot in Figure 12 the normalized clay layer thickness δ / d as a function of w_c for these two packing arrangements, taking $\phi_{cl} = 0.24$ in equation (3b), and c in equations (5a) and (6a) for the HCP and SC configurations, respectively. According to this model our observations of a critical weight fraction of ~70% imply a normalized clay layer thickness δ / d = 0.18 and 0.30 for the HCP and SC configurations, respectively. Since we have assumed a homogeneous distribution of clay our analytic estimates probably underestimate the thickness of clay along which continuous Riedel shears may develop, in light of our microstructural observations that the spatial distribution of quartz grains can be quite heterogeneous in all the shear gouge mixtures. Our model idealizes the quartz grains as monodisperse spheres, and it is plausible that thicker clay layers can readily develop in a less sorted system made up of angular grains.

A common feature of the ideal packing model and critical clay thickness model is that they both predict the critical clay fraction for the transition from regime 1 to 2 and from 2 to 3 to be primarily influenced by the clay porosity and packing characteristics of the quartz grains. This implies that the transitions (particularly regime 1 to 2) are also dependent on the particle size distribution of the constituent minerals, which would evolve with strain. For example, if we consider a shear zone containing a sand-clay gouge with a homogenous distribution of coarse sand grains at the beginning of its deformation history, the regime transitions would occur at the critical clay contents predicted by the analyses. A snapshot of the gouge at a latter point would show cataclasis and grain size reduction of the sand, producing a non-homogeneous particle size

distribution with an overall shift towards the clay-size fraction. The effect on porosity and packing of this evolved sand-clay mixture would result in regimes transitions at slightly different clay critical contents than in the initial state.

5.3 Ternary diagram for frictional strength of simulated gouge mixtures

Our data on binary and ternary mixture are compiled in Figure 14a. The black circles represent the compositions of the experimental run. Each point is associated with a friction coefficient (the same shown in Figure 4) which was then used to manually fit contours of friction coefficient for the quartz-clay system. One can visualize the friction coefficient to be a 3D surface that overlies the mineralogy plot with a peak at the quartz end-member and a valley at the montmorillonite end-member. The three micromechanical regimes are also shown and the transitions between them is discernible as the clustering (as in the transition from 1 to 2) or dispersion (as in the transition from 2 to 3) of contours.

5.4 Application to fault zones

Pervious studies have inferred the mechanical properties of shear zones from surface and shallow borehole samples [e.g., *Morrow et al*., 1982], and pure mineral analogs [e.g., *Morrow et al.,* 1992; *Moore et al.*, 1996]. In recent years several drilling projects have investigated active fault zones in a variety of tectonic settings and retrieved core for laboratory study. To assess the extent to which our laboratory data on simulated gouge mixtures can be applied to natural samples, we compile data in Figure 14b for clay-rich fault gouge obtained by deep drilling programs for 3 major shear zones: the San Andreas fault, Chelungpu fault, and Nankai décollement. The compositions of the samples are represented by the shaded areas and are detailed below. Where possible we have also included the friction coefficient determined by high-pressure friction experiments of gouge samples retrieved from these drilling sites (denoted by squares). Coincidence of the shaded area with the squares implies the frictional strength can be

estimated fairly accurately from our data on simulated gouges if gouge composition is known.

The San Andreas Fault Observatory at Depth (SAFOD) penetrated the creeping section of the fault in 2006 and is currently probing a region of repeating seimicity. The SAFOD main hole passed through numerous shear zones, including at least one actively deforming trace of the San Andreas fault. *Solum et al.* [2006] distinguished 5 shear zones from bulk mineral assemblages sampled in drill core and cuttings collected during the project's first two phases. Of these only three, from 2545-2560 m measured depth (MD), a minor strand of the southwest fracture zone of the SAF at 3067 m MD, and the inferred actively deforming zone at 3310-3353 m MD [*Hickman et al*., 2005], were abundant in illite, chlorite, and mixed layer illite-smectite clay phases. The remaining two shear zones were enriched in laumontite and contained only trace amounts of clay so they were not included in our diagram. Although it is unclear how chlorite would behave in a mixture without further investigation, given that the friction coefficient of chlorite is ~ 0.4 under saturated conditions [*Morrow et al*., 2000] we felt it more appropriate to lump it with the illite fraction rather than the montmorillonite. Undoubtedly, there will be some error in estimating the friction coefficient in Figure 14b. For comparison we show data from saw-cut frictional sliding tests conducted by *Morrow et al.* [2007] and *Tembe et al*. [2007] on SAFOD gouge materials at 40 MPa effective normal stress. The shaded areas indicate mineralogy determined by XRD analyses [*Solum et al*., 2006, *Morrow et al*., 2007], while the squares represent friction data. Samples A and C from 2551 and 3322 m MD contained up to 27 wt.% chlorite and were obtained using a method developed by *Morrow et al*. [2007] in which only drill cuttings containing slickensides were tested. This ensured the weak shear zone material would not be diluted by the surrounding bulk material and in doing so, yielded data better representative of the shear zone. *Tembe et al.* [2007] investigated the frictional behavior of the 3067 m MD SAFOD drill core (plotted as sample B) which contained 62-69% illite and mixed illite/smectite phases. Velocity strengthening behavior was reported for all the SAFOD samples. Overlapping of the

squares with the shaded area validates the premise of our mixing study and implies the frictional strength can be estimated from mineralogical analyses.

The Taiwan Chelungpu-fault Drilling Project (TCDP) drilled two boreholes into the Chelungpu fault that was ruptured 1999 Mw7.6 Chi-Chi earthquake. Two potential shear zones for slip in the 1999 event were identified at 1111 m and 1153 m in TCDP Hole A. The core samples for these depths are included in Figure 14 as samples D and E, respectively. *Kuo et al.* [2005] conducted XRD clay mineral analyses of the shear zone materials. They reported a thin black layer rich in smectite and illite in the fault core at 1111 m. All other clay phases are absent or present at low concentrations. Although illite and chlorite were present in the deeper shear zone, smectite and kaolinite phases were entirely absent. In Figure 14 we have used a shaded ellipse to indicate the composition of the fault cores. *Lockner* [*personal communication*, 2007] conducted triaxial saw-cut tests on water saturated gouge from FZ1111 at obtained friction coefficients of 0.5 and 0.7 at high normal stress.

The Nankai décollement has been extensively studied by the Ocean Drilling Program (ODP) and Deep Sea Drilling Program (DSDP) and much like the San Andreas, shares the common attribute of appearing extremely weak despite being locked through much of its length. The Nankai accretionary prism was formed by the subduction of the Philippine Plate (Shikoku Basin) following periods of seafloor spreading and volcanism [*Shipboard Scientific Party,* 2001a and references therein]. Mineralogy may be an important factor in controlling fault strength since the basal décollement of the Nankai accretionary wedge occurs in lower Shikoku Basin facies, consisting of hemipelagic mudstones and claystones, volcanic ash and the replacement of vitrified glass with smectite and zeolites [*Shipboard Scientific Party,* 2001b]. The décollement was penetrated near the toe of the subduction zone at ODP Sites 808 and 1174 at depths of 945-964 m below sea floor (mbsf) and at 808-840 mbsf, respectively. *Underwood et al*. [1993] found illite to be the dominant clay phase with total clay fraction ~30 wt.% at Site 808, whereas Site 1174 about 250 km away was reported to have up to 90% clay [*Steurer and Underwood*, 2003]. Ring shear experiments on ODP décollement zone samples at

pressures <2 MPa by *Kopf and Brown* [2003] obtained values of ~0.2, in general agreement with our estimates at 40 MPa for clay-rich shear zone.

The samples included in Figure 14b are from mature fault zones and largely belong to the Regime 2 (20-70% clay), in which strength degradation is greatest and the development of foliation as a failure mode is active. In this regime, the frictional strength deviates considerably from the prediction of Byerlee's law for a gouge dominated by siliciclastic minerals with relatively low clay content. This is also the regime in which the frictional strength is highly sensitive to variations in clay content. In this study we restrict ourselves to room temperature conditions, however a deeper understanding of these related phenomena requires systematic experiments at a range of elevated pressure and temperature conditions relevant to seismogenic depths. Likewise extending the study to other clay systems, such as kaolinite, chlorite, and micas would be worthwhile.

6. Summary and Conclusions

We systematically investigated the frictional sliding behavior of simulated quartz-clay gouges at seismogenic stress conditions. Conventional triaxial compression tests were conducted on saturated saw-cut samples containing binary and ternary mixtures made up of quartz, montmorillonite and illite. Microstructural observations were performed on the deformed samples to characterize the geometric attributes of shear localization within the gouge layers. We observed the degradation of frictional strength with increasing clay content from 0.7 to 0.1, and identified the involvement of three micromechanical regimes. Regime 1 occurred in mixtures with <20 % clay, regime 2 at 20-70 % clay, and regime 3 at >70 % clay content. Two micromechanical models were adopted to analyze the transitions from 1 to 2 and from 2 to 3. The first transition follows from the ideal packing model and is associated with the shift from a stress supporting framework of quartz grains to a clay matrix supporting framework. In the microstructure the transition is manifested by the development of P-foliation and a reduction in Riedel shear angle. The second transition (from regime 2 to 3) is attributed to the development

of shear localization in the clay matrix which can develop only when the nearby layers of quartz grains are sufficiently separated. Analytic estimates of the critical clay thickness between neighboring quartz grains were obtained from a conceptual model in which the gouge is treated as an assemblage of randomly or regularly packed quartz grains embedded in a clay matrix.

Data collected on synthetic gouge mixtures were used to infer the frictional strength of clay shear zone materials obtained from scientific deep drilling projects based on composition. The natural gouges when compared with our mixing relations were estimated to be moderately weak to strong and mostly belonged to regime 2. Experiments conducted at high pressures on the natural samples obtained friction coefficients that are in accord with our estimates.

Acknowledgments

We have benefited from discussions with Diane Moore. We also thank Carolyn Morrow for her assistance in the lab and John Solum for conducting the XRD analyses. Li-Wei Kuo and Sheng-Rong Song shared with us their TCDP data. Brian Crawford kindly provided us with his unpublished manuscript on kaolinite-quartz mixtures. ST was supported by a Department of Education GAANN fellowship. This research was partially supported by US National Science Foundation under grant EAR-0346022.

References

Brown, K.M., A. Kopf, M.B. Underwood, and J.L. Weinberger (2003), Compositional and fluid pressure controls on the state of stress on the Nankai subduction thrust: A weak plate boundary, *Earth and Planetary Science Letters, 214*, 589-603, doi:10.1016/S0012-821X(03)00388-1.

Byerlee, J.D., (1978) Friction of rocks, *Pure and Applied Geophysics*, 116, 615-26.

Chandrasekhar, S., (1943), Stochastic problems in physics and astronomy, *Reviews of Modern Physics*, 15 (1), 1-89.

Cumberland, D.J. and R.J. Crawford, (1987), The Packing of Particles, Elsevier, Amsterdam, p. 148.

Dieterich, J.H. (1979), Modeling of rock friction, 1, Experimental results and constitutive equations, 2, Simulation of preseismic slip, *J. Geophys. Res.,* 84, 2161-2168, 2169-2175.

Gu, Y., and T.-f. Wong (1994), Development of shear localization in simulated quartz gouge: Effect of cumulative slip and gouge particle size, *Pure Appl. Geophys., 143*, 387-424.

Ikari, M.J., D.M. Saffer, and C. Marone, (2007), Effect of hydration state on the frictional properties of montmorillonite-based fault gouge, *J. Geophys. Res*., 112, B06423, doi:10.1029/2006JB004748.

Koltermann, C.E., and S.M. Gorelick, (1995), Fractional packing model for hydraulic conductivity derived from sediment mixtures, *Water Resources Research*, 31(12), 3283–3297.

Kopf, A, K. M. Brown, (2003), Friction experiments on saturated sediments and their implications for the stress state of the Nankai and Barbados subduction thrust, *Marine Geology*, 202, no.3-4, 193-210.

Kuo, L., S. Song, H. Chen (2005), Characteristics of Clay Minerals in the Fault Zone of TCDP and its Implications, *Eos Trans. AGU, 86*(52), Fall Meet. Suppl., Abstract T43D-05.

Lockner, D.A., and N.M., Beeler (2002), Rock failure and earthquakes-Chapter 32, in *International Handbook of Earthquake and Engineering Seismology*, edited by W.H.K. Lee, H. Kanamori, P.C. Jennings, and C. Kisslinger, 505-537, Academic Press, Amsterdam.

Logan, J.M., M. Friedman, N. Higgs, C. Dengo, T. Shimamoto (1979) Experimental studies of simulated gouge and their application to studies of natural fault zones, in *Analyses of Actual Fault Zones in Bedrock. US Geol. Surv. Open File Rep*. 1239:305–43.

Logan, J.M., and K.A. Rauenzahn, (1987) Frictional dependence of gouge mixtures of quartz and montmorillonite on velocity, composition and fabric. *Tectonophysics*, 144:87–108.

Lupini, J.F., A.E. Skinner, and P.R. Vaughan (1981), The drained residual strength of cohesive soils, *Géotechnique, 31,* (2), 181-213.

Marion, D., A. Nur, H. Yin, and D. Han (1992), Compressional velocity and porosity in sand-clay mixtures, *Geophysics, 57*, 554-363.

Mavko, G., T. Mukerji, and J. Dvorkin, (1998), The Rock Physics Handbook: Tools for Seismic Analysis in Porous Media, 147-161, Cambridge University Press,.

McGeary, R.K., (1961), Mechanical packing of spherical particles, *Journal of the American Ceramic Society*, 44(10), 513-22.

Moore, D. E., R. Summers, J.D. Byerlee (1989), Sliding behavior and deformation textures of heated illite gouge, *J. Struct. Geol., 11,* (3) 329-342.

Moore, D. E., Lockner, D. A., Summers, R., Ma, S., and Byerlee, J. D. (1996), Strength of chrysotile-serpentinite gouge under hydrothermal conditions: Can it explain a weak San Andreas fault?, *Geology*, 24, 1041–1044.

Moore, D.E. and D.A. Lockner (2007), Friction of the smectite clay montmorillonite: A review and interpretation of data, in Dixon, T. H., and Moore, J. C., eds., The Seismogenic Zone of Subduction Thrust Faults, MARGINS Theoretical and Experimental Earth Science Series, 2, in press.

Morrow, C. A., L. Q. Shi and J. D. Byerlee, (1982), Strain hardening and strength of clay-rich fault gouges, *J. Geophys. Res*., 87, 6771-6780.

Morrow, C.A., B. Radney, and J.D. Byerlee, (1992), Frictional strength and the effective pressure law of montmorillonite and illite clays, in *Fault Mechanics and Transport Properties of Rocks*, ed. B. Evans, and T.-f. Wong, 69-88, Academic Press, San Diego.

Morrow, C., J. Solum, S. Tembe, D. Lockner, and T.-f. Wong, (2007), Using drill cutting separates to estimate the strength of narrow shear zones at SAFOD, *Geophys. Res. Lett., 34,* L11301, doi:10.1029/2007GL029665.

Paterson, M.S., and T.-f. Wong, (2005) Friction and Sliding Phenomena, in *Experimental deformation-The brittle field*, Springer, New York, 165-210.

Revil, A., D. Grauls, and O. Brévart, (2002), Mechanical compaction of sand/clay mixtures, *J. Geophys. Res*., 107, B11, 10.1029/2001JB000318.

Saffer, D.M, and C. Marone (2003), Comparison of smectite- and illite-rich gouge frictional properties: application to the updip limit of the seismogenic zone along subduction megathrusts. *Earth Planet. Sci. Lett*., 215, 729-736.

Shipboard Scientific Party, (2001a) Leg 190 Summary, *In* Moore, G.F., Taira, A., Klaus, A., et al., *Proc. ODP, Init. Repts.,* 190: College Station, TX (Ocean Drilling Program), 1–87. doi:10.2973/odp.proc.ir.190.101.2001.

Shipboard Scientific Party, (2001b) Site 1174, *In* Moore, G.F., Taira, A., Klaus, A., et al., *Proc. ODP, Init. Repts.,* 190: College Station, TX (Ocean Drilling Program), 1–149. doi:10.2973/odp.proc.ir.190.105.2001.

Skempton, A.W. (1964), Long-term stability of clay slopes, *Géotechnique, 14,* 77–102.

Solum, J.G., S.H. Hickman, D.A. Lockner, D.E. Moore, B.A. van der Pluijm, and J.P. Evans, (2006), Mineralogical characterization of protolith and fault rocks from the SAFOD main hole. *Geophys. Res. Lett., 33,* L21314, doi:10.1029/2006GL027285.

Steurer, J.F., and M.B. Underwood, (2003), Clay Mineralogy of Mudstones from the Nankai Trough Reference Sites 1173 and 1177 and Frontal Accretionary Prism Site 1174, In Mikada, H., Moore, G.F., Taira, A., Becker, K., Moore, J.C., and Klaus, A. (Eds.), Proc. ODP, Sci. Results, 190/196, 1–9, doi:10.2973/odp.proc.sr.190196.211.2003.

Tembe, S., D.A. Lockner, J.G. Solum, C.A. Morrow, T.-f. Wong, D.E. Moore (2006), Frictional strength of cuttings and core from SAFOD drillhole phases 1 and 2, *Geophys. Res. Lett*., 33, L23307, doi:10.1029/2006GL027626.

Tiwari, B., AMASCE, and H. Marui, (2005), A new method for the correlation of residual shear strength of the soil with mineralogical composition, *J. Geotech. Geoenv. Eng., 31*, (9), doi:10.1061/(ASCE)1090-0241(2005)131:9(1139).

Underwood, M.B., K. Pickering, J.M. Gieskes, M. Kastner, and R. Orr, (1993) Sediment geochemistry, clay mineralogy, and diagenisis: A synthesis of data from Leg 131, Nanakai Trough, In Hill, I.A., Taira, A., Firth, J.V., et al., Proc. ODP, Sci. Results, 131: College Station, TX (Ocean Drilling Program), 343-363.

Underwood, M.B., (2002), Strike-parallel variation in clay mineralogy, fault vergence, and up-dip limits to the seismogenic zone, *Geology*, 30, 155-158.

Wilson, M.E.J., S. Hirano, C.L. Fergusson, J. Steurer, and M.B. Underwood (2003) Data Report: Sedimentological and Petrographic Characteristics of Volcanic Ashes and Siliceous Claystones (Altered Ashes) from Sites 1173, 1174, and 1177, Leg 190, In Mikada, H., Moore, G.F., Taira, A., Becker, K., Moore, J.C., and Klaus, A. (Eds.), Proc. ODP, Sci. Results, 190/196, 1–9.

Zoback, M. D., and J. D. Byerlee (1976), Effect of high-pressure deformation on permeability of Ottawa Sand, *AAPG Bulletin*, 60, 1531-1542.

Table 1. Description of samples studied.

Sample	Gouge Composition (weight %)			Thin Section	Texture (from Fig. 7)	Coefficient of Friction	
	Montmorillonite	*Illite*	*Quartz*			*4.00 mm*	*7.98 mm*
Q 100	0	0	100			0.749	0.698
M 5	5	0	95	x	A	0.734	0.705
M 15	15	0	85	x	A	0.679	0.647
M 25	25	0	75	x	B	0.503	0.476
M 50	50	0	50	x	C	0.264	0.237
M 75	75	0	25	x	C	0.193	0.165
M 100	100	0	0	poor		0.126	0.129
I 15	0	15	85			0.726	0.671
I 25	0	25	75			0.655	0.602
I 50	0	50	50	x	C	0.496	0.457
I 88	0	87.5	12.5			0.347	0.308
I 100	0	100	0			0.303	0.279
MI 25	12.5	12.5	75	x	B	0.732	0.699
MI 25	12.5	12.5	75			0.755	0.709
MI 35	17.5	17.5	65	x	B	0.534	0.543
MI 50	25	25	50	x	C	0.354	0.332
MI 75	37.5	37.5	25	poor		0.215	0.203
MI 94	47	47	6			0.165	0.165

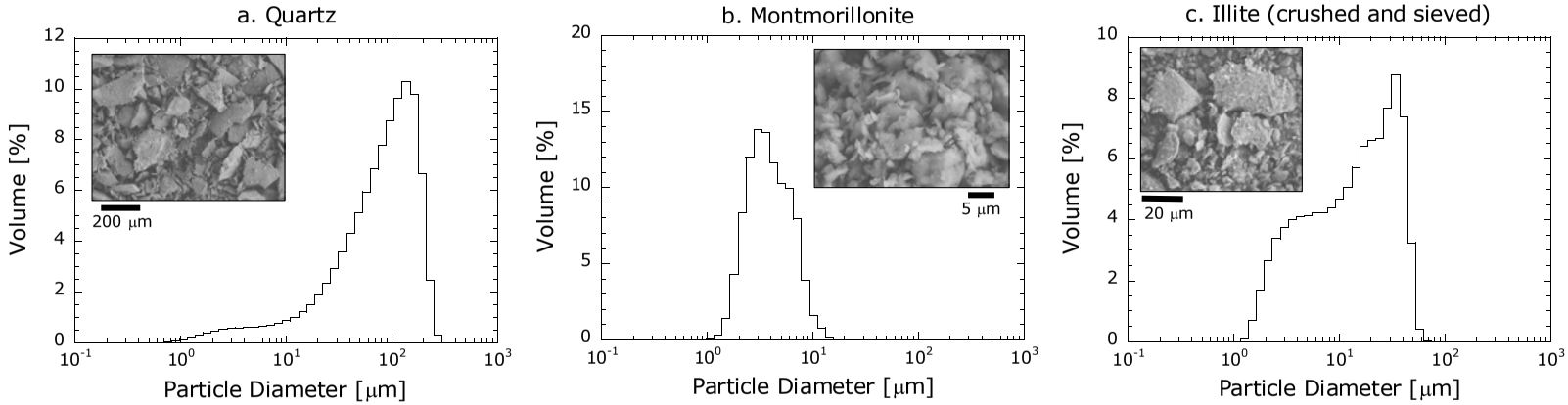

Figure 3.1. Particle size distribution for a) quartz, b) montmorillonite, and c) illite starting materials. Insets show backscattered SEM images of undeformed material.

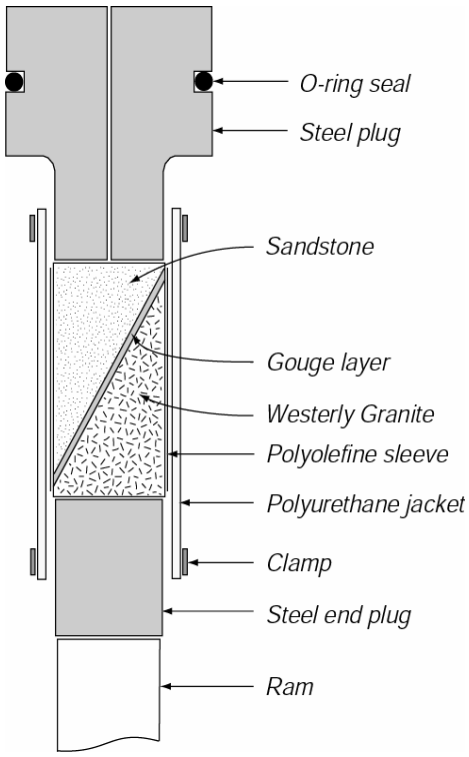

Figure 3.2. Experimental set-up for triaxial saw-cut tests.

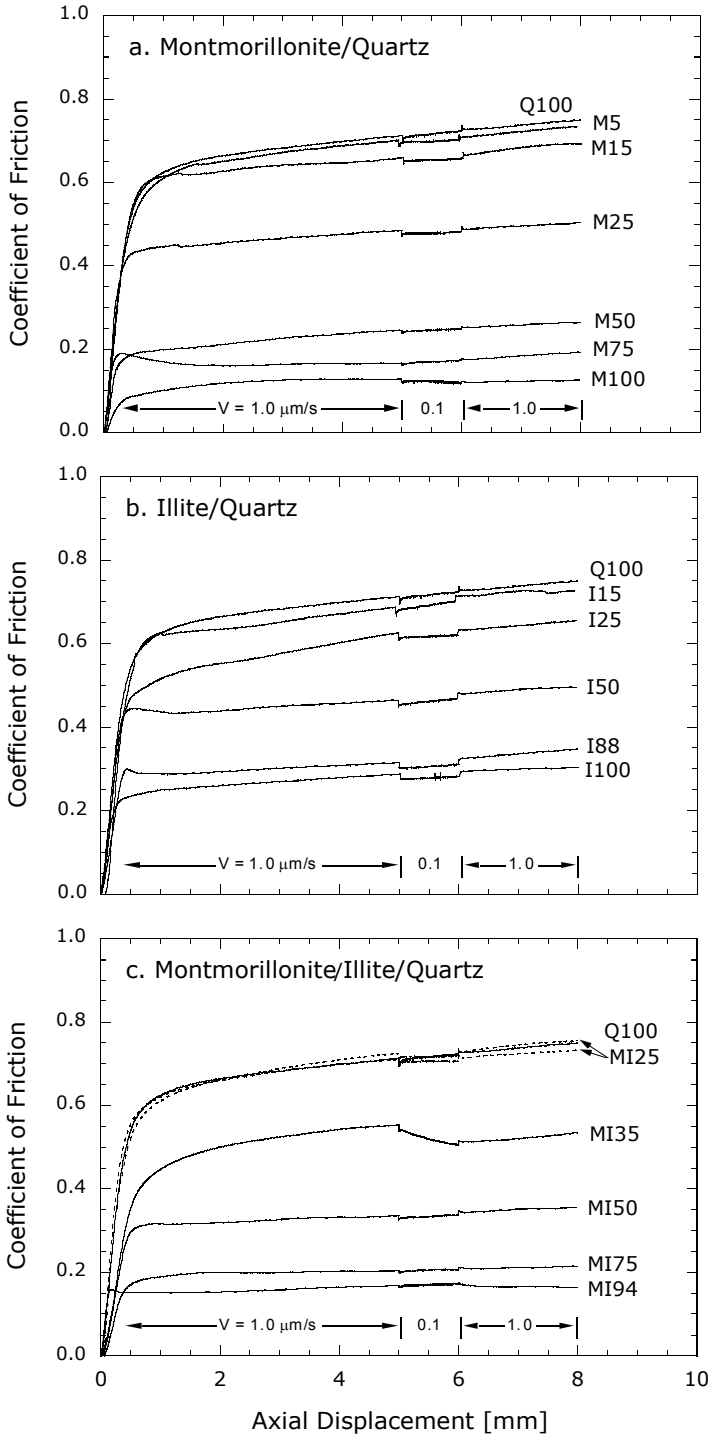

Figure 3.3. Coefficient of friction as a function of axial displacement for a) montmorillonite-quartz, b) illite/quartz and c) montmorillonite/illite/quartz mixtures.

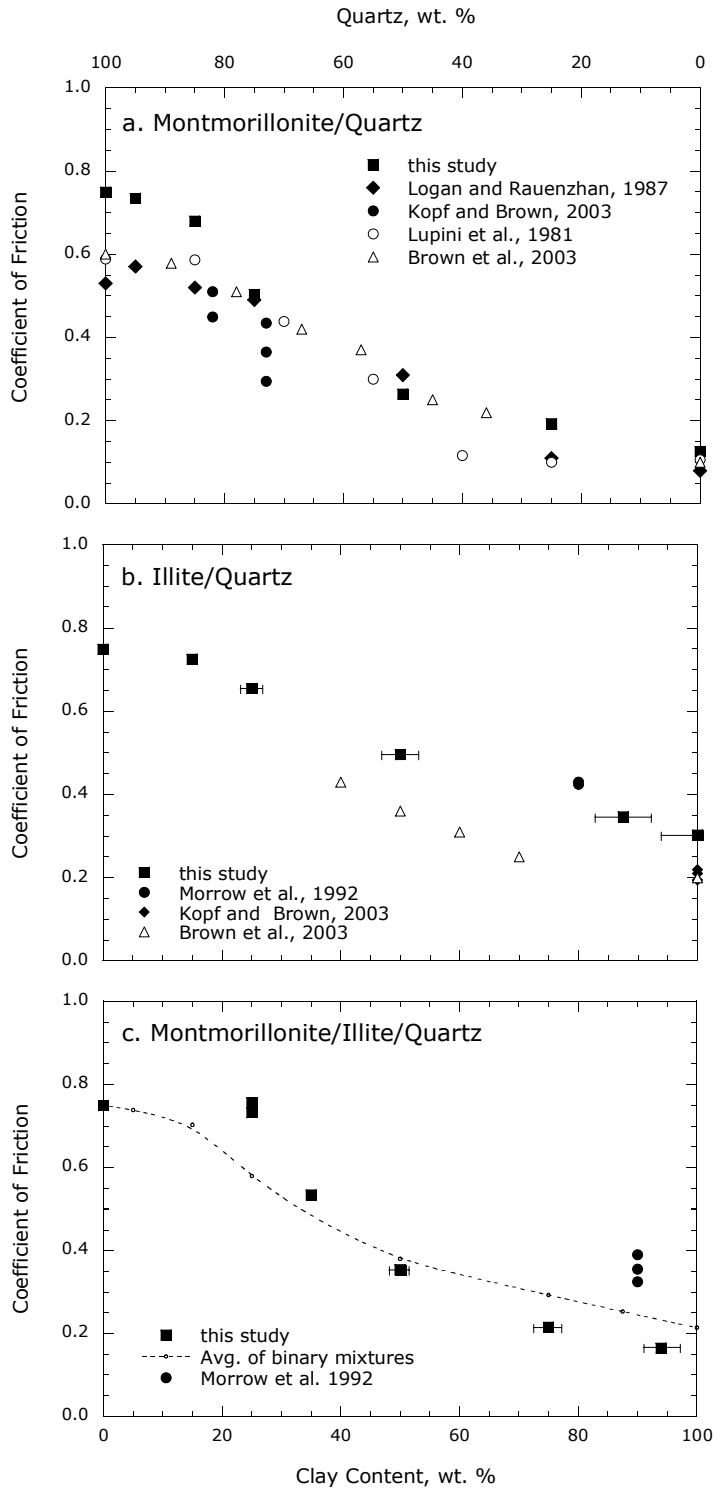

Figure 3.4. Friction coefficient of the runs shown in Figure 3 after 7.98 mm of axial displacement for a) montmorillonite/quartz, b) illite/quartz and c) montmorillonite/illite/quartz. Data from previous studies are included for comparison.

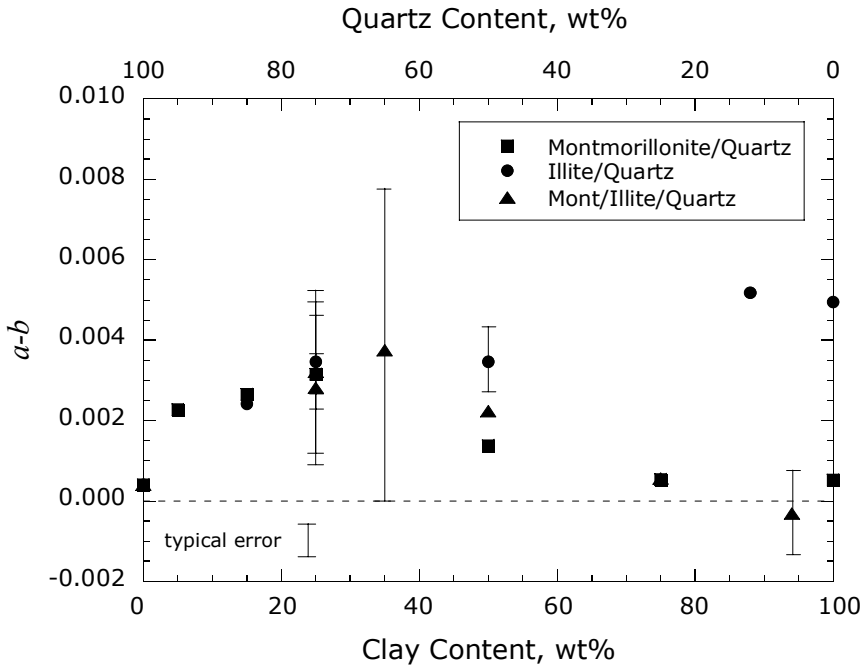

Figure 3.5. Velocity dependence of frictional sliding in clay mixtures where positive $a-b$ values indicate velocity strengthening and negative values indicate velocity weakening.

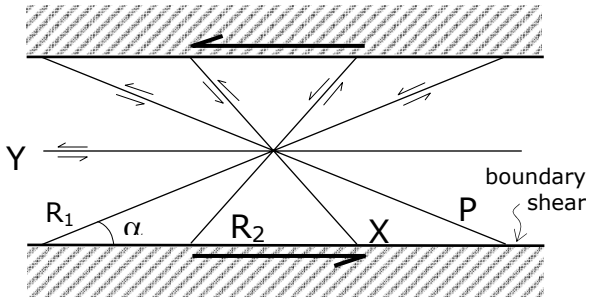

Figure 3.6. Classification of shear localization developed in deformed gouge layers (after *Logan et al*., 1992).

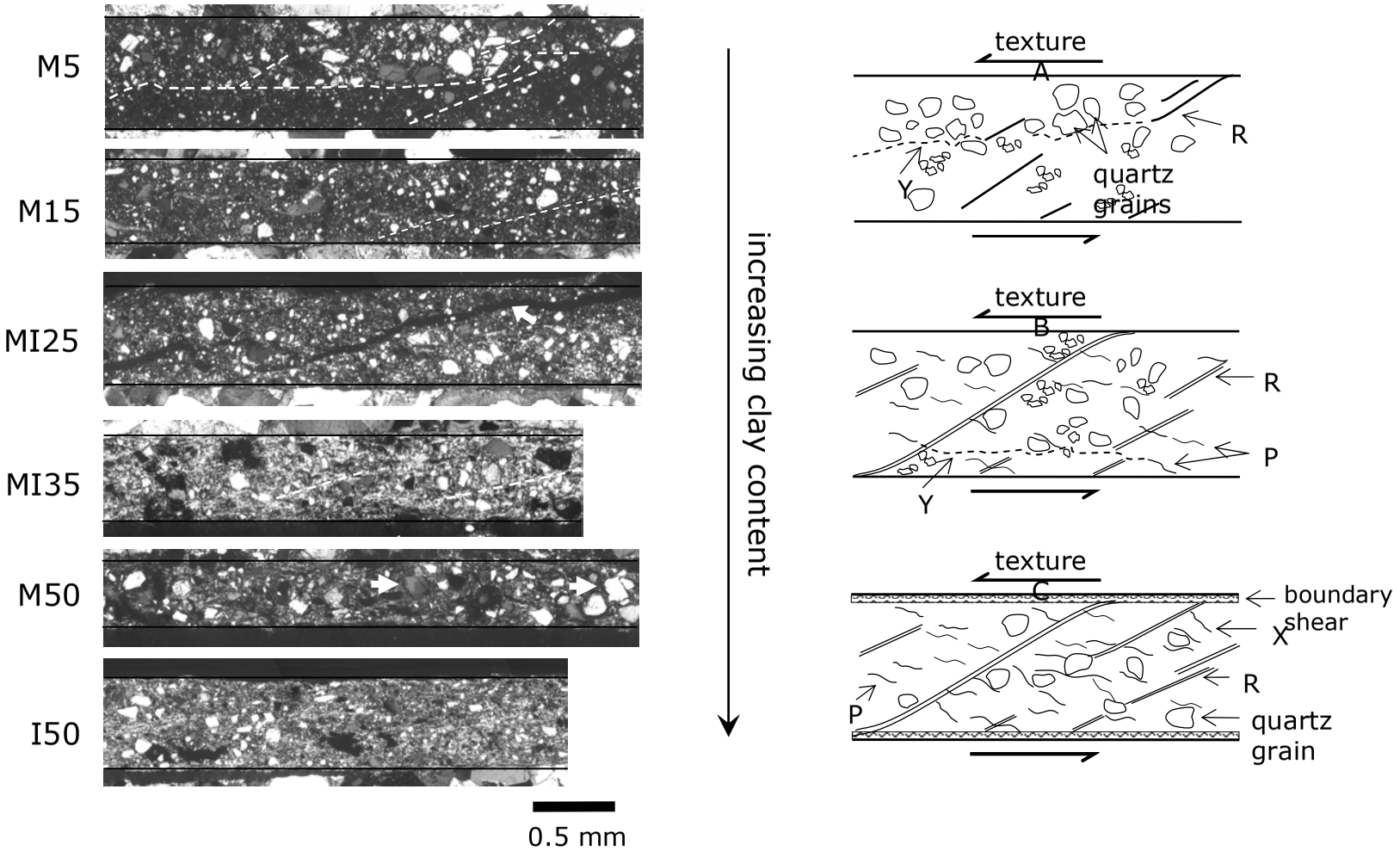

Figure 3.7. Micrographs of clay-quartz gouges under polarized light after 9.2 mm of fault parallel slip. Dashed lines highlight shear bands. The white arrow in MI25 points to an R-shear and in M50 the arrows point to large intact quartz grains. The micrographs have three classes of textures that vary with clay content.

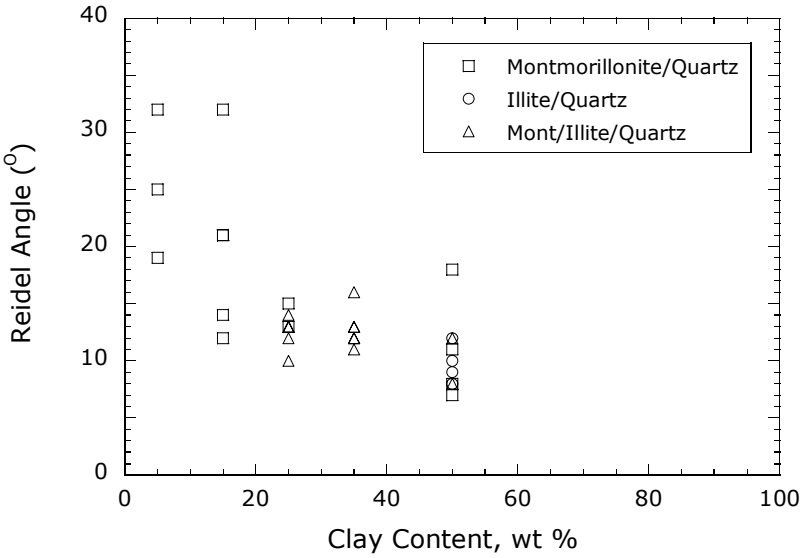

Figure 3.8. Reidel shear angle in gouge samples show a marked decrease in angle with increasing clay content at the transition from regime 1 to 2.

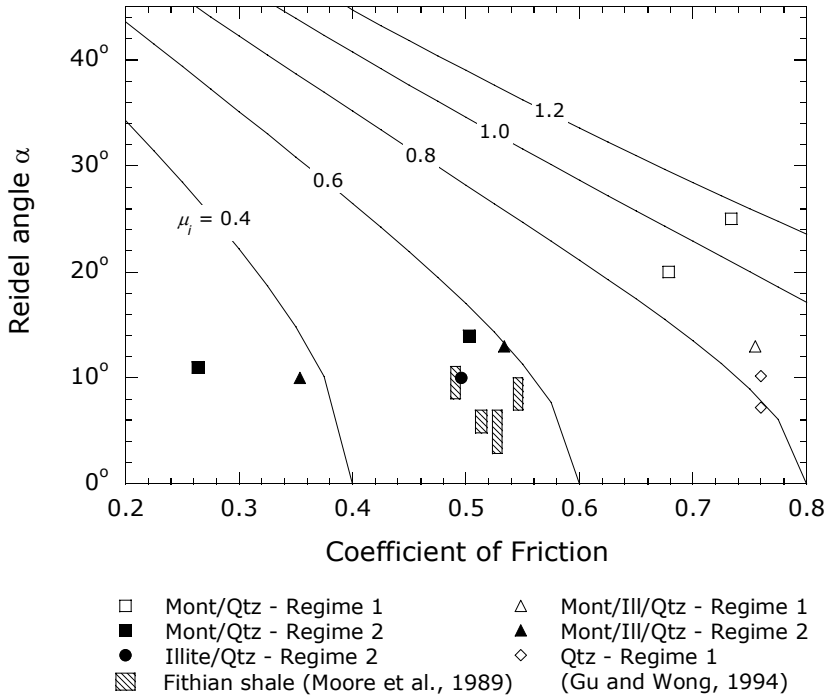

Figure 3.9. Reidel shear angle as a function of the friction coefficient. The solid curves are theoretical predictions of the Reidel shear angle as a function of the friction coefficient for fixed values of the internal friction coefficient μ_i from equation (1). The points represent the average Reidel angle from experimental data for our mixtures shown Figure. 8, from *Gu and Wong* [1994] for coarse quartz, and from *Moore et al.* [1989] for illite-bearing Fithian shale. Open and closed symbols represent samples belonging to regime 1 and 2, respectively.

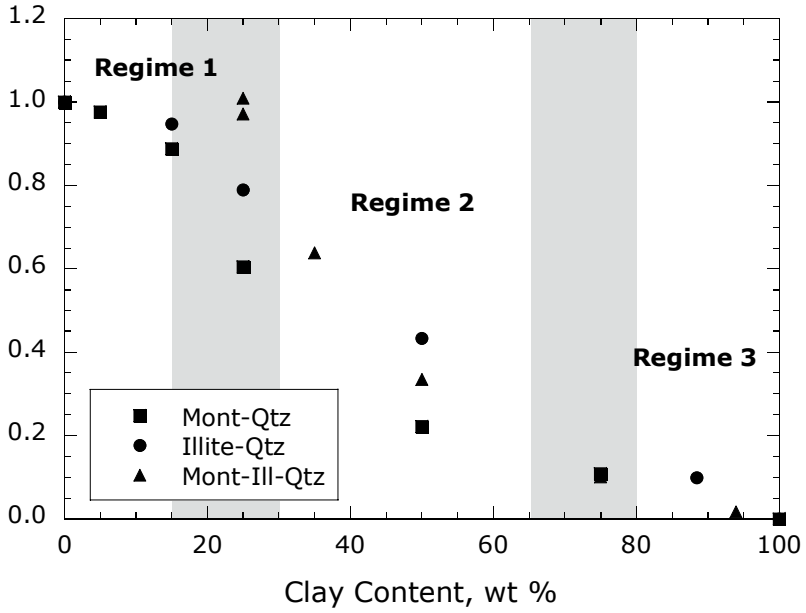

Figure 3.10. Normalized coefficient of friction as a function of clay content. The three regimes can be discerned clearly here with the transition between them indicated by the grey areas.

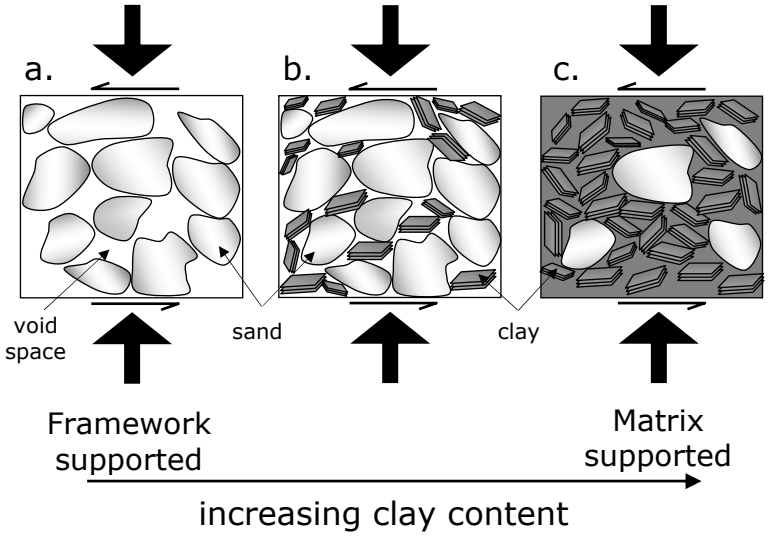

Figure 3.11. a) A stress supporting framework of quartz sand grains. b) The clay minerals collect in the void space of the coordinated grains and the load is accommodated by the quartz force chains. c) As the clay fraction increases the force chains are comprised of the weak minerals that yield easily to applied stress until finally the clay content exceeds the void volume and shear strength is reduced.

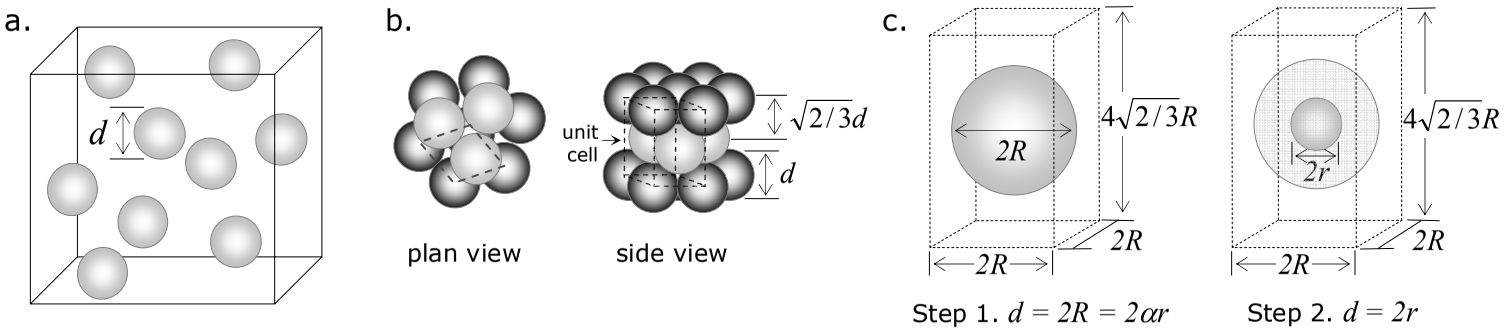

Figure 3.12. a) A system of randomly dispersed spherical particles. b) HCP particle configuration considered in our ideal packing scenario. c) A representative HCP unit cell volume containing a spherical grain embedded within a clay matrix. The system dilates by a factor α in Step 1. In Step 2 the solid grain contracts to its original size within the transformed cell and the residual space is filled with clay.

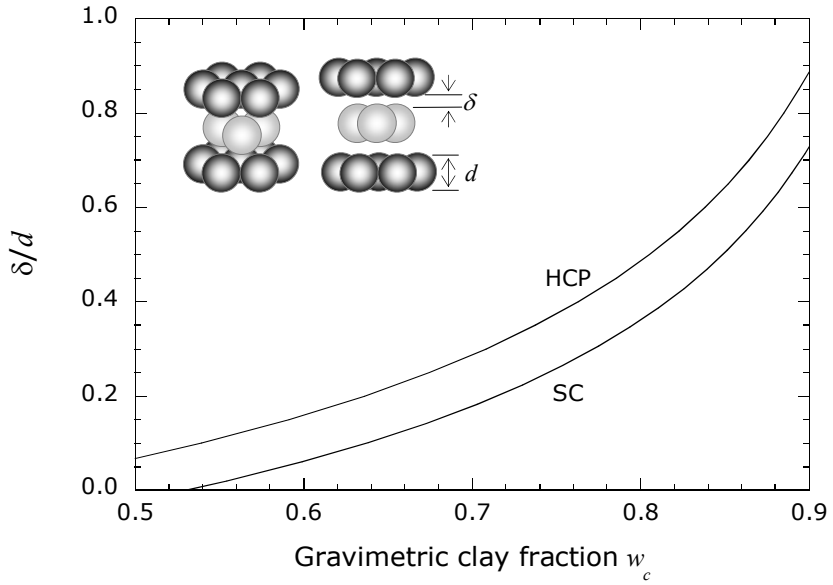

Figure 3.13. The normalized clay thickness versus the clay content for simple cubic packing and hexagonal close packing where δ is the layer spacing and d is the diameter of a spherical quartz particle.

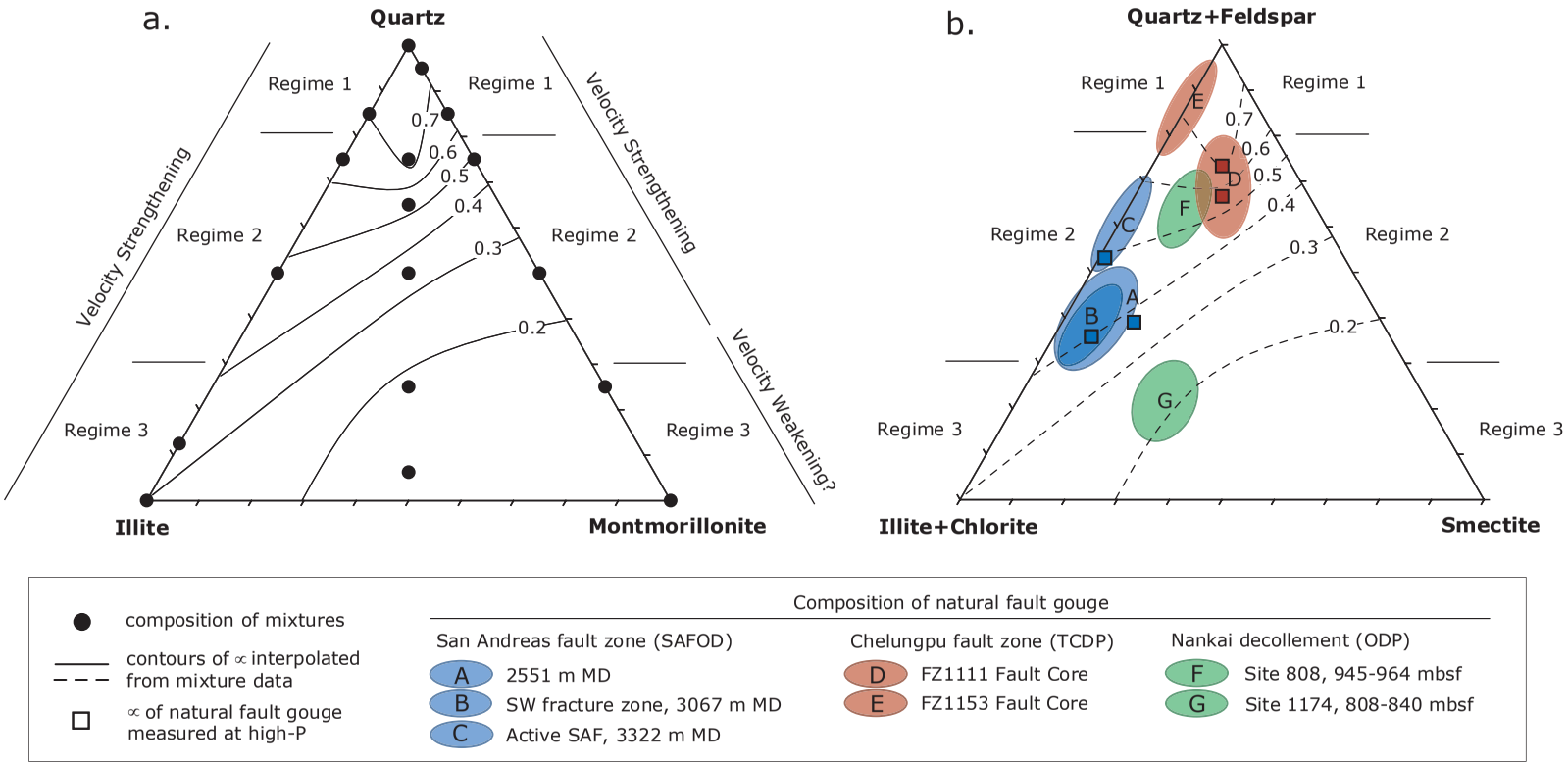

Figure 3.14. a) Compositions of simulated clay-quartz gouges are plotted as black circles. Each point is associated with a friction coefficient which then was used to construct contours. b) For comparison, we plot the compositions of natural shear zone samples (colored areas) retrieved by deep drilling projects and their measured friction coefficients (squares). SAFOD data are from *Solum et al*. [2006] and *Morrow et al*. [2007]. TCDP data are from *Kuo et al*. [2005] and D. Lockner (personal communication, 2007). ODP data for Sites 808 and 1174 are from *Underwood et al*. [1993] and *Steurer and Underwood* [2003], respectively.

Chapter 4

Frictional Strength of SAFOD Core at Seismogenic Depths: Implication for Fault Stress State and Pore Pressure in the San Andreas Fault

Abstract

Elevated pore fluid pressure confined to the fault zone has long been hypothesized as the cause of weakening in the SAF. In light of the recent findings that the SAFOD cores contain weak clay, serpentine an talc phases, we extend the *Rice* [1992] model to the case for SAF gouge with reduced frictional strength and calculate the pore pressures required to weaken the fault. Constraints on fault zone friction coefficient μ_f were obtained from published and newly acquired data from friction experiments conducted in the saw-cut configuration at hydrothermal conditions (compatible with 0-15 km depth) on three materials: illite-bearing fault gouge from SAFOD ST1 3067 m MD core at, the serpentine mineral-chrysotile, and talc. Using experimental values for μ_f and a directional constraint $\psi = 20°$ (corresponding to σ_H making a 70° angle to the fault), the fluid pressures involved for a thrust faulting regime range from sub-hydrostatic up to 3

times σ_V, less than that predicted using the original *Rice* model. To satisfy the heat flow constraint with $\bar{\tau}$ <20 MPa and assuming $\sigma_h \sim \sigma_V$ based on the inferred stresses at SAFOD, the angle ψ must be less than 5° and $\mu_f \approx 0.05$. Such values are lower than $\mu_f = 0.1 - 0.2$ typically cited because conventional analysis of the problem assumes the normal stress can be approximated by the vertical overburden. In our modified Rice [1992] model σ_V is the minimum principle stress and $\sigma_n \sim \sigma_H$, resulting in a lower friction coefficient.

1. Introduction

A multiplicity of geophysical and geological observations have indicated that the San Andreas fault (SAF) is mechanically weak. Absence of an appreciable heat flow anomaly near the fault trace constrains the absolute magnitude of the average shear stress on the SAF to be less than about 20 MPa [e.g., *Brune et al*., 1969; *Lachenbruch and Sass*, 1980; 1992]. Seismological and geological indictors constrain the maximum principal stress to be at a high angle to the strike of the SAF [e.g. *Mount and Suppe*, 1987; *Zoback et al*., 1987]. Together with related measurements of the stress magnitude, such data imply that not only is the SAF weak in an absolute sense, it is also weak when compared to the surrounding crust [*Rice*, 1992].

The stress magnitude inferred for the SAF is significantly lower than that predicted by a fault model based on the *Anderson* [1951] theory of faulting and laboratory-derived rock friction data [*Byerlee*, 1978], assuming a hydrostatic pore pressure gradient [e.g. *Brace and Kohlstedt*, 1980]. If the laboratory strength data for fault rocks is correct, then one way to reconcile lab and field observations is to appeal to elevated pore fluid pressure within the fault zone. However, necessary fluid pressures would exceed the minimum compressive stress and would hydrofrac the host rock. This

theoretical problem was overcome independently by *Byerlee* [1990] and *Rice* [1992] when they recognized that for a mature fault such as the San Andreas, a pore pressure gradient could be established between the fault core and the surrounding host rock that would never exceed the local minimum principal stress. At the same time, pore pressure in the fault core could rise as needed, reducing the effective normal stress and therefore the fault strength. An end-member conceptual model of this type is shown in Figure 1a, where the adjoining crust is considered to be relatively strong, with limiting stresses comparable to those required to induce thrust faulting in a rock mass with Byerlee frictional strength [*Brace and Kohlstedt*, 1980]. A critical assumption in this scenario is that a pronounced pore pressure excess can be generated and maintained within the fault gouge that would allow frictional sliding to occur at a low shear stress level, with a local stress state in the strike-slip regime and maximum principal stress oriented almost normal to the fault plane (Figure 1a).

In contrast, the vertical pore pressure gradient in the other end-member case (Figure 1b) is assumed to be hydrostatic. In the absence of pore pressure excess, this scenario is viable only if frictional strength of the fault gouge is intrinsically low, possibly due to the abundance of minerals such as smectite, illite, serpentinite and talc with friction coefficients significantly lower that predicted by Byerlee's law. One of the scientific objectives of SAFOD is to acquire pertinent borehole data and laboratory data on cores that would constrain the stress state and pore pressure of the SAF near Parkfield, California and potentially resolve the question to what extent they are in agreement with either of these two end-members.

The SAFOD experiment included two boreholes. After passing through 760 m of Tertiary and Quaternary sedimentary rocks, a pilot hole was drilled vertically in 2002, through Salinian granite basement to a depth of 2170 m, at a distance of 1.8 km

southwest of the surface trace of the SAF. Heat flow and stress orientation in the SAFOD pilot hole basically agree with previous regional data for the SAF. No heat flow anomaly was detected, thus constraining the average shear stress to be low [*Williams et al*., 2004]. Borehole breakout and drilling-induced tensile fractures in the pilot hole at depths below 2050 m indicate that the maximum horizontal stress is inclined at a relatively high angle of ~70^{o} to the strike of the SAF [*Hickman and Zoback*, 2004]. The main borehole (immediately adjacent to the pilot hole) was drilled during SAFOD Phase 1 (in 2004) and Phase 2 (in 2005). This hole was first drilled vertically to a depth of 1490 m, and then directionally drilled to the northeast toward the SAF, deviating from the vertical at an angle by 54^{o}-60^{o}. The main hole terminates at a total vertical depth of 3200 m, corresponding to a measured depth of ~4 km. *Boness and Zoback* [2006] inferred from observation of stress-induced seismic anisotropy in the main hole that the maximum horizontal stress basically aligns with that inferred by *Hickman and Zoback* [2004] for the deeper portion of the pilot hole.

The directionally drilled segment of the SAFOD hole penetrated over 1 km of arkosic sandstones and conglomerates, as well as numerous faults before terminating in sedimentary rocks of the Great Valley sequence. Frictional properties of drill cuttings and cores retrieved during Phases 1 and 2 were systematically investigated by *Tembe et al*. [2006], who observed that the frictional strength varies appreciably among the primary lithologic units and shear zones. Whereas the friction coefficients of quartzo-feldspathic core and cuttings are in basic agreement with Byerlee's law, those of shale, claystone and siltstone units are relatively low (in the range of 0.40-0.55). Some of the weakest samples were retrieved from two shear zones at measured depths of 2560 m and 3067 m. The active trace of the SAF was penetrated at a measured depth of 3322 m, where talc (which

has a very low friction coefficient 0.1 to 0.15) was discovered in serpentinite cuttings [*Moore and Rymer*, 2007].

It is implicitly assumed in *Rice's* [1992] conceptual model (Figure 1a) that the friction coefficient of the fault gouge is comparable to that of the country rock (thus obeying Byerlee's law). In light of the recent findings that the SAFOD cores contain hydrous platy minerals and can be weak, an objective of the present study is to extend the *Rice*-style model to apply to a fault zone with relatively low frictional strength. Explicit expressions for the stress state and pore pressure distribution will be presented. However, to connect the theoretical predictions to field observations, it is necessary to prescribe the friction coefficient of the SAF gouge as a function of depth. The measurements of *Tembe et al*. [2006] were conducted at room temperature, but frictional strengths of minerals such as illite, smectite and serpentinite found in SAFOD cores [*Solum et al*., 2006] tend to become stronger with increasing temperature [*Moore et al*., 1997; *Moore and Lockner*, 2007]. Hence the second objective of this study is to characterize the frictional properties of SAFOD cores under hydrothermal conditions comparable to those at seismogenic depths. The hydrothermal friction data allow us to determine the stress state and pore pressure distribution that are consistent with heat flow and *in situ* stress measurements.

2. Fault Stress State and Pore Pressure Distribution

2.1 Stress state in the country rock

Following *Rice* [1992] we assume the stresses in the country rock surrounding the SAF to be in the thrust faulting regime, so that the minimum and maximum principal stresses are given by the vertical stress σ_V and maximum horizontal stress σ_H ,

respectively. If the rock mass is permeated by randomly distributed fractures and the pore pressure p_o as a function of depth is given by the hydrostatic gradient, then limiting values of σ_V and σ_H (represented by the large Mohr circle on the left in Figure 2) are related by [*Brace and Kohlstedt*, 1980]:

$$\sigma_H = \sigma_V \left[\frac{\sqrt{1+\mu^2}+\mu}{\sqrt{1+\mu^2}-\mu} \right] - 2p_o \left[\frac{\mu}{\sqrt{1+\mu^2}-\mu} \right] \quad (1)$$

where μ denotes friction coefficient of the country rock (here assumed to obey Byerlee's law). Fluid and rock density values of $\rho_w = 1000$ kg/m^3 and $\rho_r = 2500$ kg/m^3 will be used to calculate the pore pressure $p_o = \rho_w gz$ and vertical overburden $\sigma_V = \rho_r gz$, respectively. Since the country rock is assumed to be in a thrust faulting regime, the minimum horizontal stress σ_h is expected to have an intermediate magnitude between σ_V and σ_H. Accordingly, σ_h can be related to σ_V and σ_H by the ratio

$$r \equiv \frac{(\sigma_H - \sigma_h)}{(\sigma_H - \sigma_V)} \quad (2)$$

which is a nonnegative number between 0 and 1. *Hickman and Zoback* [2004] inferred from observations of breakout and tensile fractures in the SAFOD pilot hole that σ_h is comparable to the vertical overburden, corresponding to a ratio of $r \sim 0.8-1$.

2.2 Stress state and pore pressure inside the fault zone

A conceptual breakthrough in *Rice's* [1992] and *Byerlee's* [1990] analyses is the clear differentiation between stress states in the country rock and within the gouge zone. Rice emphasized that the two stress tensors can be very different, and indeed even if one assumes the country rock is in the thrust faulting regime, there is still the possibility that stresses within the fault zone (represented by the gray Mohr circle in Figure 2) may actually be in the strike-slip regime, with the maximum and minimum principal stresses

given by the maximum horizontal stress (σ_H^f) and minimum horizontal stress (σ_h^f), respectively.

Notwithstanding these fundamental differences, the two stress states are constrained by mechanical equilibrium (at the interface between the country rock and gouge zone), which would necessarily require the resolved normal stress σ_n and shear stress τ to be continuous across the interface. Other stress components can, in principle, be discontinuous across the interface. If the angle between the minimum horizontal stress σ_h in the country rock and the fault strike is ψ, then the resolved stresses σ_n and τ will fall on the point so indicated on the (σ_h, σ_H) Mohr circle in Figure 2. The equilibrium condition then constrains this Mohr circle to intersect the gray Mohr circle (representing horizontal stresses inside the fault zone) at (σ_n, τ).

For the sake of simplicity, *Rice* [1992] focused his analysis on the limiting case with the fault gouge and country rock having identical frictional strength. Here we extend his analysis to the more general case, with the SAF fault gouge having a friction coefficient μ_f lower than the country rock. If the fault is critically stressed in the strike-slip regime, then the tangent with slope μ_f in Figure 2 should touch the gray Mohr circle and intersect the horizontal axis at a point corresponding to the pore pressure p_f inside the fault zone. It can be observed that not only are the stress states within and outside the fault zone very different, the pore pressure p_f inside the fault zone is also significantly higher than the hydrostatic value p_o in the country rock. Indeed, it is possible that the local pressure p_f exceeds the lithostatic pressure σ_V. However, it should also be noted that even though the local pore pressure can be very large, hydraulic fracturing does not occur since its magnitude is still less than the minimum principal stress σ_h^f inside the fault gouge zone. Analytic expressions can be derived for the pore pressure and stresses

inside the fault zone. The mathematical details are described in Appendix A, and here we only present the pertinent results.

The resolved shear and normal stresses are given by

$$\tau = \frac{r\,\mu \sin 2\psi}{\sqrt{1+\mu^2}-\mu}\,(\sigma_V - p_o) \tag{3}$$

$$\sigma_n = p_o + \left[\frac{\sqrt{1+\mu^2}+\mu - r\,\mu \sin^2\psi}{\sqrt{1+\mu^2}-\mu}\right](\sigma_V - p_o) \tag{4}$$

Since the overburden σ_V and hydrostatic pore pressure p_f both increase linearly with depth *z*, the resolved shear and normal stresses would also increase linearly with depth for fixed friction coefficient μ and angle ψ. It should be noted that the shear stress is directly proportional to *r,* and therefore arbitrarily low shear stresses can be attained for *r* very small. Expressions for the maximum and minimum horizontal stresses are given in Appendix A. Here we focus on the pore pressure inside the fault zone, which is given by

$$p_f = p_o + \left[\frac{\sqrt{1+\mu^2}+\mu - r\,\mu(\sin^2\psi + \sin 2\psi/\mu_f)}{\sqrt{1+\mu^2}-\mu}\right](\sigma_V - p_o) \tag{5a}$$

The local pore pressure excess (given by the second term above) derives from the trade-off between the angle ψ and friction coefficient μ_f. The local pore pressure increases linearly with depth only if the gouge friction coefficient is independent of temperature and effective normal stress.

We plot in Figure 3 the Hubbert-Rubey coefficient $\lambda = p_f/\sigma_V$ as a function of the angle ψ for friction coefficient μ_f ranging from 0.1 to 0.6. It can be seen that while

the pore pressure excess increases with increasing frictional strength, it decreases almost linearly with increasing angle. As elaborated in Appendix A, if the angle ψ is small (< 20^o or so), the term containing $\sin^2\psi$ in (5a) can be neglected and $\sin 2\psi$ can be approximated by 2ψ. Accordingly, the local pore pressure can be approximated by

$$p_f \approx p_o + \left[\frac{\sqrt{1+\mu^2}+\mu-2\mu(r\,\psi/\mu_f)}{\sqrt{1+\mu^2}-\mu}\right](\sigma_V - p_o) \tag{5b}$$

and therefore the Hubbert-Rubey coefficient is simply

$$\lambda = \frac{p_f}{\sigma_V} \approx \frac{\rho_w}{\rho_r} + A - B\left(\frac{r\,\psi}{\mu_f}\right) \tag{6a}$$

with
$$A = \left[\frac{\sqrt{1+\mu^2}+\mu}{\sqrt{1+\mu^2}-\mu}\right]\left(1-\frac{\rho_w}{\rho_r}\right) \tag{6b}$$

and
$$B = \left[\frac{2\,\mu}{(\sqrt{1+\mu^2}-\mu)}\right]\left(1-\frac{\rho_w}{\rho_r}\right) \tag{6c}$$

The pore pressure excess decreases linearly with increasing $r\,\psi/\mu_f$, a parameter which characterizes the interplay of the fault stress state (in the numerator) and frictional strength (in the denominator). Assuming $\rho_w = 1000$ kgm^{-3}, $\rho_r = 2500$ kgm^{-3} and friction coefficient $\mu = 0.6$-0.85, the parameters *A* and *B* fall in the ranges of 1.87-2.81 and 1.27-2.21, respectively.

To better characterize the frictional strength of the SAF gouge as a function of depth, we conducted a suite of hydrothermal experiments to investigate the frictional properties of a SAFOD core. The new data with other published data will be synthesized

and input into this model to infer the stress state and pore pressure distribution that are compatible with the stress orientation and heat flow measurements at SAFOD.

3. Hydrothermal Data on Frictional Strength of SAFOD Core

3.1 Description of material

Tembe et al. [2006] have conducted a comprehensive investigation of the room temperature frictional strength of cuttings and spot core samples retrieved during SAFOD Phases 1 and 2. They identified the weakest material to be from an illitic clay layer (Figure 4a) approximately 30 cm thick in the spot core at measured depth (MD) of 3067 m. The black-colored gouge (cut from 7-9 cm from the top of the core) had a friction coefficient of 0.40-0.45 at room temperature (Figure 4b). The shear zone is thought to be a minor inactive strand ~130 m southwest of the active SAF [*Hickman et al*., 2005]. X-ray diffraction analysis (XRD) of *Solum et al*., [2006] determined composition of this gouge to be 48-51 weight % illite, 14-18% mixed illite-smectite, 19-22% feldspar, 11-17% quartz, 1% chlorite, and trace amounts of calcite. The mineralogy and texture were further studied by *Schleicher et al.* [2006] using electron microscopy (SEM, TEM) and XRD. They reported the presence of a natural, swelling smectite phase in the spot core from 3067 m MD, and interpreted the slickenfiber geometries and related texture of this authigenic phase as mineral coatings on microfault surfaces associated with some increments of slip. Laboratory data have shown that the presence of smectite and illite in a gouge mixture can significantly lower the frictional strength [e.g. *Tembe et al*., 2007]. However, most of the data were acquired at room temperature, and to our knowledge, there has not been any systematic investigation of the frictional properties of such gouge

mixture under hydrothermal conditions. Our experiments were conducted as a first step in characterizing the temperature dependence of natural fault gouge strength.

3.2 Experimental methodology

The SAFOD 3067 m MD gouge was highly friable and contained many fractures incurred from previous tectonic episodes and during the coring process. Our best efforts to obtain intact specimens for mechanical testing were largely unsuccessful and it was ultimately decided to crush the material and test it as a simulated gouge. The powdered material was passed through a 100 mesh sieve to obtain particle sizes of <149 μm for experimental use. In the laboratory a geologic fault zone, consisting of a principal slip zone embedded in country rock, is represented by a thin gouge layer deformed between forcing blocks. Our high-temperature frictional sliding experiments were conducted in the conventional triaxial configuration on a 1 mm-thick gouge layer sandwiched between Westerly granite forcing blocks. The forcing blocks were made from a single cylindrical sample of Westerly granite (1.91 cm in diameter and 4.06 cm in length) which was cut in half at a 30° incline (Figure 5). Although maximum displacement of the driving blocks is limited by the size of the pressure vessel, the triaxial apparatus allows for ambient pressures and displacement rates that are comparable to the tectonic stresses and creep rate of the SAF.

The simulated gouge layer was first prepared as a thick paste with deionized water, which was spread onto the saw-cut face of the upper forcing block, and then sandwiched by the lower block. The saw-cut surfaces were roughened slightly with SiC powder to ensure coupling of the gouge layer and forcing block. To assure good pore pressure communication between the gouge layer and the external pore pressure system, the upper driving block contained a small hole drilled along the sample axis. The hole

was then packed with medium-sized Ottawa sand to minimize extrusion of the gouge and allow the flow of fluids. The low porosity (< 1%) of the lower granite driving block minimizes water storage and pore pressure transients that might be generated during rapid stress changes. Following the experimental procedure of *Moore et al*. [2004], the assembled saw-cut sample was inserted into an annealed copper jacket between titanium carbide and Lucalox ceramic spacers, and then slipped into a platinum resistance furnace. The space between the copper jacket and furnace was loosely packed with thermally conductive boron nitride and then the entire assembly was placed in the pressure vessel.

Confining pressure (argon gas medium) was applied first while the sample assembly and pore pressure lines were evacuated for 25 minutes. Deionized water was then introduced as the pore fluid and the sample allowed to equilibrate at pore pressure $p_f = 100$ MPa and confining pressure of 138-400 MPa. The confining pressure and pore pressure were computer controlled to within ±0.3 MPa and ±0.2 MPa, respectively.

We assumed temperature was relatively well correlated with depth and chose run temperatures appropriate for 3-15 km depth. Based on heat flow for Central California (described in Appendix B), the corresponding run temperatures were 96-431°C. Following the addition of the pore pressure, the temperature was raised gradually at a rate of approximately 5°C/min to the desired run value and the sample was allowed to equilibrate for 1 hour.

Triaxial loading was then applied to the saw-cut sample such that the saturated gouge layer would be sheared under drained conditions (no internal rise in p_f within the gouge layer) at a fixed normal stress σ_n and constant pore pressure p_f = 100 MPa. Up to 3.5 mm of axial displacement (corresponding to 4.04 mm resolved on the inclined saw-cut) would be reached in the experiments. A total of 12 experiments were performed at effective normal stresses $\sigma_n - p_f$ of 38 - 300 MPa and are summarized in Table 1. In

each run a servo-controlled axial displacement rate of 0.5 μm/s was initially applied until an axial displacement of 1.5 mm had been attained. To measure the velocity dependent response the displacement rate was then alternated between 0.05 μm/s and 0.5 μm/s until the end of the run or until the jacket ruptured. Experimental displacement rates parallel to the saw-cut correspond to 18.5 and 185 mm/yr, compared with SAF creep rates of 28-34 mm/yr [*Titus et al*, 2006].

The mechanical data were corrected for the elastic deformation of the loading system, jacket strength (details reported in *Moore et al*., 1996), reduction in contact area between the sliding blocks during deformation, and confining pressure-dependent piston-seal friction, producing frictional strength values that are accurate to within 10%. Changes in frictional strength during a single experiment, such as that due to displacement rates steps, will be more accurate since the measurements were made in the same run.

Six deformed samples (runs 1, 2, 3, 4, 6, and 7) were impregnated with epoxy and then sawed along a plane parallel to the sample axis and perpendicular to the saw-cut plane and prepared as thin-sections for standard petrographic analysis. Transmission optical microscopy under polarized light and scanning electron microscopy (SEM) were used to image the gouge layer. Electron dispersive X-ray analysis and thermogravimetric/ differential thermal analyses (TGA/DTA) were also conducted on the starting material.

3.3 Mechanical data and effect of temperature

The frictional strength data are normalized by the effective normal stress and are presented in Figure 6 in terms of the coefficient of friction of the gouge $\mu_f = \tau/(\sigma_n - p_f)$, where τ is the shear stress resolved on the saw-cut surface. For each sample the friction coefficient values attained at an axial displacement of 3.2 mm

(corresponding to shear displacement of 3.7 mm resolved on the saw-cut) are compiled in Table 1.

Several features were observed in the frictional sliding data. First, the friction coefficient typically attained a relatively stable value at an axial displacement around 1 mm, beyond which strain hardening manifested by a slight increase in friction coefficient with axial displacement. It is important to consider that when slip in the experiments is limited to a few millimeters, the values of friction and velocity dependence may not represent a true steady state, but reflect and evolving system. This may be apparent in the mechanical data as a strain-hardening/softening trend due to ongoing cataclasis, compaction, and strain localization within the gouge layer as well as time-dependent fluid-rock interactions if the gouge is chemically out of equilibrium. In our experiments the effect was most pronounced at high temperatures. For runs that terminated early the friction coefficient values reported in Table 1 were extrapolated to 3.2 mm by assuming a linear strain hardening trend for an axial displacement rate of 0.5 μm/s.

Second, while experiments conducted at the same temperature demonstrate a pressure dependence, the temperature dependence is far greater with values ranging from 0.4 at 96 °C, comparable to the room-temperature findings (Figure 4), up to 0.73 at 431 °C. Similar dependence has been observed in heated chrysotile [*Moore et al*., 2004]. Third, each velocity step was associated with a transient perturbation in the friction coefficient in the same sense as the velocity step. Stick-slip behavior accompanied velocity step changes in the run at 300 MPa (Figure 6c) and oscillatory behavior was observed at 283 °C (Figure 6b) and at 150 MPa (Figure 6c). Smaller amplitude-high frequency noise in the mechanical data are due to <3 °C fluctuations in the temperature.

Steady-state frictional sliding can be characterized by the quantity $d\mu_{ss} / d\ln V$, where μ_{ss} denotes the steady state coefficient of friction at the slip velocity V. In the

context of the rate and state dependent friction model [*Dieterich,* 1979], this quantity is given by the difference *a*-*b*, with *a* and *b* characterizing the "direct" and "evolution" effects in response to perturbations in slip velocity [*Paterson and Wong*, 2005]. Positive and negative values of $a - b = d\mu_{ss} / d \ln V$ thus correspond to velocity strengthening and weakening, respectively. The experimental data naturally fall into three thermo-mechanical regimes: low-temperature (T<266°C) with velocity strengthening behavior, intermediate-temperature (266°C≤T≤283°C) with velocity weakening behavior, and high-temperature with predominantly velocity strengthening.

In each experiment we made several changes in the loading velocity (Figure 6) and the velocity dependence was then quantified from the corresponding changes in friction coefficient. We present in Figure 7 our data for the velocity dependence of the friction coefficient over temperature and depth. The uncertainty in these estimates is typically around ±0.0004. Values for *a*-*b* range from -0.0056 up to 0.0122 with negative values occurring in the intermediate regime and positive values in the low and high temperature regimes. The most interesting of these is the intermediate regime, which covers a temperature range corresponding to 9.0-9.6 km depth and exhibits transient frictional behavior relevant to seismogenesis.

4. Laboratory Constraints on Stress State and Pore Pressure Associated with Near Fault Normal Compression

Seismological and geological indictors constrain the maximum horizontal stress to be subperpendicular to the strike of the SAF [e.g. *Mount and Suppe*, 1987; *Zoback et al*., 1987], with the implication that the angle ψ is small (Figure 2). Borehole breakout and drilling-induced tensile fractures in the SAFOD pilot hole [*Hickman and Zoback*, 2004] as well as stress-induced seismic anisotropy in the main hole (*Boness and Zoback*,

2006) indicate an average value of ~20° for this angle. Guided by these observations we will assume in most of our calculations a value of $\psi = 20^{o}$.

As illustrated in Figure 3, for a fixed angle ψ between the minimum horizontal stress and fault plane the pore pressure excess is predicted to decrease with decreasing friction coefficient. Using the relatively weak black gouge retrieved from 3067 m MD as a proxy for the SAF gouge, our predictions of pore pressure excess can be considered as a lower bound on what is compatible with the stress orientation data. The black gouge is thought to be in a shear zone that represents a minor inactive strand ~130 m southwest of the active SAF [*Hickman et al*., 2005]. The active trace of the SAF was penetrated at a 3322 m MD, where serpentinite cuttings were retrieved and talc discovered [*Moore and Rymer*, 2007]. For comparison, we also evaluated the stresses and pore pressure using laboratory data on serpentinite and talc [*Moore et al*. 1997; *Moore et al*., 2004; *Moore and Lockner*, 2007].

4.1 Friction coefficient as a function depth constrained by laboratory data

Equations (3) and (4) were used to evaluate the shear stress and normal stress inside the fault zone. For most of our calculations we fixed $\psi = 20^{o}$, μ=0.85, $\rho_w = 1000$ kg/m^3 and $\rho_r = 2500$ kg/m^3. The stress state in the country rock is characterized by the parameter *r*. To analyze its influence we will show calculations *r* = 0 ($\sigma_h = \sigma_H$), 0.5, and 1 ($\sigma_h = \sigma_V$).

To evaluate the pore pressure inside the fault zone using (5a), we must specify the gouge friction coefficient μ_f as a function of depth, on the basis of laboratory data as functions of temperature and effective normal stress (Figure 8). Our approach is to first define the temperature as a function of depth with a geotherm that is considered to be appropriate for the SAF near Parkfield. As detailed in Appendix B, the geotherm (B1) we

used was originally proposed by *Lachenbruch and Sass* [1977], with parameters constrained by SAF heat flow data of *Sass et al*. [1977], *Williams et al*. [2004] and *Williams* [1996]. The temperature variation as a function of depth is approximately linear with a gradient of ~28^{o}C/km.

The pore pressure was evaluated at depths corresponding to the temperatures at which the friction data were acquired (Table 1). However, the gouge friction coefficient μ_f at a given temperature is not constant, showing a slight increase with effective normal stress following an approximately linear trend. We account for this dependence and simultaneously solve for $\sigma_n - p_f$ and μ_f by the approach illustrated in Figure 7a. Once we have specified the depth *z* and stress ratio *r*, equations (4) and (5a) can be used to calculate $\sigma_n - p_f$ as a function of μ_f. As can be seen from (A10), $\sigma_n - p_f$ is approximately proportional to $1/\mu_f$. Intersection of the theoretical curve and the linearly interpolated friction coefficient data marks the point that represents the effective normal stress and friction coefficient compatible with laboratory data. Friction coefficients so inferred for the SAFOD black gouge are plotted as a function of depth for three different values of *r* in Figure 9b. It should be noted that in cases where only one measurement of friction coefficient was made at a given temperature, we have assumed that its dependence on the effective normal stress can be neglected.

Figure 10a shows the shear and normal stresses according to (3) and (4). These stresses are independent of the gouge properties, and they both increase linearly with depth. For comparison we also include the two lines corresponding to lithostatic and hydrostatic gradients. The shear stress is directly proportional to *r*, and the maximum magnitude is attained if $\sigma_h = \sigma_V$ ($r = 1$). In contrast, the normal stress is basically independent of the stress ratio and as noted in Appendix A, it can simply be approximately by the maximum horizontal stress σ_H as given by equation (A9).

4.2 Predictions for pore pressure excess in an illite-rich fault zone

Figure 10b shows the pore pressure (normalized by the overburden stress) for the illite-rich gouge from SAFOD 3067 m MD, calculated in conjunction with the friction coefficient values in Figure 9b. Several features of the pore pressure distribution should be noted. First, the pore pressure excess is predicted to be less than the scenario originally considered by *Rice* [1992], with $\mu = \mu_f$. Since frictional strength of the gouge is weaker than the country rock, a lower pore pressure excess is involved for failure along a fault zone under near fault normal compression. Nevertheless, the pore pressure required is still very high, well in excess of the lithostatic pressure. Second, because friction coefficient of the illite-rich gouge increases appreciably with temperature, the predicted pore pressure also increases with depth. Third, the pore pressure excess is sensitively dependent on *r*, and the minimum pressure is required for $\sigma_h = \sigma_V$ ($r = 1$).

Figure 10c shows the effective normal stress as a function of depth (and temperature). For comparison we also show the effective normal stress and temperature at which our experiments were conducted. From equation (A10) the effective stress is approximately proportional to r and inversely proportional to $\mu = \mu_f$. Accordingly effective normal stress is predicted to decrease with depth in the 8 to 10 km range because the gouge friction coefficient increases rapidly with temperature.

4.3 Predictions for fluid pressures in chrysotile and talc dominated fault zones

Characterization of the serpentinite discovered in SAFOD drill cuttings by *Moore and Rymer* [2007] showed the presence of the low-temperature serpentine phases, chrysotile and lizardite. Talc was found to coat vein walls, fill cracks, and form along foliation in sheared serpentinite. Room temperature friction experiments on sheared serpentinite grains plucked from bulk cuttings [*Morrow et al*., 2007] determined

coefficients of 0.4-0.45 at 40 MPa effective normal stress. Laboratory studies on the velocity dependence of chrysotile show sensitivity to temperature and displacement rate [*Moore et al*. 1997; *Moore et al*., 2004]. Given the significance of these minerals in the mechanics of the San Andreas, we will model the pore pressure distribution for chrysotile and talc. In the interest of brevity we are not including lizardite in our analysis since its coefficient of friction (0.42-0.52 over 25°-200 °C) is similar to the black gouge and would produce excess fault zone pore pressure of similar magnitude.

Frictional data obtained in the saw-cut geometry for chrysotile were reported by *Moore et al.* [1997] and *Moore et al*. [2004] for effective normal stresses between 40 to 200 MPa and temperatures 25°-280°C (0.5-9.6 km). Chrysotile has a distinct hydrophilic quality due to a relatively large specific surface area and a unique tubular structure that exposes an $(OH)^{-}$ layer on the surface [*Moore et al*., 2004]. Thus, water-saturated chrysotile at low pressure and temperature has a friction coefficient of 0.15 that gradually reaches 0.55 as adsorbed water is driven-off with increasing pressure and temperature.

Figure 11a compiles the chrysotile friction data of *Moore et al.* [1997; 2004] obtained at room temperature, 100°C and 200°C for several effective normal stresses. We used the linear interpolation approach illustrated in Figure 9a to simultaneously solve for the effective normal stress and friction coefficient at each of these three temperatures. The predicted frictional coefficient as a function of depth for r=0, 0.5 and 1 are shown by the solid lines in Figure 11a. The frictional strength of chrysotile is appreciably lower than the SAFOD black gouge (Figure 9b), and consequently lower pore pressures are involved for failure under near fault normal compression. Indeed, for very small values of μ_f and ψ a formal application of the model would require negative pore pressure (Figure 3), which is not physically realistic. We also show in Figure 10c the effective

normal stress as a function of depth, and for comparison the effective normal stress and temperature at which the experimental data were acquired.

Talc is typically found in mineral assembles containing serpentine and brucite and it considered to replace serpentine by reaction with silica. It is thought to form in the mantle wedge above a subducting slab as silica-rich fluids migrate upwards causing serpentinization of the overlying rock. Unlike the hydrous clays (i.e. smectite) and the serpentine minerals, talc remains weak well into the brittle crust (<15-20 km). Frictional strength data for water-saturated talc obtained in the same manner and apparatus used for the SAFOD ST1 3067 m MD gouge, were reported by *Moore and Lockner* [2007]. Dry talc friction coefficients were ~0.2-0.35, in comparison with wet runs that remained around 0.15-0.2. Velocity strengthening was observed at all the conditions tested.

Figure 12a compiles the talc friction data of *Moore and Lockner* [2007] obtained at room temperature, 100^{o}C, 200^{o}C, 300^{o}C and 400^{o}C for several effective normal stresses. Since the friction coefficient is very low, it can be seen from (A10) that high pore pressures are not necessary for fault zone yielding and effective normal stress increases to hundreds of MPa. Since the effective normal stresses in the laboratory tests were lower, the interpolation scheme (Figure 9a) cannot be applied here. In our calculations we simply used the mean value of the friction coefficients measured at a given temperature, thus neglecting the very small dependence on effective normal stress. Figure 12b presents the pore pressure distribution and Figure 10c the effective normal stress over depth. Because of the extremely low strength of talc, the pore pressures required are quite low but the effective normal stress can be up to ~ 1 GPa at 13 km.

5. Discussion

5.1 Fault normal compression, frictional strength and pore pressure excess

Rice [1992] proposed a model whereby frictional failure in a nominally strong fault may occur under near fault normal compression in the presence of pore pressure excess. Motivated by observations from SAFOD that the gouge may contain clay minerals such as illite and smectite (which lower the friction coefficient to 0.4 or less) and trace amount of talc (with friction coefficient down to 0.1), we extend the model to consider a scenario with a lower friction coefficient in the fault zone. We have also conducted high temperature experiments on one of the weakest gouge samples retrieved from SAFOD Phase 1 and 2 drilling to determine frictional properties pertinent to seismogenic depths. To our knowledge this is the first experimental study of the frictional properties of a clay-rich gouge under hydrothermal conditions.

Our modeling using the hydrothermal friction data of the SAFOD black gouge from 3067 m MD predicts a pore pressure that is less than that in the scenario originally considered by *Rice* [1992]. Since the gouge is weaker than the country rock, a lower pore pressure excess is required for failure to occur along a fault zone under near fault normal compression. Nevertheless, the pore pressure required is still high, well in excess of the lithostatic pressure (Figure 10). Because the friction coefficient of the illite-rich gouge increases appreciably with temperature, the predicted pore pressure also increases with depth. This prediction is in apparent discrepancy with borehole observations at SAFOD, which have yet to detect such pressure excesses [*S. Hickman*, *personal communication*, 2007].

If further measurements at SAFOD confirm the absence of pore pressure excess, an important question that must be addressed is what frictional strength and stress state can be compatible with near fault normal compression and hydrostatic pore pressure. For

the fault architecture and stress states considered here, the pore pressure distribution depends on the stress state and orientation, as well as gouge friction coefficient (Figure 3). For near fault normal compression, we can use the approximate relation (6) which implies the pore pressure inside the fault zone is nearly hydrostatic only if the ratio $r\psi / \mu_f \approx A/B$, or explicitly

$$\frac{r\psi}{\mu_f} \approx \frac{\sqrt{1+\mu^2}+\mu}{2\mu} \tag{7}$$

which equals 1.27-1.47 for $\mu = 0.85$-0.6. In our calculations $\psi = 20^o$=0.35 radians, and this condition requires the gouge friction coefficient μ_f <0.28. As illustrated by our calculations using friction coefficients of talc and chrysotile (Figures 11 and 12), relatively low pore pressure can be attained if the gouge has an abundance of such minerals.

While our analysis underscores that the model predictions on both shear stress and pore pressure are very sensitive to the stress state (as parameterized by *r*), unfortunately very limited SAFOD data are available to constrain this key mechanical attribute. Estimates of stress magnitude are available for the pilot hole, and as noted by *Hickman and Zoback* [2004] significant uncertainty is associated with these stress values primarily inferred from dimensions of borehole breakouts. In the main hole, systematic characterization of the stress orientation was conducted by *Boness and Zoback* [2006] on the basis of stress-induced seismic anisotropy, a technique which is not applicable to some of the more shaly and clay-rich sections.

Notwithstanding the apparent absence of pore pressure excess, detailed analyses of mineral assemblages in SAFOD show pervasive mineralization indicative of significant paleofluid activity [*Solum et al*., 2006; *Schleicher et al.,* 2006; *Solum et al*., 2007]. From their noble gas analyses of SAFOD mud gas samples, *Wiersberg and Erzinger* [2007] suggested that the SAF provides a path for fluid flux from greater depths,

but higher amounts of mantle-derived fluids rise up through other, more permeable faults, situated on the North American Plate side of the SAF Zone. Such a scenario would involve significant spatial complexity in both the fluid flow and stress field, which is not fully captured in *Rice's* [1992] model or in the extended version considered here. A comprehensive characterization of pertinent hydraulic and poromechanical properties of SAFOD cores will also be necessary to help constrain such processes.

5.2 Heat flow constraint on stress state

It is assumed in the use of *Rice's* [1992] model that near fault normal compression is associated with a shear stress level compatible with the heat flow constraint. Our analysis demonstrates that average shear stresses down to the 10-20 MPa level inferred from heat flow measurements [e.g. *Lachenbruch and Sass*, 1992; *Williams et al*., 2004] can be attained only if the stress ratio r is relatively small ($\sigma_h \sim \sigma_H$), but it in turn implies very high pore pressure yet to be observed in SAFOD. For a relatively high r value near 1 ($\sigma_h \sim \sigma_V$), a model compatible with fault normal compression that can explain the relative weakness of the SAF may not be sufficiently weak in the absolute sense to satisfy the heat flow constraint. To clarify this issue, we consider the stresses associated with the end-member scenario illustrated in Figure 1b. The average shear strength of the fault is $\bar{\tau}$, and the pore pressures in the country rock and fault zone will be assumed to be hydrostatic. The shear stress is assumed to increase linearly down to the bottom of the seismogenic layer of thickness L = 14 km (Figure 13a). Mathematical details are presented in Appendix C.

We first consider the case with stress state in the country rock in the thrust faulting regime (Figure 2), as postulated in the *Rice* [1992] model. We plot in Figure 13 the fault angle ψ, effective normal stress and friction coefficient for $\bar{\tau}$ in the range of

10-100 MPa. The angle ψ according to equation (C2) is sensitively dependent on the stress ratio *r*. For small angle ψ, it can be expressed as

$$\psi \approx \frac{1}{2}\frac{\sqrt{1+\mu^2}+\mu}{r\mu}\frac{\tau}{(\sigma_V - p_o)} \tag{8}$$

If the ratio is in the range 0.8-1.0 as inferred from SAFOD pilot hole data [*Hickman and Zoback*, 2004], then the angle ψ must be less than 5° to satisfy the heat flow constraint with $\bar{\tau}$ <20 MPa (Figure 13b). In contrast, the effective normal stress is not sensitive to *r* or $\bar{\tau}$ (Figure 13c). Indeed it can be observed from equation (C3) that, for small angle ψ, the effective normal stress is simply given by

$$\sigma_n - p_f \approx \left(\frac{\sqrt{1+\mu^2}+\mu}{\sqrt{1+\mu^2}-\mu}\right)(\sigma_V - p_o) \tag{9a}$$

In this scenario the effective normal stress is directly proportional to the overburden minus hydrostatic pore pressure. The constant $(\sqrt{1+\mu^2}+\mu)/(\sqrt{1+\mu^2}-\mu)$ ranges from 3.12 to 4.68 for μ=0.6-0.85.

According to (C4), the gouge friction coefficient is directly proportional to the average shear stress, but is basically independent of the ratio *r*. For small angle ψ, it can be written as

$$\mu_f \approx \left(\frac{\sqrt{1+\mu^2}-\mu}{\sqrt{1+\mu^2}+\mu}\right)\frac{\tau}{(\sigma_V - p_o)} \tag{9b}$$

The friction coefficient must be very low ($\mu_f \approx 0.05$) to satisfy the heat flow constraint with $\bar{\tau}$ <20 MPa or so (Figure 13d). Such a value is much lower than the range of 0.1-0.2 often cited as necessary to satisfy the heat flow constraint (Figure 1b).

This apparent discrepancy arises because we have followed *Rice* [1992] to impose the condition that the country rock is in the thrust faulting regime. In contrast, this problem is conventionally analyzed assuming the stress states in both the country rock and fault zone are in the strike-slip regime. In this second scenario, the vertical stress

represents the intermediate principal stress, and the normal stress is expected to fall somewhere between the maximum and minimum horizontal stresses. This leads to the plausible assumption that the normal stress can be approximated by the vertical overburden [*Morrow et al*., 1992; *Moore et al*.,1997; *Moore and Rymer*, 2007] and accordingly, we can write the effective normal stress as:

$$\sigma_n - p_f \approx (\sigma_V - p_o) \tag{10a}$$

and similarly the gouge friction coefficient as

$$\mu_f \approx \frac{\tau}{(\sigma_V - p_o)} \tag{10b}$$

Comparison of (10) with (9) shows that in this second scenario, the normal stress required to satisfy the heat flow constraint is significantly lower (Figure 13c). For the same reason, the friction coefficient required is higher if the country rock is assumed to be in the strike-slip regime, with a value in the range of 0.1-0.2 that is commonly cited.

5.3 Gouge mixtures and fine structure of fault zones

Fault gouges observed in the field and in the laboratory contain a pattern of shear localization along which strain is accommodated. In gouges composed of weak and strong mineral phases, the weak grains are typically found aligned with and on the fracture surface. Textural characteristics and orientation of Riedel shears have been linked to sliding behavior [*Moore et al*., 1989] and reflect the overall weakness of the gouge layer [e.g. *Gu and Wong*, 1992]. *Tembe et al*. [2007] observed in room temperature friction experiments on montmorillonite-illite-quartz mixtures that the gouge's response to velocity perturbation is also a function of mixture composition. Taken together, the overall frictional behavior of a fault zone would be governed by the relative proportion of weak phases and continuity of the shears which are enriched in the weak phase. High-temperature friction experiments on mixtures of serpentine-talc and serpentine-brucite by

[*Moore and Lockner*, 2007] show dramatic weakening in gouge strength such that as in mixtures containing as little as 25 wt.% talc or brucite, the shear strength had reduced by 75% compared to the serpentine end-member. Findings of sheared serpentinite coated with talc support a San Andreas fault that is intrinsically weak, but one would have to consider the fine structure before the implications for the mechanics of faulting are fully understood.

5.4 Velocity weakening in SAFOD gouge

At least three factors may contribute to velocity weakening behavior in the SAFOD gouge experiments in the temperature interval 266 – 283°C. First, the velocity step intervals may by too short to achieve steady-state, giving the impression of negative *a-b* values. Second, while constant pore pressure was maintained in the pore pressure system during the experiment, it was assumed the migration of water in or out of the gouge layer occurs at a rate that keeps up with volumetric changes induced by shearing of the layer. Although we used slow displacement rates to enable a fully drained gouge (velocity steps alternated between 1,000 and 10,000 seconds), in a low-permeability clay material it may be possible to trap fluids and jack up the pore pressure locally reducing the effective stress. There was no indication in the mechanical data that this problem occurred. Third, the narrow temperature range would suggest a chemical origin such as a phase change (for example, smectite to illite) or a dehydration reaction, which would lubricate the grains during sliding.

To determine if the velocity weakening was due a phase change we must identify the minerals involved in the reaction and determine the reaction temperature and kinetics at pressures relevant to our experimental conditions. The major mineral constituents of the SAFOD gouge are illite, smectite, quartz, and feldspar and previous studies have found a correlation between temperature and the onset of unstable sliding in all these

materials. *Moore et al*. [1989] noted stick-slip behavior in illite at temperatures upwards of 400°C. Studies on wet granite [e.g., *Stesky*, 1978; *Blanpied et al*., 1991] and quartz [e.g., *Higgs*, 1981; *Chester and Higgs*, 1992] also show weakening at elevated temperatures and comparable sliding rates, but the temperatures involved are typically much greater. In contrast, smectite is known to dehydrate at relatively low temperatures and experimental data by *Logan et al.* [1981] on nominally montmorillonite-rich gouge showed stick-slip behavior at 300°C. Dehydration may be related to the illitization of smectite, which is estimated to be complete by 150°C. However, paucity of data at in-situ conditions, uncertainty in the reaction process, and the need for detailed microscopy of our samples leaves this an open question.

Preliminary thermogravimetric and differential thermal analyses conducted at ambient pressure on the starting material revealed dehydration reactions at 20-100 °C and at 400-600 °C, with each stage losing 1.7 wt.% and 2.5 wt.%, respectively of the total initial mass. Data on high-pressure and high-temperature behavior of minerals have shown that the dehydration temperatures will increase under elevated pressures and the dehydration temperature at ambient pressure would have to be extrapolated to our experimental conditions. From a synchrotron study conducted by *Huang et al*. [1994] on Na-montmorillonite they were able to map the pressure-temperature path up to water (H2O) pressures of 535 MPa and temperatures up to 553 °C using a hydrothermal diamond-anvil cell and real-time XRD. They studied montmorillonite with hydrate of one-, two- and three- H2O layers and determined that in a drained sample dehydration of three to two layers would occur at ~270 °C, comparable to our experimental findings. Just beyond the run conditions at ~440 °C, they estimate the two to one layer dehydration. While extensive study would be required, our preliminary analyses suggest smectite

dehydration from three interlayer waters to two at 266-283 °C may be involved in the velocity weakening behavior observed in the intermediate thermo-mechanical regime.

6. Summary

Rice [1992] proposed a model where in the presence of elevated pore pressure frictional failure in a strong fault may occur in near fault normal compression. In light of the recent findings that the SAFOD cores contain weak clay, serpentine an talc phases, the objective of the our study was to extend the *Rice* [1992] model to the more general case with the San Andreas fault gouge having reduced frictional strength. Using the relatively weak black gouge retrieved from 3067 m MD, chrysotile and talc as proxies for the SAF gouge, our predictions of pore pressure excess, which can be up to 3 times the lithostatic stress, can be considered as a lower bound on pressures compatible with the stress orientation data. If we impose the heat flow constraint with $\bar{\tau}$ <20 MPa (leaving ψ and μ_f as free parameters) and assuming the stress ratio is in the range 0.8-1.0, then the angle ψ would be less than 5° and the friction coefficient would be very low ($\mu_f \approx 0.05$). Such values are lower than derived from conventional analysis of the problem, which assume the stress states in both the country rock and fault zone are in the strike-slip regime and that the normal stress can be approximated by the vertical overburden.

Appendix A: Fault zone stress state and pore pressure

With reference to Figure 2, we derive here expressions for the stresses and pore pressure within the fault zone using Mohr circle analysis. Mechanical equilibrium at the interface between country rock and fault gouge necessarily requires the resolved shear

and normal stress to be continuous across this interface [*Rice*, 1992]. Hence the stresses τ and σ_n can conveniently be derived using the Mohr circle for the horizontal principal stresses (σ_H, σ_h) in the country rock. Since the angle between σ_H and the fault normal (aligned with σ_n) is ψ, the resolved shear stress at the interface is

$$\tau = \frac{1}{2}(\sigma_H - \sigma_h)\sin 2\psi = \frac{r}{2}(\sigma_H - \sigma_V)\sin 2\psi \tag{A1}$$

where *r* is a principal stress ratio defined in equation (2). If the rock mass is permeated by randomly distributed fractures and the pore pressure p_o as a function of depth is given by the hydrostatic gradient, then limiting values of σ_V and σ_H are related by equation (1), which we substitute in (A1) to arrive at

$$\tau = \frac{r\mu \sin 2\psi}{\sqrt{1+\mu^2}-\mu}(\sigma_V - p_o) = \frac{r\mu \sin 2\psi}{\sqrt{1+\mu^2}-\mu}(\rho_r - \rho_w)gz \tag{A2}$$

Similarly we can derive the normal stress at the interface

$$\begin{aligned}\sigma_n &= \frac{1}{2}(\sigma_H + \sigma_h) + \frac{1}{2}(\sigma_H - \sigma_h)\cos 2\psi \\ &= p_o + \left[\frac{\sqrt{1+\mu^2}+\mu - r\mu\sin^2\psi}{\sqrt{1+\mu^2}-\mu}\right](\sigma_V - p_o) \\ &= p_o + \left[\frac{\sqrt{1+\mu^2}+\mu - r\mu\sin^2\psi}{\sqrt{1+\mu^2}-\mu}\right](\rho_r - \rho_w)gz\end{aligned} \tag{A3}$$

If the fault is critically stressed in the strike-slip regime, then the tangent with slope equal to the gouge friction coefficient μ_f should touch the gray Mohr circle in Figure 2, which represents the maximum and minimum principal stresses (σ_H^f, σ_f^f) inside the fault zone. With reference to this Mohr circle, it can readily be shown that the principal stresses are given by

$$\sigma_H^f = \sigma_n + \tau(\sqrt{1+\mu^2} + \mu_f) \tag{A4}$$

$$\sigma_h^f = \sigma_n + \tau(\sqrt{1+\mu^2} - \mu_f) \tag{A5}$$

The tangent should intersect the horizontal axis at a point corresponding to the local pore pressure p_f (Figure 2). Furthermore, the frictional failure criterion would require the shear and normal stresses to be related by $\tau = \mu_f(\sigma_n - p_f)$, which implies

$$p_f = \sigma_n - \frac{\tau}{\mu_f} \tag{A6}$$

Substituting (A2) and (A3) into (A4), we therefore obtain

$$\begin{aligned}\lambda = \frac{p_f}{\sigma_V} &= \frac{p_o}{\sigma_V} + \left[\frac{\sqrt{1+\mu^2}+\mu - r\mu(\sin^2\psi + \sin 2\psi/\mu_f)}{\sqrt{1+\mu^2}-\mu}\right]\left(1-\frac{p_o}{\sigma_V}\right) \\ &= \frac{\rho_w}{\rho_r} + \left[\frac{\sqrt{1+\mu^2}+\mu - r\mu(\sin^2\psi + \sin 2\psi/\mu_f)}{\sqrt{1+\mu^2}-\mu}\right]\left(1-\frac{\rho_w}{\rho_r}\right)\end{aligned} \tag{A7}$$

The ratio λ is also called the Hubbert-Rubey coefficient. If the angle ψ is sufficiently small, then the term containing $\sin^2\psi$ in (5a) can be neglected and $\sin 2\psi$ can also be approximated by 2ψ. Our computations show that for $\psi < 20°$ or so, this turns out to be a good approximation for the range of friction coefficient we consider here. The Hubbert-Rubey coefficient can then be approximated by

$$\lambda = \frac{p_f}{\sigma_V} \approx \frac{\rho_w}{\rho_r} + \left(\frac{\sqrt{1+\mu^2}+\mu}{\sqrt{1+\mu^2}-\mu}\right)\left(1-\frac{\rho_w}{\rho_r}\right) - \frac{2\mu}{\sqrt{1+\mu^2}-\mu}\left(\frac{r\,\psi}{\mu_f}\right) \tag{A8}$$

Applying the same approximation to (A3) , we obtain for the normal stress

$$\sigma_n \approx \sigma_H = p_o + \left[\frac{\sqrt{1+\mu^2}+\mu}{\sqrt{1+\mu^2}-\mu}\right](\sigma_V - p_o) \tag{A9}$$

and the effective normal stress

$$\sigma_n - p_f \approx \frac{2\mu}{\sqrt{1+\mu^2}-\mu}\left(\frac{r\psi}{\mu_f}\right)(\sigma_V - p_o) \tag{A10}$$

Appendix B: Geothermal gradient at Parkfield

To infer the frictional strength at seismogenic depths from our hydrothermal friction data for the SAFOD gouge, we must first specify a geothermal gradient for the

SAF. A comprehensive study of the thermal regime of the SAF near Parkfield was conducted by *Sass et al.* [1997], who adopted the following relation of *Lachenbruch and Sass's* [1977] to extrapolate their heat flow data to temperature T as a function of depth z

$$\theta(z) = T(z) - T_s = \frac{1}{\lambda}\left[(q - DA_o)\ z + D^2 A_o (1 - e^{-z/D}) \right] \tag{B1}$$

The derivation of this relation assumes that radiogenic heat production decays exponentially over depth, with a characteristic decay depth of D=15 km. Here we use a value of A_o=1.5 μWm^{-3} for surface heat flow as suggested by *Sass et al*. [1997]. For the surface heat flow and thermal conductivity λ, we use updated values of q = 77 mWm^{-2} and λ=2.5 Wm^{-1}K^{-1} reported by *Williams et al*. [2004] and *Williams* [1996], respectively. We also assign a surface temperature of T_s=10°C. The geotherm is almost linear with a gradient approximately equal to 28°C/km.

Appendix C: Heat flow constraint

The shear stress is assumed to increase linearly with depth in a seismogenic layer of thickness L:

$$\tau = 2\bar{\tau}\frac{z}{L} \tag{C1}$$

With reference to the Mohr circle associated with principal stresses σ_h and σ_H (Figure 2), we can use equation (A2) to derive the stress orientation:

$$\psi = \frac{1}{2}\sin^{-1}\left(\frac{\tau}{(\sigma_V - p_o)} \frac{(\sqrt{1+\mu^2} - \mu)}{r\,\mu} \right) = \frac{1}{2}\sin^{-1}\left(\frac{2\bar{\tau}}{(\rho_r - \rho_w) g L} \frac{(\sqrt{1+\mu^2} - \mu)}{r\,\mu} \right) \tag{C2}$$

The pore pressures in the country rock and fault zone are both assumed to be hydrostatic. Hence, we can substitute into (A3) to calculate the effective normal stress:

$$\sigma_n - p_f = \sigma_n - p_o = \left(\frac{\sqrt{1+\mu^2} + \mu - r\,\mu \sin^2\psi}{\sqrt{1+\mu^2} - \mu} \right) (\sigma_V - p_o)$$
$$= \left(\frac{\sqrt{1+\mu^2} + \mu - r\,\mu \sin^2\psi}{\sqrt{1+\mu^2} - \mu} \right) (\rho_r - \rho_w) gz \qquad \text{(C3)}$$

The gouge friction coefficient that is compatible with such a shear stress profile can then be determined either by substituting (C3) into the relation $\mu_f = \tau/(\sigma_n - p_o)$, or by imposing the condition $p_f = p_o$ in (5a):

$$\mu_f = \left(\frac{\sqrt{1+\mu^2} - \mu}{\sqrt{1+\mu^2} + \mu - r\,\mu \sin^2\psi} \right) \frac{\tau}{(\sigma_V - p_o)}$$
$$= \left(\frac{\sqrt{1+\mu^2} - \mu}{\sqrt{1+\mu^2} + \mu - r\,\mu \sin^2\psi} \right) \frac{2\bar{\tau}}{(\rho_r - \rho_w) gL} \qquad \text{(C4)}$$

Acknowledgments

We thank Diane Moore for her for her advice in the lab and for providing us with her unpublished talc data. Microprobe analyses were conducted by Francis McCubbin. We have benefited from discussions with Stephen Hickman, Diane Moore, Carolyn Morrow, John Parise, and Colin Williams. Sheryl Tembe was supported by a Department of Education GAANN fellowship. This research was partially supported by US National Science Foundation under grant EAR-0346022.

References

Boness, N.L., and M.D. Zoback, (2004), Stress induced seismic velocity anisotropy and physical properties in the SAFOD pilot hole in Parkfield, CA, *Geophys. Res. Lett.*, 31, doi:10.1029/2003GL019020.

Boness, N.L., and M.D. Zoback, (2006), A multiscale study of the mechanisms controlling shear velocity anisotropy in the San Andreas Fault Observatory at Depth, *Geophys.*, 71 (5), F131-F136.

Brace, W.F., and D.L. Kohlstedt, (1980) Limits on lithospheric stress imposed by laboratory experiments, *J.Geophys. Res*., 85, B11, 6248-6252.

Bredehoeft, J. D., and S. E. Ingebritsen (1990), Degassing of carbon dioxide as a possible source of high pore pressure in the crust, in *The Role of Fluids in Crustal Processes*, edited, pp. 158-164, National Academy Press, Washington, D.C.

Brune, J.N., T. Henyey, and R. Roy, (1969) Heat flow, stress, and rate of slip along San Andreas fault, California, *J. Geophys. Res*., 74, 3821-4009.

Byerlee, J.D., (1978) Friction of rocks, *Pure and Applied Geophysics*, 116, 615-26.

Byerlee, J.D., (1990), Friction, overpressure, and fault normal compression, *Geophys. Res.Lett.*, 17, 2109-2112.

Dieterich J.H. (1979) Modeling of rock friction:1. Experimental results and constitutive equations, *J. Geophys. Res.* 84, 2161–68.

Gu, Y., and T.-f. Wong (1994), Development of shear localization in simulated quartz gouge: Effect of cumulative slip and gouge particle size, *Pure Appl. Geophys., 143*, 387-424.

Hickman, S., and M.D. Zoback, (2004), Stress orientations and magnitudes in the SAFOD pilot hole, *Geophys. Res. Lett*., 31, doi:10.1029/2004GL020043.

Lachenbruch, A., and J. Sass, (1977), Heat flow in the United States and the thermal regime of the crust, in *The Earth's Curst: Its Nature and Physical Properties, Geophys. Monogr. Ser*., 20, edited by J.G. Heacock, 626-675, AGU, Washington D.C.

Lachenbruch, A., and J. Sass, (1980), Heat flow and energetics of the San Andreas fault zone, *J. Geophys. Res*., 85, 6185–222.

Lachenbruch, A., and J. Sass, (1992), Heat flow from Cajon Pass, fault strength, and tectonic implications, *J. Geophys. Res*., 97, 4995-5015.

Moore, D. E., R. Summers, J.D. Byerlee (1989), Sliding behavior and deformation textures of heated illite gouge, *J. Struct. Geol., 11,* (3) 329-342.

Moore, D.E., D.A. Lockner, H. Tanaka, and K. Iwata, (2004), The coefficient of friction of chrysotile gouge at seismogenic depths, in *Serpentine and Serpentinites: Minerology,* Petrology, Geochemistry, Geology, Geophysics, and Tectonics, ed. W.G. Ernst, and B.J. Skinner, GSA Int. Geol. Rev., 46, 385-398.

Moore, D. E., D. A. Lockner, (2007), Comparative deformation behavior of minerals in serpentinized unltramafic rock: Application to the slab-mantle interface in subduction zones, *Int. Geol. Rev.,* 49, 401-415.

Morrow, C.A., B. Radney, and J.D. Byerlee, (1992), Frictional strength and the effective pressure law of montmorillonite and illite clays, in *Fault Mechanics and Transport Properties of Rocks*, ed. B. Evans, and T.-f. Wong, 69-88, Academic Press, San Diego.

Morrow, C., J.G. Solum, S. Tembe, D.A. Lockner, T.-f. Wong, (2007), Using drill cutting separates to estimate the strength of narrow shear zones at SAFOD, *Geophysical Research Letters*, 34, L11301, doi:101029/2007GL029665.

Mount, V.S. and J. Suppe, (1987), State of stress near San Andreas fault: Implications for wrench tectonics, *Geology*, 15, 1143-1146.

Rice, J.R., (1992), Fault stress states, pore pressure distributions, and the weakness of the San Andreas fault, in Fault mechanics and Transport Properties of Rocks, ed. B. Evans, and T.-f. Wong, 475-504, Academic Press, San Diego.

Sass, J., C. Williams, A.H. Lachenbruch, S.P Galanis Jr., and F.V. Grubb (1997), Thermal regime of the San Andreas Fault near Parkfield, California, *J. Geophys. Res*., 102, 27,575-27,585.

Schleicher, A.M., B.A. van der Pluijm, J.G. Solum, L.N. Warr, (2006) Origin and significance of clay-coated fractures in mudrock fragments of the SAFOD borehole (Parkfield, California), *Geophys. Res. Lett., 33,* L16313, doi:10.1029/2006GL026505.

Solum, J.G., S.H. Hickman, D.A. Lockner, D.E. Moore, B.A. van der Pluijm, and J.P. Evans, (2006), Mineralogical characterization of protolith and fault rocks from the SAFOD main hole. *Geophys. Res. Lett., 33,* L21314, doi:10.1029/2006GL027285.

Solum, J.G., (2007) What have learned about faults and earthquakes? Using a view from SAFOD to increase understanding of fault behavior, EarthScope National Meeting Abstracts, 177.

Tembe, S., D.A. Lockner, J.G. Solum, C.A. Morrow, T.-f. Wong, D.E. Moore (2006), Frictional strength of cuttings and core from SAFOD drillhole phases 1 and 2, *Geophys. Res. Lett*., 33, L23307, doi:10.1029/2006GL027626.

Tembe, S., D.A. Lockner, T.-f. Wong, (2007), Effect of clay content and mineralogy on frictional sliding behavior of simulated gouges: Binary and ternary mixtures of quartz, illite and montmorillonite, *J. Geophys. Res*., *submitted MS#2007JB005290.*

Townend, J., and M. D. Zoback (2001), Implications of earthquake focal mechanisms for the frictional strength of the San Andreas Fault system, in The Nature and Tectonic Significance of Fault Zone Weakening, edited by R. E. Holdsworth et al., Geol. Soc. Spec. Publ., 186, 13– 21.

Townend, J., and M. D. Zoback (2004), Regional tectonic stress near the San Andreas Fault in central and southern California, Geophys. Res. Lett., 31, L15S11, doi:10.1029/2003GL018918.

Wiersberg, T., and J. Erzinger (2007) A helium isotope cross-section study through the SanAndreas Fault at seismogenic depths, *Geochemistry Geophysics Geosystems*, 8(1):Q01002.

Williams, C., (1996), Temperature and the seismic/aseismic transition: Observations from the 1992 Landers earthquake, *Geophys. Res. Lett*., 23, 2029-2032.

Williams, C., F.V. Grubb, and S.P. Galanis, (2004), Heat flow in the SAFOD pilot hole and implications for the strength of the San Andreas Fault, *Geophys. Res. Lett*., 31, doi:10.1029/2003GL019352.

Zoback, M.D., et al. (1987), New evidence for the state of stress on the San Andreas fault system, *Science*, 238, 1105-1111.

Table 1. Experimental conditions. One standard deviation for uncertainty in *a*-*b* is 0.0004.

Run #	Temp. (°C)	Depth (km)	$\sigma_n - p_f$ (MPa)	τ (MPa)	μ_f at 3.2 mm axial disp.	$a - b$
1	96	3.0	38	12	0.41	0.0070
12	100	3.15	75	31	0.40	0.0107
2	189	6.3	76	32	0.42	0.0063
4	223	7.5	95	44	0.46	0.0035
8	266	9.0	76	38	0.50	- 0.0043
7	266	9.0	113	62	0.54	- 0.0056
11	266	9.0	226	129	0.57	- 0.0013
3	283	9.6	113	68	0.60	- 0.0043
9	349	12.0	100	68	0.68	- 0.0006
5	349	12.0	150	102	0.68	0.0068
10	349	12.0	300	197	0.65	0.0122
6	431	15.0	188	137	0.73	0.0115

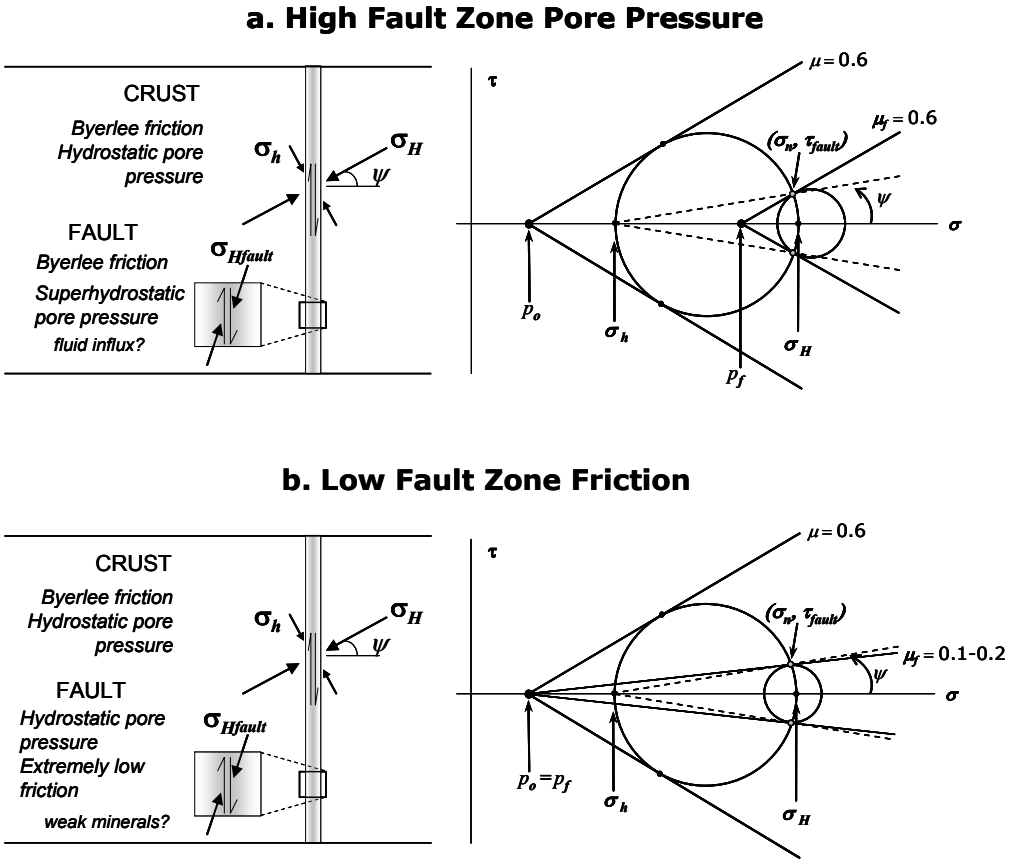

Figure 4.1. End-member models for fault weakening hinge on a strike-slip faulting regime in the country rock (large circle) surrounding the SAF with Byerlee frictional strength. The vertical overburden stress ranges between the minimum and maximum horizontal stress. The fault zone stress state is represented by the small circle. The point of intersection of the two circles is determined by the angle ψ and marks the shear and normal stresses, which are continuous across the interface. a) If elevated pore pressure can be generated and maintained in the fault zone, then frictional failure can occur at low shear stress in an otherwise strong crust and strong fault. b) If the fault zone pore pressure is hydrostatic, then the fault zone must be intrinsically weak.

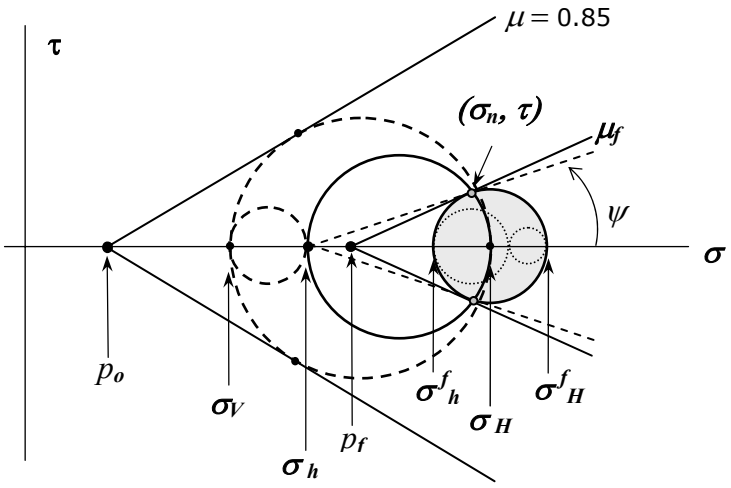

Figure 4.2. Mohr circle diagram modified after *Rice* [1992] showing a critically stressed crust in a thrust faulting regime (large dashed circle) and a critically stressed fault under strike-slip failure (grey circle). The intermediate stress is unconstrained, but can be assigned a value by the parameter *r*. In the original *Rice* [1992] model $\mu = \mu_f = 0.6$. In our modified version the friction coefficient of the crust has a Byerlee friction coefficient of 0.85 and the fault zone coefficient of friction is allowed to vary. The angle ψ (dashed line) is drawn in the plane of the horizontal stresses (circle with solid line) and determines the shear and normal stresses continuous across the interface. The tangent with a slope corresponding to the fault zone friction coefficient must pass through this point. Where the line intersects the horizontal axis is the fault zone pore pressure.

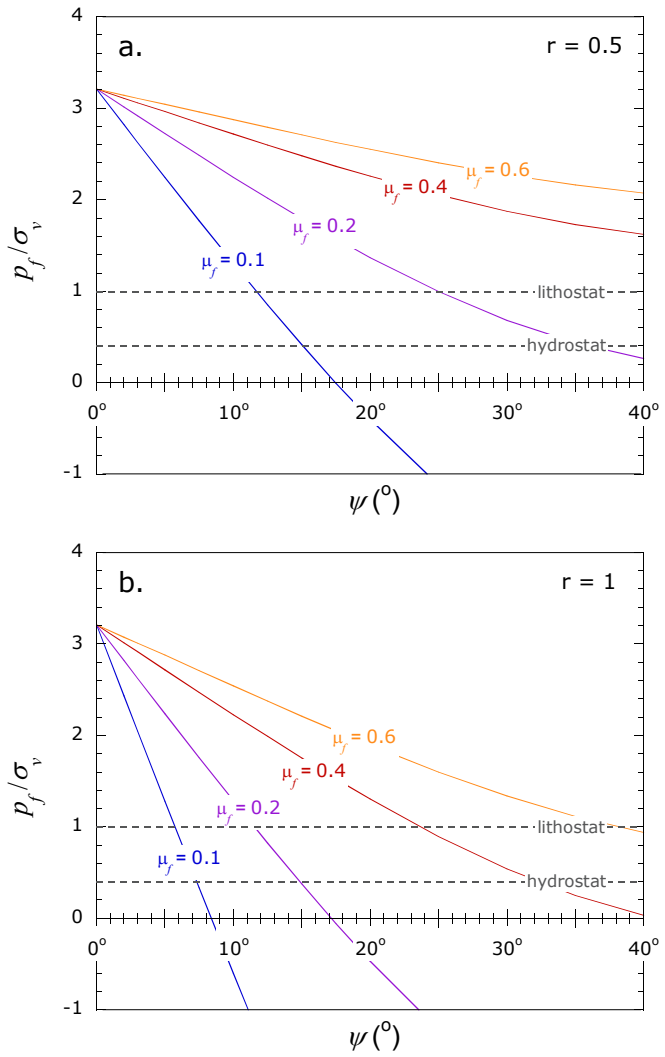

Figure 4.3. Hubbert-Rubey pore pressure coefficient for the fault zone as a function of the fault angle for a range of friction coefficients. a) H-R coefficient for r =0.5 and b) H-R coefficient for r =1. The hydrostatic and vertical overburden in the country rock are shown for reference as the dashed lines. H-R coefficients below zero are not permissible. The Hubbert-Rubey parameter is sensitive to the friction coefficient and linearly dependent on fault angle when the angle is small.

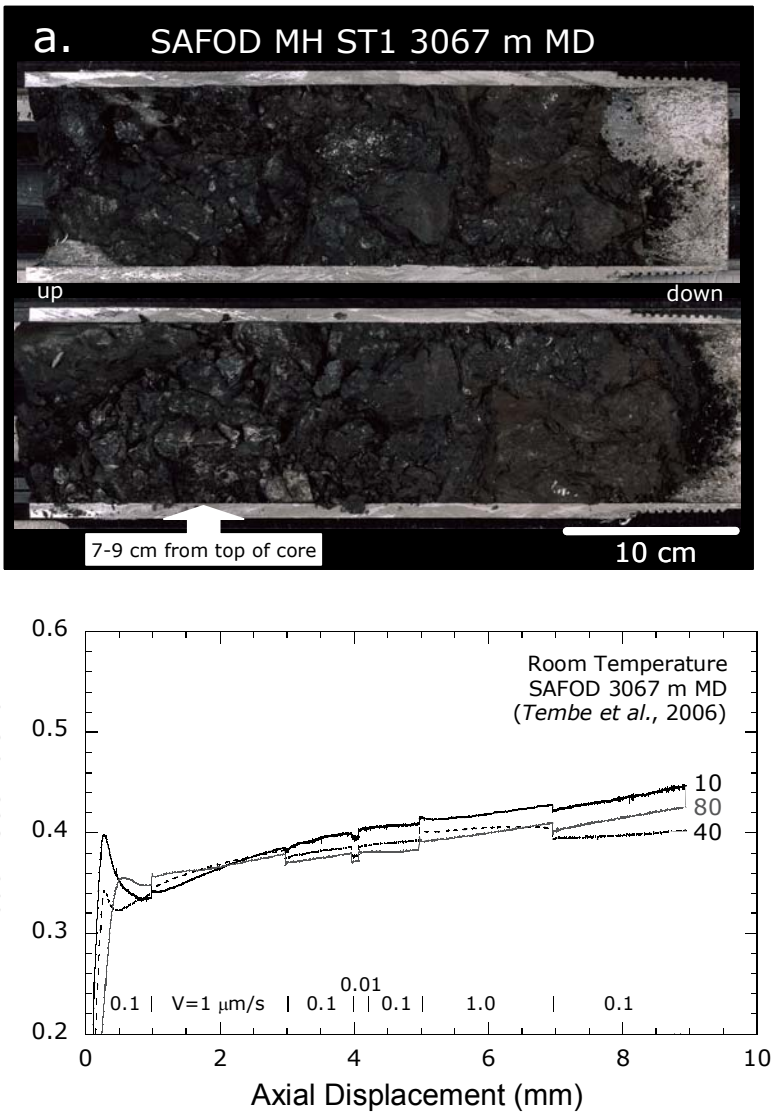

Figure 4.4. a) Section of spot core from SAFOD MH showing the 30 cm thick shear zone. The arrow points to the location of the laboratory samples used in the high-temperature study and by *Tembe et al.* [2006]. b) Room-temperature friction experiments conducted on the material have moderate strength and velocity strengthening behavior.

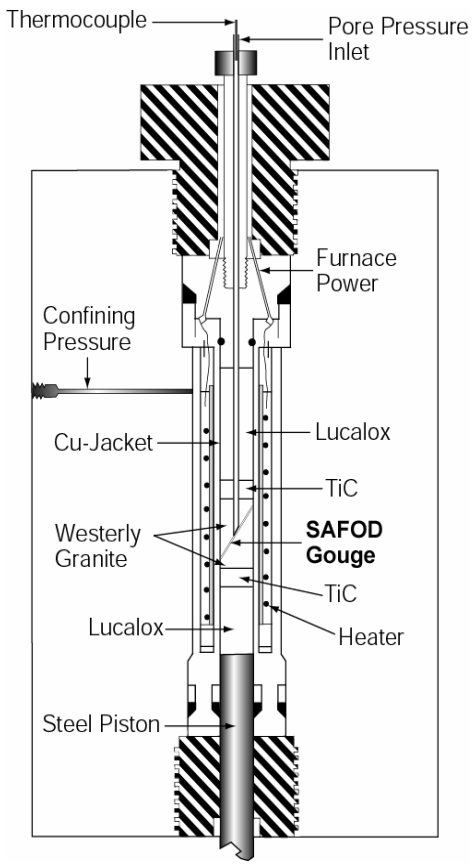

Figure 4.5. Experimental set-up for high-temperature saw-cut experiments.

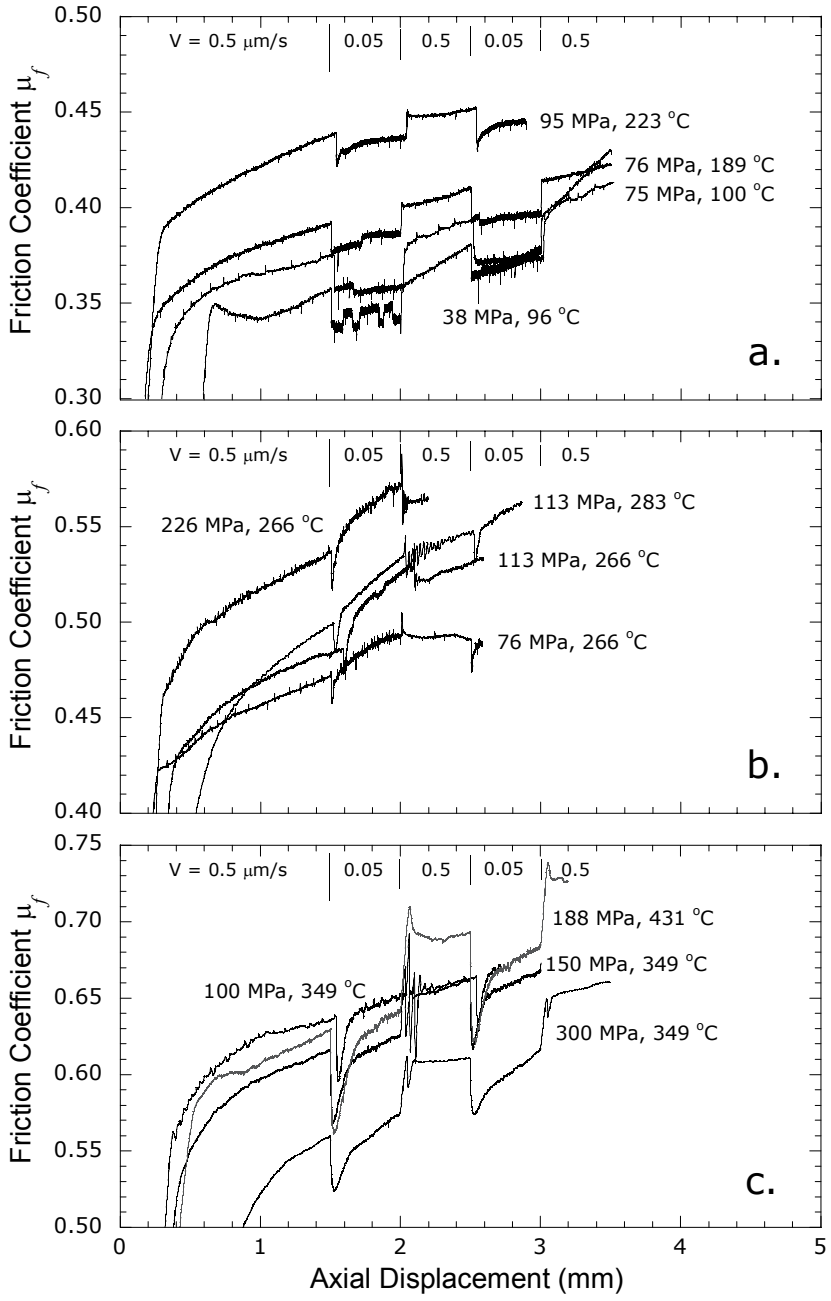

Figure 4.6. Friction coefficient-displacement curves for experimental runs on the black gouge at the indicated effective normal stress (σ_n - p_f) and temperature. The maximum axial displacement reached was 3.5 mm (corresponding to 4.04 mm resolved on the saw-cut) at alternating axial displacement rates of 0.5 and 0.05 μm/s. The frictional sliding behavior can be characterized by three regimes at: a) low-temperature (T<266°C) with velocity strengthening behavior, b) intermediate temperature (266°C≤T ≤283°C) with velocity weakening, and c) high temperature (T >283°C) with velocity strengthening behavior.

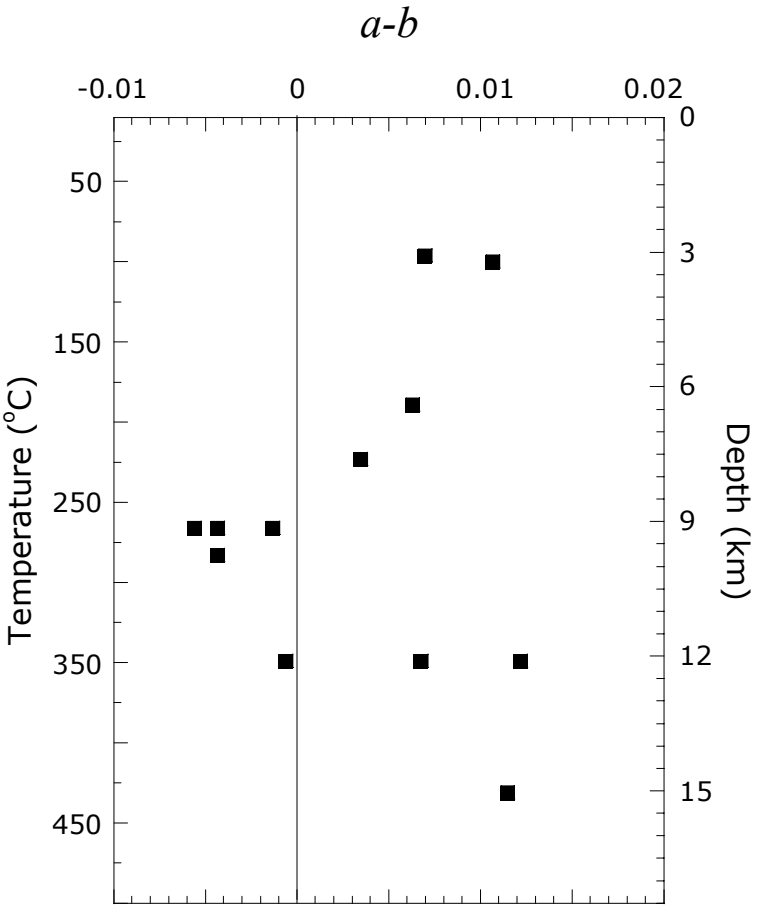

Figure 4.7. Velocity dependence of steady state friction for the SAFOD 3067 m MD black gouge as a function of temperature. Symbol size is proportional to the uncertainty. The corresponding depths were calculated from thermal gradient for the Parkfield region (Appendix B).

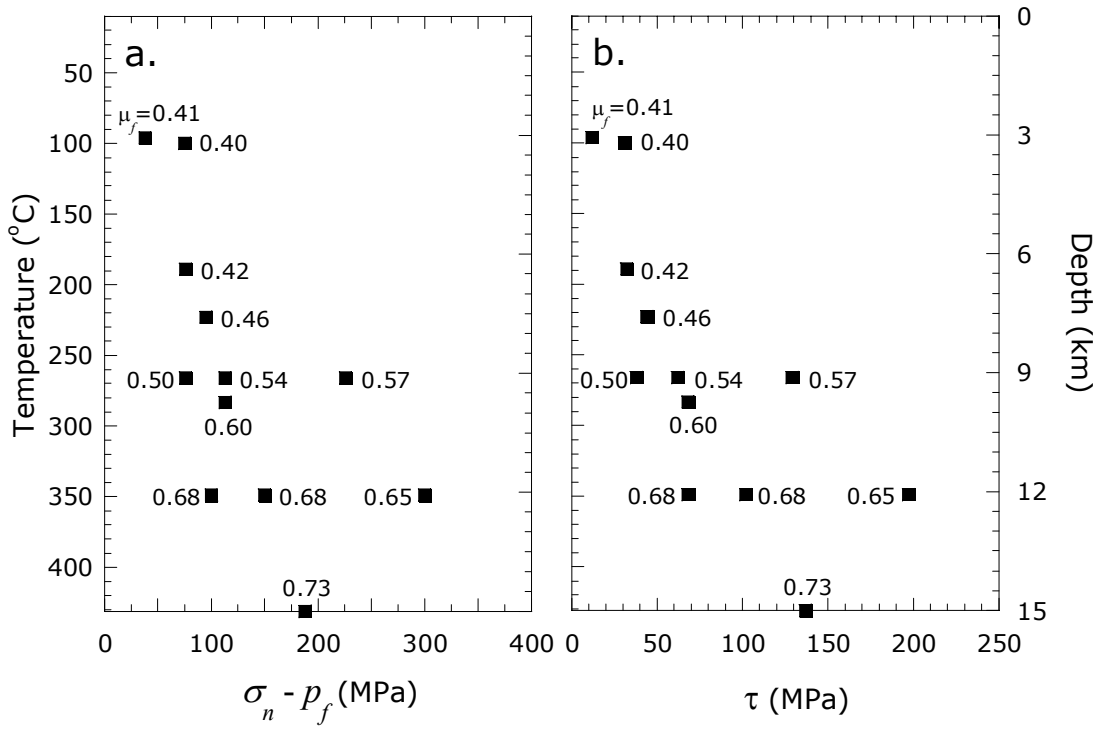

Figure 4.8. a) The effective normal stress in the gouge layer is analogous to the effective normal stress in the fault zone. The measured friction coefficient (indicated for each point) for the SAFOD gouge increases with increasing temperature and depth and varies slightly with the effective normal stress for a given temperature. b) Shear stress as a function of temperature and depth in the experiments.

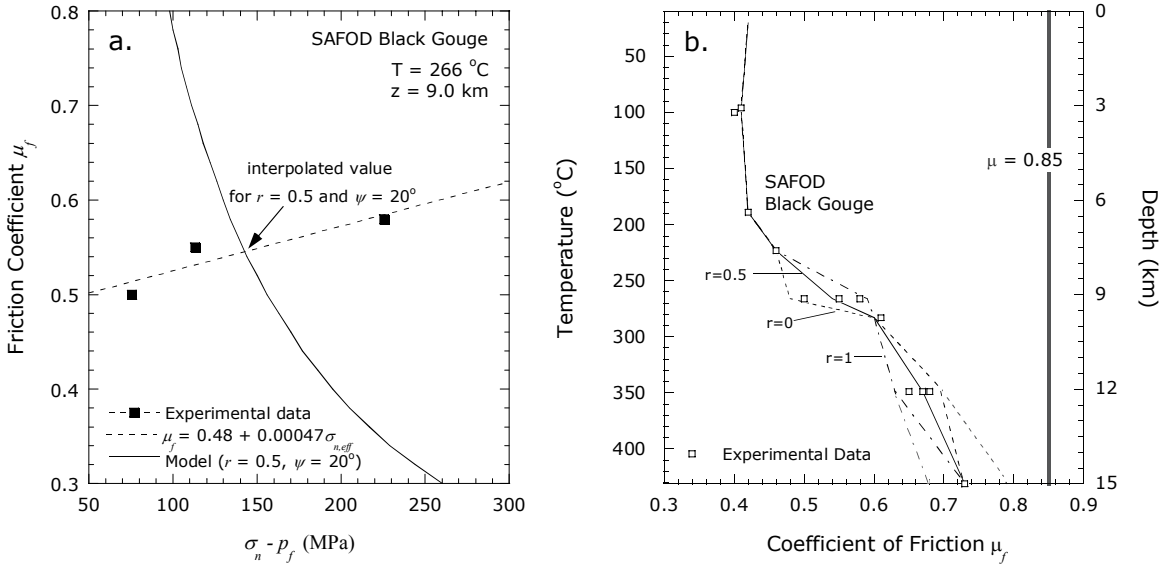

Figure 4.9. a) For multiple experimental runs at a single temperature, interpolated values were determined for effective normal stress and friction coefficient for r=0, 0.5, and 1. The example depicted is for T = 266°C, z = 9 km, the experimental data are fit with a line giving the friction coefficient is a function of effective normal stress. The solid line is the model prediction for the stress state defined by r=0.5 for a range of friction coefficients. The point where the lines intersect represents the optimal friction coefficient and shear stress for the modified considered. This approach can only be applied to when the normal stress dependence is sufficiently constrained, which requires more than one data point. b) Experimental and interpolated coefficient of friction as functions of temperature and depth for r=0, 0.5 and 1. These values are plugged into to the model to generate fault zone stress and pore pressure predictions. The grey dashed lines between 12-15 km represent the trajectories of r=0 and r=1. Since only one experiment was conducted at this temperature-depth, the true friction coefficient is unknown.

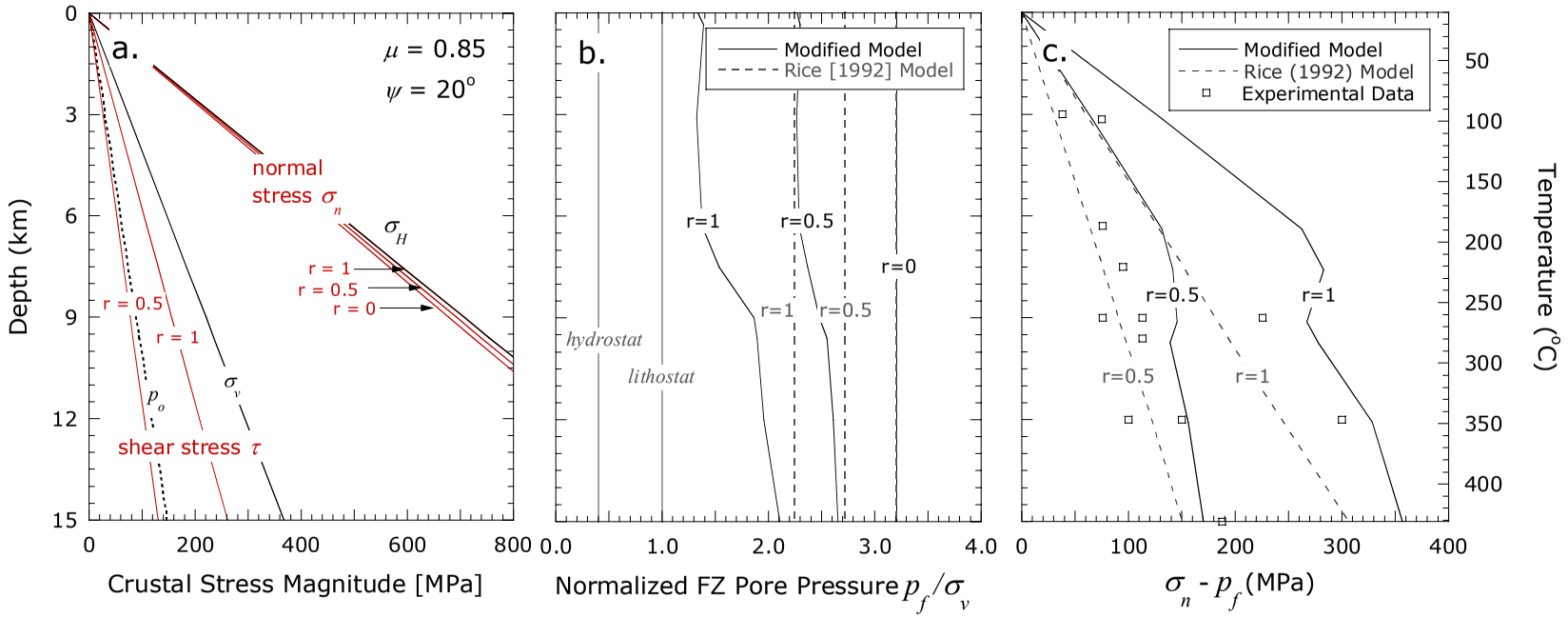

Figure 4.10. a) Stresses in the crust for *r*=0, 0.5, and 1. The stress magnitudes are constrained only by the hydrostatic and lithostatic stresses, and friction coefficient of the crust and do not vary with fault zone parameters. b) Vertical distribution of fluid pressure (in terms of the Hubbert-Rubey coefficient) in an illite-rich fault zone predicted by the modified (solid lines) and original Rice [1992] model (dashed lines). The hydrostat and lithostat are included for reference c) Effective normal stress in the fault zone.

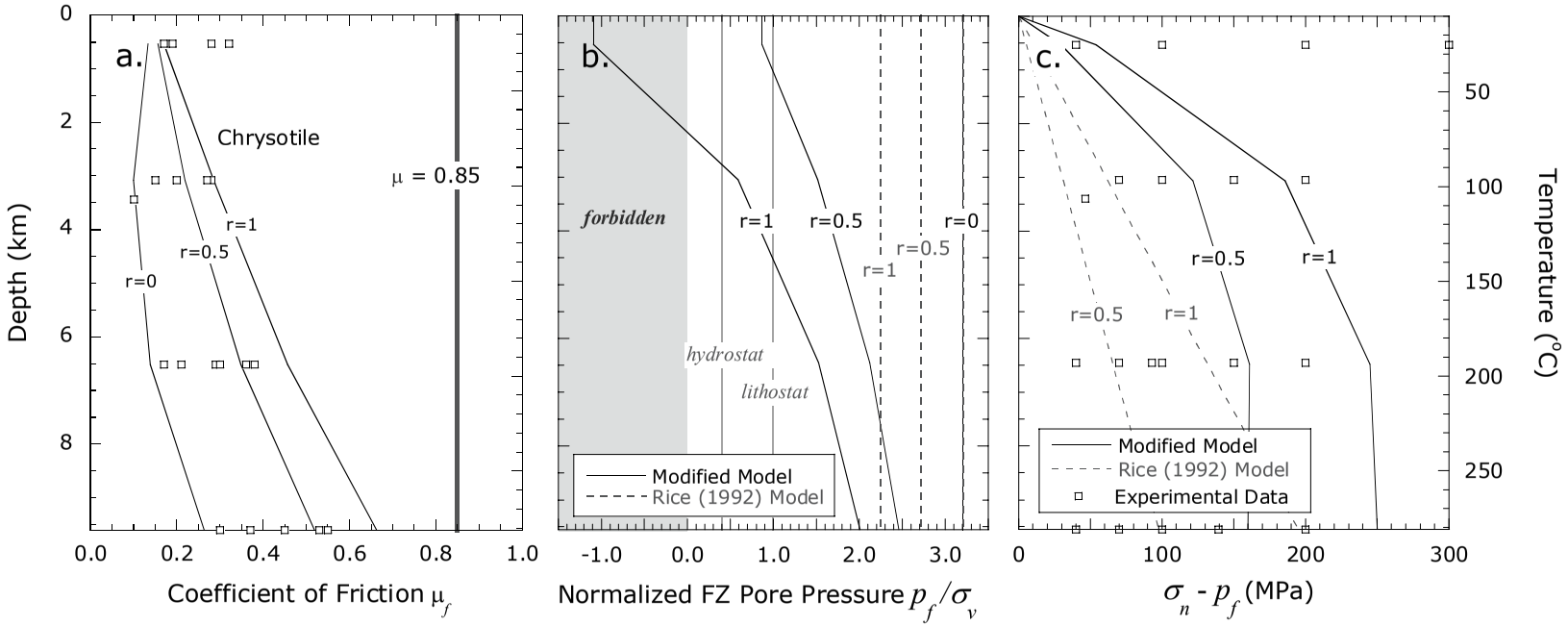

Figure 4.11. a) Interpolated friction coefficient for chrysotile used in our modified models. b) Vertical distribution of fluid pressure (in terms of the Hubbert-Rubey coefficient) in a chrysotile fault zone predicted by the modified (solid lines) and original Rice [1992] model (dashed lines). The hydrostat and lithostat are included for reference c) Effective normal stress in the fault zone. The crustal stresses are the same as in Figure 10a.

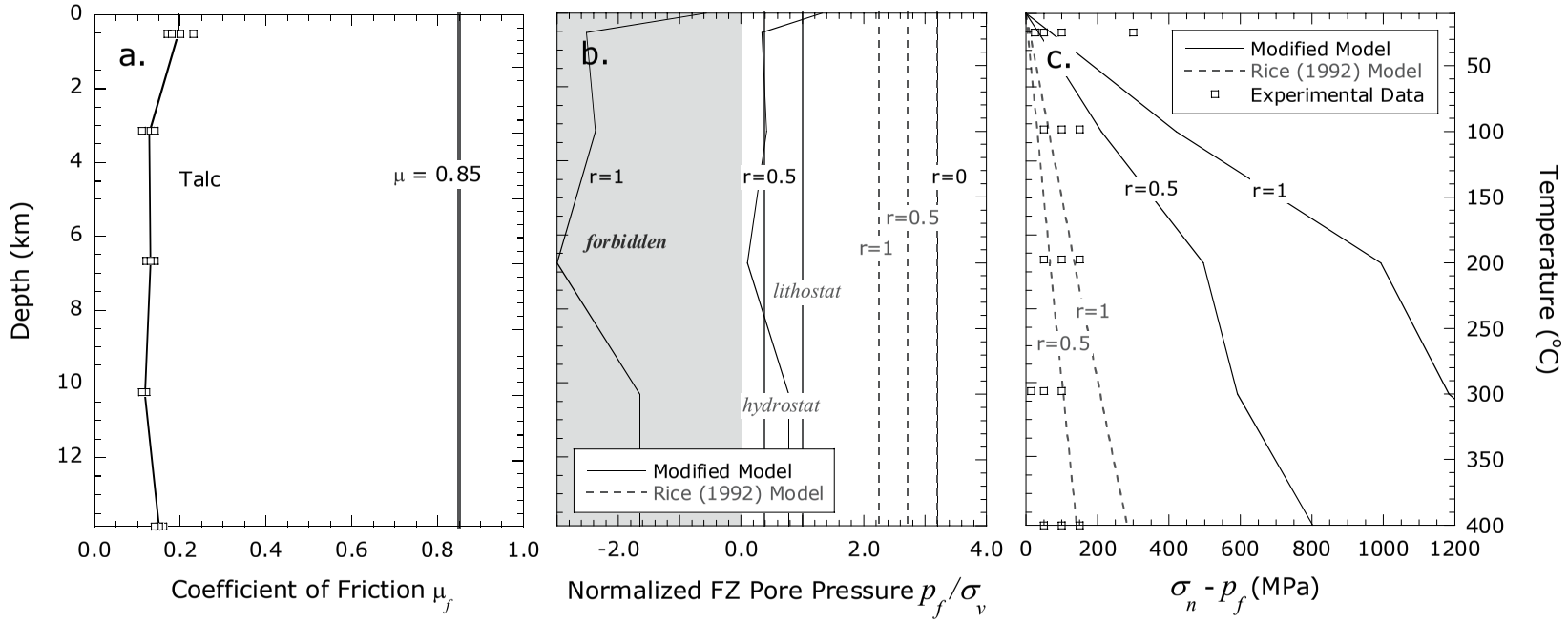

Figure 4.12. a) Variation of friction coefficient of talc over depth. Since the interpolation scheme could not be applied to talc, and average value was used in the model . b) Vertical distribution of fluid pressure (in terms of the Hubbert-Rubey coefficient) in a talc fault zone predicted by the modified (solid lines) and original Rice [1992] model (dashed lines). The hydrostat and lithostat are included for reference c) Effective normal stress in the fault zone. The crustal stresses are the same as in Figure 10a.

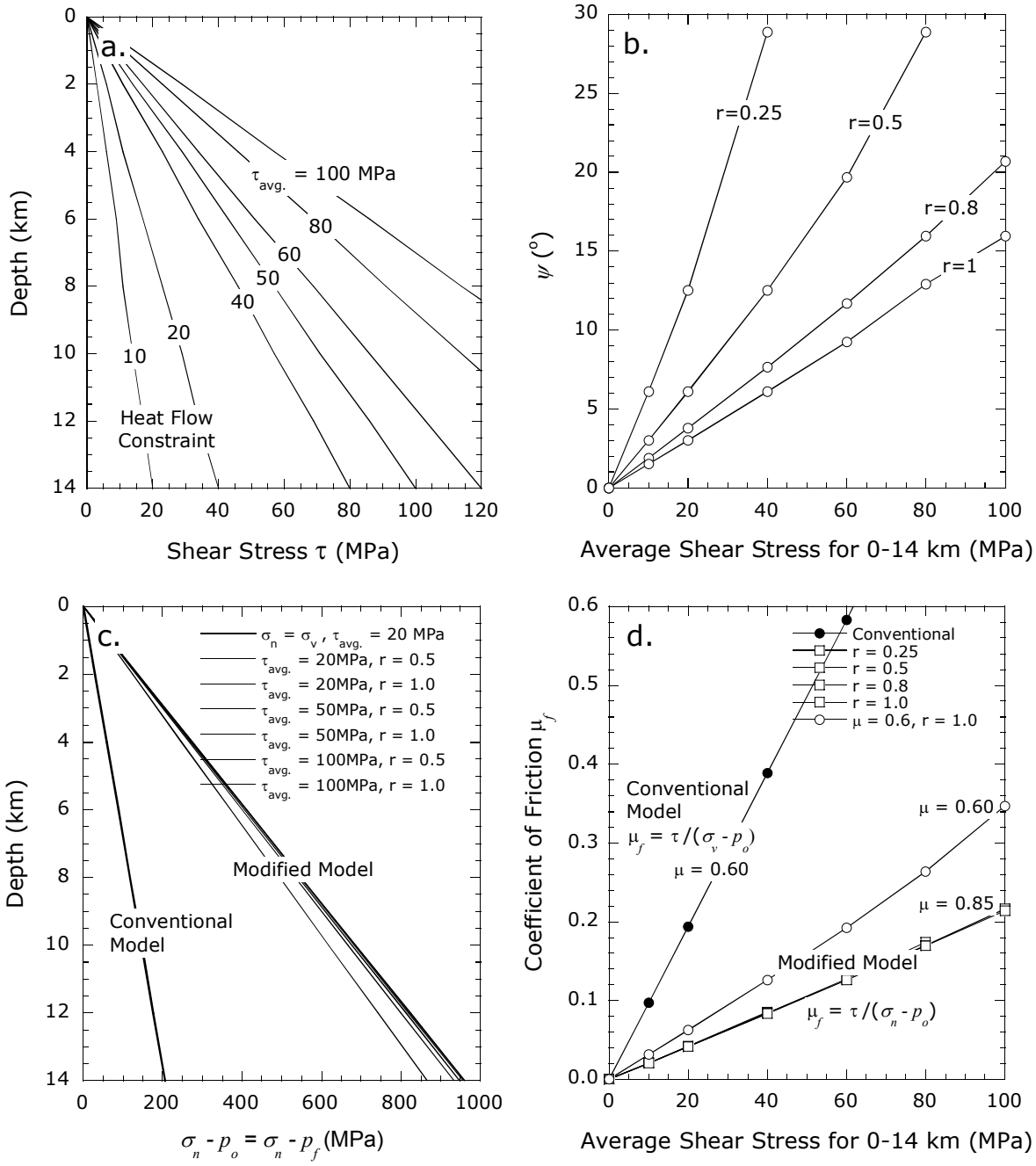

Figure 4.13. a) Shear stress on the fault as a linearly increasing function of depth. The average stress was calculated over a 0-14 km depth interval. b) Fault angle as a function of average shear stress. The fault angle is dependent on the shear stress and inversely dependent on *r*. To satisfy the heat flow constraint of 10-20 MPa and SAFOD findings of *r*~0.8-1, the fault angle must be very small. For a strong fault with shear stress of 100 MPa and *r*~0.8-1, the fault angle would be 16-21°. c) Effective normal stress in the fault zone for the end-member presented in Figure 1b (where $p_f = p_o$) assuming the overburden

stress is equivalent to the normal stress (conventional model) or assuming the normal stress is as given by the modified model. The effective normal stress in the modified model is insensitive to the shear stress and *r*. d) With the shear stress and normal stress defined in (a) and (c), the coefficient of friction for the fault zone can be calculated for the conventional and modified models. The modified friction coefficients are insensitive to *r* and are significantly lower than the conventional model. To satisfy the heat flow constraint, the fault zone friction coefficients must be 0.1-0.2 and <0.05 in the conventional and modified, respectively.

Chapter 5

Summary and Path Forward

1. Major findings

The frictional properties of SAFOD materials were investigated in the laboratory at in-situ conditions. Experiments were conducted in the saw-cut geometry on thin gouge layers under water-saturated conditions. Several questions were posed at the outset of the study regarding the rheology of San Andreas fault materials.

In chapter 2 we developed a method of obtaining meaningful friction data from typically underutilized cuttings samples. A preliminary strength-depth profile of the rocks in the vicinity of SAFOD materials was constructed and several shear zones of low to moderate strength were identified. Mineralogy was an important factor controlling frictional strength and it was noted that illite and smectite clays were present in many SAF shear zones.

The experimental study of quartz-clay mixtures presented in chapter 3 is the first set of data conducted on ternary mixtures at pressures relevant to faulting. As in low-pressure experiments conducted in rotary shear apparatus where strength decreases

nonlinearly with increasing clay content over three regimes, it was demonstrated that at elevated pressures the three regimes persist in mixtures of clay and quartz. For illite and/or montmorillonite-bearing gouges significant strength degradation occurred at ~20 wt.% and producing a gouge that was up to 50 % weaker than the quartz end-member. A second transition in strength was observed at clay contents around ~70 wt.%. Each mechanical regime was associated with characteristic textures containing Riedel shear fractures, comminuted quartz grains and clay foliation. Although requiring further investigation, slip behavior was also observed to vary with composition.

In chapter 4 gouge strength and fault zone fluid pressure were manipulated in *Rice* [1992]-style models. Hydrothermal laboratory data (on SAFOD illite gouge, chrysotile, and talc) and geophysical observations of heat flow around the San Andreas fault constrain the stress state and pore pressure in the modified model. We showed that if the σ_H is at high angle (~70°) to the fault and σ_h is comparable to the lithostatic stress, then fault zone pore pressure would have to be up to 3 times the lithostatic stress for failure. Previous models and stress analyses in the literature assume the vertical stress is comparable to the normal stress acting on the fault yielding friction coefficients of 0.1-0.2. An important departure in the *Rice* [1992] model and confirmed by findings at SAFOD, is that the lithostatic stress is the least principle stress in the crust and that the normal stress acting on the fault is comparable to the maximum horizontal stress. Thus, if the heat flow shear stress constraint of 10-20 MPa is imposed, then the fault angle ψ must be very small and the friction coefficient would be <0.05.

2. Research Direction for Phase 3

Results from scientific drilling into the creeping San Andreas fault have shed light on the physical and chemical process involved in earthquake dynamics, and raised a multitude of questions. What is the fluid pressure within and adjacent to the fault zone and how does it vary during a seismic cycle? What are the permeabilities of fault-zone

materials and country rock? How do stress orientations and magnitudes vary across the fault zone?

2.1 Permeability and fault zone architecture

The architectural components of fault zones have characteristic lithologies and spatial dimensions which control whether conduits or barriers for fluid flow may develop in a localized or distributed manner during different stages in the seismic cycle. Fault cores may include clay rich gouge, chemical alteration, highly comminuted grains or breccia in a fine grained matrix, and cataclasites. Bounding either side of the core is the damage zone. The damage zone typically has a permeability that is greater than that of the protolith and core because its extensive fracture network and behaves as a fluid conduit parallel to the fault core.

We have conducted 39 permeability measurements on five SAFOD samples: granodiorite from 1465 m MD (with initial porosity of 3%), arkose sandstone from 3064 m MD (with initial porosity of 6%), conglomerate from 3058 m MD (with initial porosity of 12%), and siltstone from 3066 and 3066.5 m MD (with initial porosities of 3 and 1.5%, respectively). Since most of the SAFOD core samples are relatively tight, these permeability experiments were time consuming, and so far measurements have been on samples under hydrostatic loading because of specimen size limitation but it is worthwhile to conduct additional measurements on samples under differential stress as drill core becomes available. Figure 1a shows the pressure dependence of permeability in samples of various lithologies. Our preliminary permeability data show that at effective pressures up to 35 MPa, the permeabilities of the granodiorite (not shown) at this pressure were on the order of 10^{-18} m^2 and those of the arkose sandstone and siltstone on the order of 10^{-21} m^2. The highest permeabilities, on the order of 10^{-17} m^2 were from conglomerate samples from 3058 m MD.

Figure 1b shows permeability across the 3067 m MD shear zone. The grey line is *in-situ* effective pressure of 35 MPa. Due to its fine grain size, the fault core has a

hydraulic permeability which is spatially variable and is several orders of magnitude less than other components of the fault zone, inhibiting fluid migration across the shear zone. The permeability profile for this minor inactive is consistent with the SAF acting as a hydrologic barrier to fluid migration across the fault. However, to properly assess the role of fluids data from active fault strands is imperative. A fault core that is made up of a thin shear zone results in a structure dominated by the damage zone and can potentially be a fluid pathway during deformation events. On the other hand, a thicker fault core would impede fluid flow because of mineral precipitation and sealing.

2.2 In-situ stress state at SAFOD

The most accurate way to determine stress magnitude is by conducting hydraulic fracture tests in the open hole. Unfortunately, deteriorating hole conditions in the latter phases of SAFOD have made these tests difficult. Alternatively, stress magnitude can be estimated from analysis of well bore failure from methodology developed by *Moos and Zoback* [1990] for crystalline rock. Such a technique requires knowledge of the unconfined compressive strength C_o and tensile strength T_o of the San Andreas fault rocks and well constrained lithostatic stress. The first two parameters can be acquired in the laboratory and the latter can be calculated from the SAFOD density logs. Assuming at least one principal stress is acting the vertical direction and corresponds to the overburden stress then principal stress are limited by

$$\left[\frac{\sigma_1 - p_o}{\sigma_3 - p_o}\right] = \left[\sqrt{1+\mu^2} + \mu\right]^2 \quad (1)$$

In the absence of core, *Hickman and Zoback* [2004] had estimated the stresses in the pilot hole based on an empirical relationship between V_p and C_o. With core now available from phases 1 and 2, the stress magnitude estimates can be revised. As an example, I will present the analysis for 1498 m depth following the methodology of *Moos and Zoback* [1990] on the basis of triaxial compression data on SAFOD granodiorite drill

core recovered from this section of the main hole and lithostatic stress calculated from integrated formation densities.

Our samples were from 1467.9 m, 1462.6 m and 1465.36 m MD and had an initially porosity of 0.79-1.92% and density of 2.74 g/cm^3. Because fractures were pervasive in the drill core, only 6 samples (cut into 18 mm x 45 mm rectangular prisms) were obtained from the 1467.9 m MD core and one each from 1462 m MD and 1465.36 MD (cored into 26 mm diameter x 45 mm tall cylinders). Conventional triaxial compression tests were conducted on nominally dry samples at constant confining pressure between 10 to 160 MPa. The samples were deformed at a constant shortening rate, corresponding to a nominal strain rate of 10^{-5} s^{-1}.

Figure 2 presents the mechanical data for samples from 1467.9 m MD. The peak stress increased with increasing pressure, and the samples strain softened and failed by the development of shear localization. The brittle strength data for all the mechanical tests are compiled in Figure 3a, and for reference the failure envelope for Westerly granite is also included [*Lockner*, 1998]. The brittle strength is sensitively dependent on confining pressure, and possibly, due to its higher porosity and microfractures the SAFOD granodiorite is weaker than the more compact Westerly granite. A linear fit to the peak strength data gives C_o = 184 MPa, comparable to the ~210 MPa inferred by *Hickman and Zoback* [2004] for the pilot hole. The tensile strength of the granodiorite was not determined in the laboratory, however T_o for granitic rocks is typically <10% of the unconfined compressive strength [*Jaeger et al.,* 2007] or 0 to 18 MPa. The normal and shear stresses acting on the developed fracture planes (Figure 3b) during sliding were calculated from the residual stress are presented in Figure 3c. The coefficient of friction for the SAFOD granodiorite is 0.71 and in the context of crustal faulting, this implies that the ratio of stresses must be less than that required to cause frictional failure on preexsistng optimally oriented faults.

The friction failure polygon (Figure 4) for a vertical borehole is a graphical representation of possible horizontal stresses solved in (1) for normal, reverse, and strike-slip faulting styles, assuming $\sigma_3 = \sigma_V$ and $\mu = 1$. The lithostatic stress is 32 MPa at 1464 m depth. The maximum and minimum horizontal stresses in the granodiorite formation with unconfined compressive strength of 184 MPa and tensile strength 0-18 MPa are 86 and 44 MPa, respectively. The inferred stress magnitudes are compatible with a reverse faulting stress regime. Borehole breakout and tensile failure would be predicted in domains that exceed the compressive and tensile strength of the rock. Although the depths at which these features have occurred in the SAFOD main hole has not been analyzed yet, Formation Micro Image logs show pervasive fracturing in the formation.

Figure 5 presents the data along with pilot hole estimates from *Hickman and Zoback* [2004] and is consistent with the style of deformation observed in the Parkfield area. As the quality and availability of core improves estimates of stress magnitudes for the deeper deviated part of the main hole crossing the SAF may be obtained.

An interesting advance in borehole geophysics related to SAFOD is the use of measurement of seismic anisotropy as a stress indicator. In their analysis of log data from the SAFOD Pilot Hole, *Boness and Zoback* [2004] concluded that the direction of maximum horizontal compression (inferred from directions of borehole breakouts) is very consistent with the fast polarization direction of the shear waves, and they attributed this correlation to stress-induced anisotropy due to the preferential closure of pre-existing fractures in this granitic section. If this correlation persists to deeper sections of the main hole, then such seismic anisotropy data can indeed be used as a stress indicator as a function of depth. However, the borehole data from the main hole turn out to be more complex. In the sedimentary sequence penetrated at depth by the SAFOD main hole, the sonic log exhibits two distinct fast shear polarizations: a NE direction in the sandstones

and a NW direction in the siltstone and shale units. *Boness and Zoback* [2006] proposed that while the former arises from structural anisotropy due to laminations in clay and is unrelated to the *in situ* stress field, the latter is stress-induced since the well-cemented sandstone would have mechanical attributes similar to a granite. These hypotheses can be tested when oriented cores [*Pares et al*., 2007] are available from phase 3 drilling.

References

Boness, N.L., and M.D. Zoback, (2006), A multiscale study of the mechanisms controlling shear velocity anisotropy in the San Andreas Fault Observatory at Depth, *Geophysics*, doi:10.1190/1.2231107.

Hickman, S., M.D. Zoback, (2004), Stress orientations and magnitudes in the SAFOD pilot hole, *Geophys. Res. Lett*., 31, doi:10.1029/2004GL020043.

Jaeger, J.C., N.G. Cook, and R.W. Zimmerman, (2007), Fundementals of rock mechanics, Chapter 5, Blackwell Publishers, New York.

Moos, D., M.D. Zoback, (1990), Utilization of observation of well bore failure to constrain the orientation and magnitude of crustal stresses: Application to continental. deep sea drilling project, and ocean drilling program boreholes, *J. Geophys. Res*., 95, 9305-9325.

Pares, J., S. Hickman, A. Schleicher, and B. van der Pluijm, (2007) Paleomagnetic reorientation of the SAFOD borehole, *EarthScope National Meeting Abstracts*, 146.

Rice, J.R., (1992), Fault stress states, pore pressure distributions, and the weakness of the San Andreas fault, in *Fault mechanics and Transport Properties of Rocks*, ed. B. Evans, and T.-f. Wong, 475-504, Academic Press, San Diego.

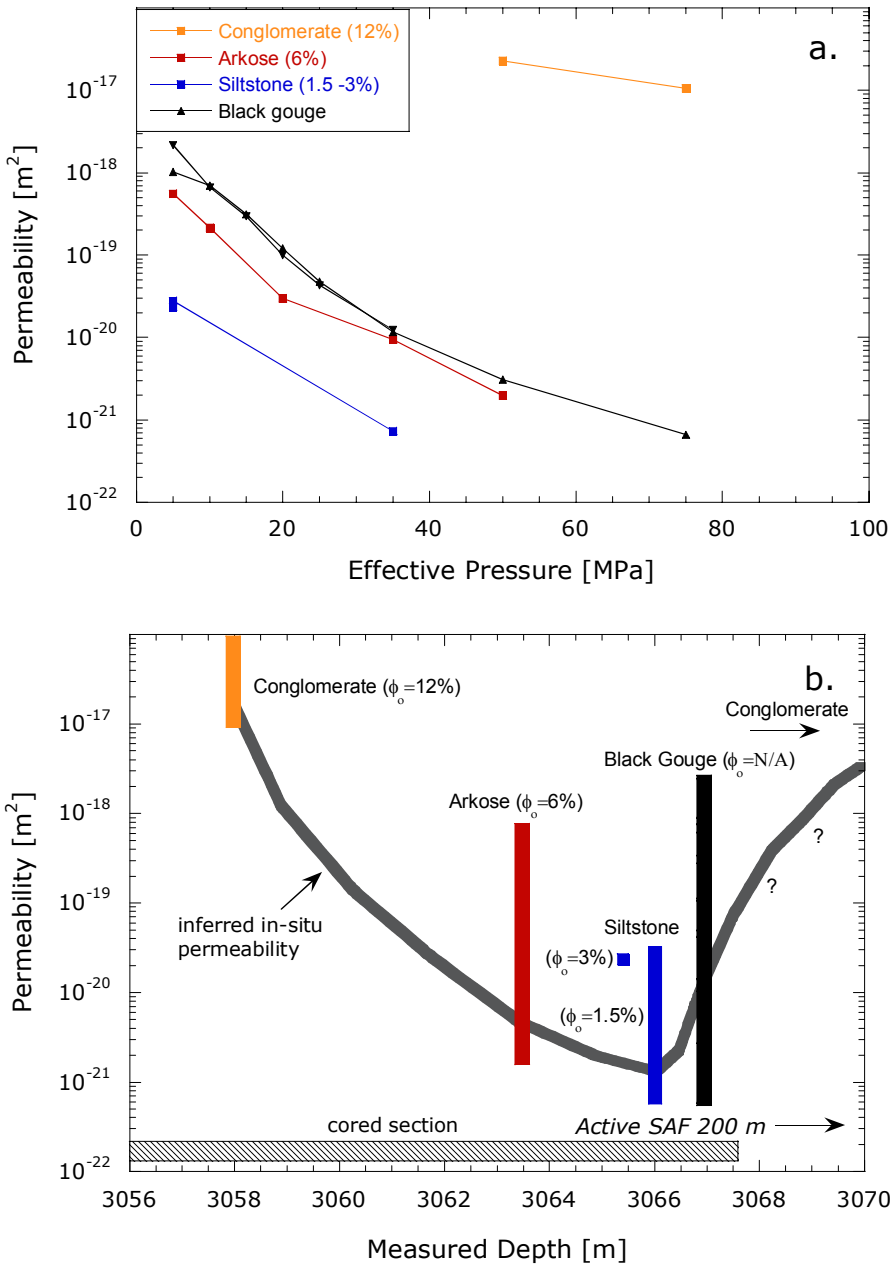

Figure 5.1. Permeability of SAFOD ST1 drill core samples. a) Effective stress dependence of samples from 3058-3067 m MD. b) Permeability of samples at the in-situ effective stress of 35 MPa (indicated by the grey line) reveals an impermeable zone at 3066 m at the interface of the siltstone and black gouge and more permeable damage zone in the arkosic and conglomerate units.

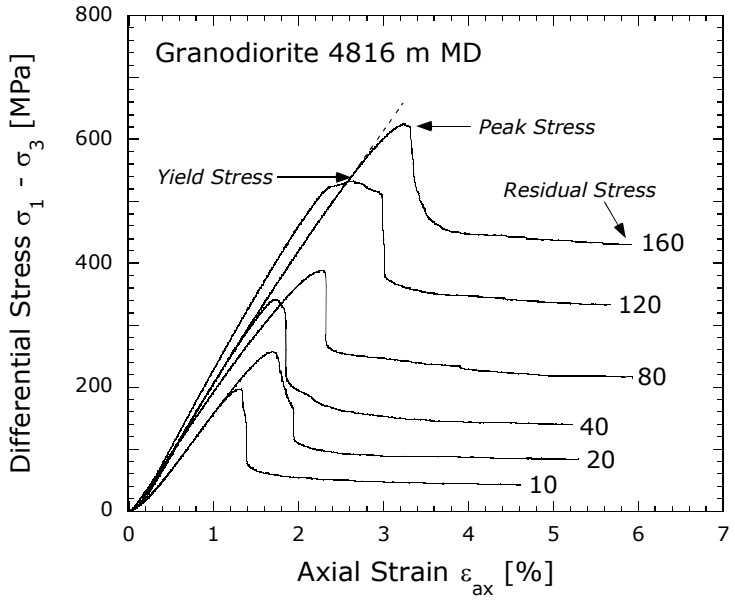

Figure 5.2. Mechanical data for SAFOD ST1 granodiorite core from 4816 m MD tested in the conventional triaxial configuration under dry conditions.

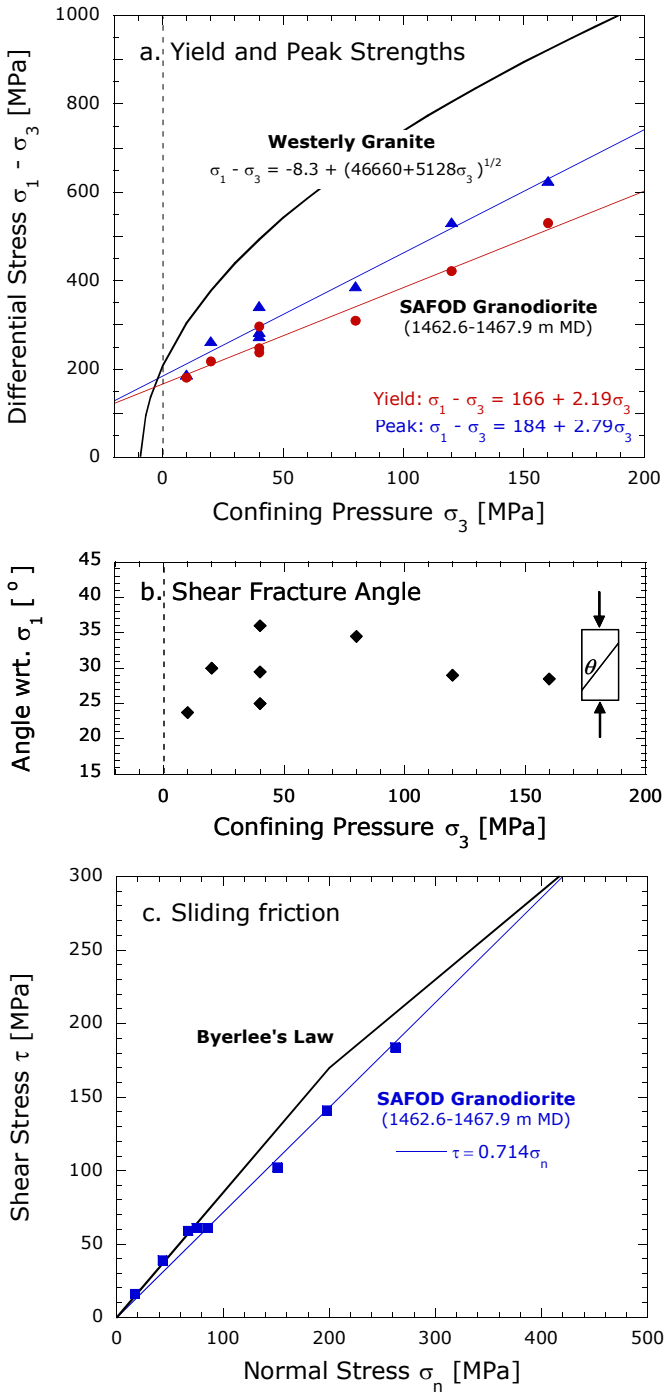

Figure 5.3. a). Brittle failure envelope and critical yield stress of SAFODg ranodiorite obtained from triaxial experiments on intact samples. The envelope for Westerly granite [*Lockner*, 1998] is shown for comparison. The unconfined compressive strength is given by the y-intercept. The tensile strength for the granodiorite was not determined. b) Shear fractures angle as a function of the confining pressure. Ideally the fracture angle should increase with pressure, however due do the heterogeneity of the rock the data are scattered. c) The shear and normal stress resolved on the fracture plane.

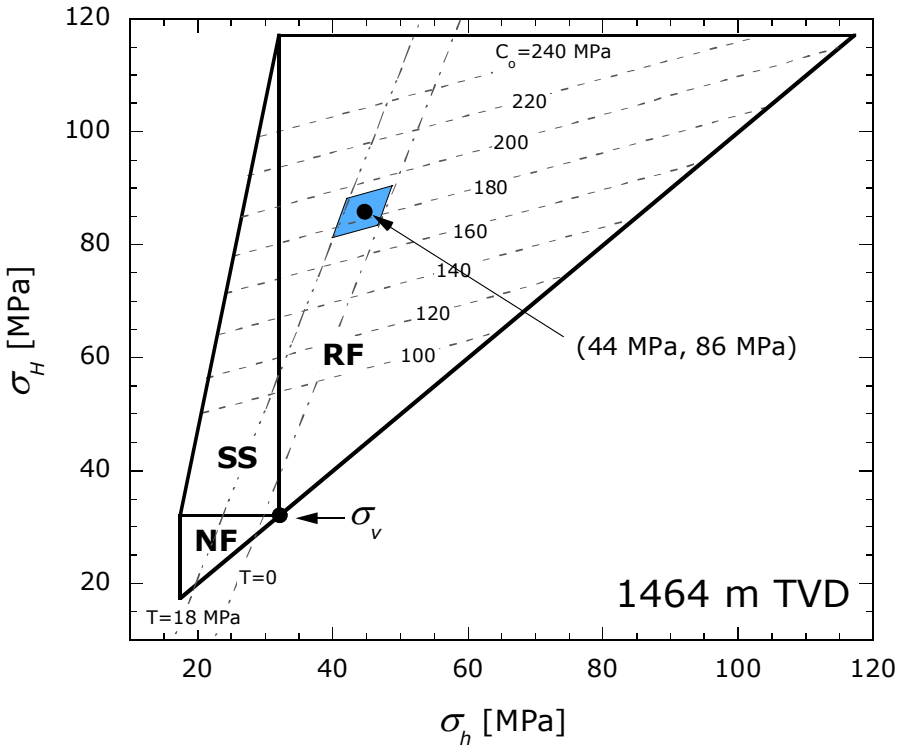

Figure 5.4. Frictional failure polygon for true vertical depth of 1464 m TVD. The solid black lines are the stress constraints given by (1). NF, SS, and RF denote normal, strike-slip, and reverse faulting, respectively. The black dot and blue rhomboid indicate the unconfined compressive strength and estimated tensile strength of the granodiorite.

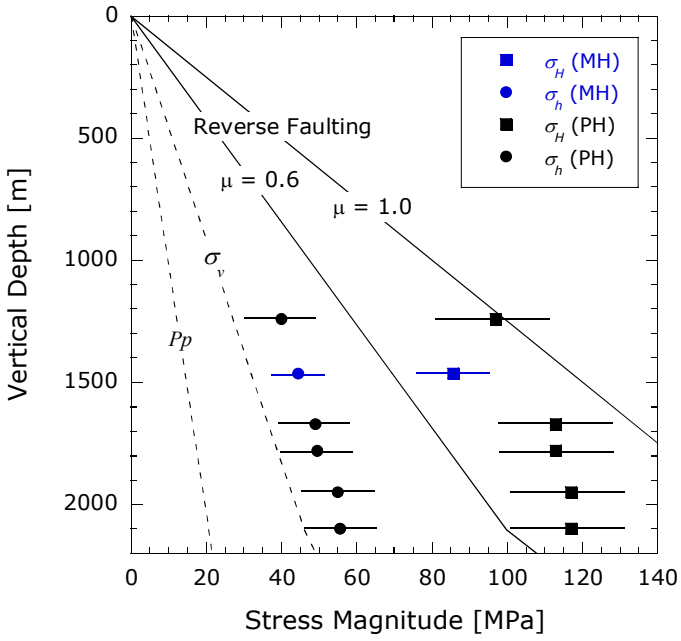

Figure 5.5. Estimated stress magnitude in the MH (blue) and pilot hole (black) [*Hickman and Zoback*, 2004]. The solid lines indicate the magnitude of the maximum horizontal stress at which frictional failure would occur on optimally oriented faults.